

ABSTRACT

ELHATISARI, SERDAR. Low Energy Continuum and Lattice Effective Field Theories. (Under the direction of Dean Lee.)

In this thesis we investigate several constraints and their impacts on the short-range potentials in the low-energy limits of quantum mechanics. We also present lattice Monte Carlo calculations using the adiabatic projection method.

In the first part we consider the constraints of causality and unitarity for the low-energy interactions of particles. We generalize Wigner's causality bound to the case of non-vanishing partial-wave mixing. Specifically we analyze the system of the low-energy interactions between protons and neutrons. We derive a general theorem that non-vanishing partial-wave mixing cannot be reproduced with zero-range interactions without violating causality or unitarity. We also analyze low-energy scattering for systems with arbitrary short-range interactions plus an attractive $1/r^\alpha$ tail for $\alpha \geq 2$. In particular, we focus on the case of $\alpha = 6$ and we derive the constraints of causality and unitarity also for these systems and find that the van der Waals length scale dominates over parameters characterizing the short-distance physics of the interaction. This separation of scales suggests a separate universality class for physics characterizing interactions with an attractive $1/r^6$ tail. We argue that a similar universality class exists for any attractive potential $1/r^\alpha$ for $\alpha \geq 2$.

In the second part of the thesis we present lattice Monte Carlo calculations of fermion-dimer scattering in the limit of zero-range interactions using the adiabatic projection method. The adiabatic projection method uses a set of initial cluster states and Euclidean time projection to give a systematically improvable description of the low-lying scattering cluster states in a finite volume. We use Lüscher's finite-volume relations to determine the s -wave, p -wave, and d -wave phase shifts. For comparison, we also compute exact lattice results using Lanczos

iteration and continuum results using the Skorniakov-Ter-Martirosian equation. For our Monte Carlo calculations we use a new lattice algorithm called impurity lattice Monte Carlo. This algorithm can be viewed as a hybrid technique which incorporates elements of both worldline and auxiliary-field Monte Carlo simulations.

© Copyright 2014 by Serdar Elhatisari

All Rights Reserved

Low Energy Continuum and Lattice Effective Field Theories

by
Serdar Elhatisari

A dissertation submitted to the Graduate Faculty of
North Carolina State University
in partial fulfillment of the
requirements for the Degree of
Doctor of Philosophy

Physics

Raleigh, North Carolina

2014

APPROVED BY:

Lubos Mitas

Thomas Schaefer

Raph Smith

Dean Lee
Chair of Advisory Committee

DEDICATION

Dedicated to my parents and siblings.

BIOGRAPHY

The author was born in Adilcevaz, which is a beautiful town along with lake Van, in Turkey. He grew up in several different cities in the east of Turkey due to his father's rotating job. He attended to Dicle University in 2002 and studied teaching physics. Elhatisari completed his five-year integrated master program and earned a Master of Science degree in 2007. Theory lectures that he attended between 2002 and 2006 were so delightful to him that he decided to pursue further education in theoretical physics.

In 2007 he was awarded by a fellowship for master programs in Turkey and he attended to the graduate program at Dicle University to study physics. In his second semester of the grad school, he applied for and won a scholarship from the Turkish Government Ministry of National Education for a doctorate study abroad. He stayed at Dicle University until 2009 when he received his second master's degree.

In the fall of 2010 Elhatisari continued to study in physics in the department of physics at North Carolina State University. At NC State he became a member of the Lee Research Group, and he worked with Professor Dean Lee and the other students in the group. In addition, he had the opportunity to collaborate with some other physicists in the field. Elhatisari currently continues his work with Dean Lee and other physicists in the Nuclear Lattice Effective Field Theory collaborations.

ACKNOWLEDGEMENTS

It is with great pleasure that I take this opportunity to express my deepest appreciation to all of those who supported me in any respect during the completion of the thesis.

First, I am very grateful to my advisor Dean Lee for his continuous supports, encouragements, endless helps and being a constant source of intellectual stimulation in every step of my studies at NC State. I am very fortunate not only because I have had the opportunity to learn from his brilliant ideas but also because I have been involved in such a friendly scientific environment provided by his kindness.

I wish to thank the Department of Physics at NC State University for taking such a nice care of all students, and want to thank everyone in the department for establishing a very nice atmosphere. I am grateful to the Turkish Government Ministry of National Education for supporting me with a doctoral fellowship and the Department of Physics at NC State University for additional supports. I am also thankful to the North Carolina State University High Performance Computing center for extensive computer support and HPC Remedy Workgroup, specially Gary Howell, for valuable technical supports.

I would like to thank Michelle Pine, Sebastian König and Shahin Bour who are members of the Lee Research Group. A special thank to Sebastian König for his collaborations and useful discussions, and Michelle Pine for carefully reading and useful comments on the manuscript of my thesis. I also thank the physicist from the Nuclear Lattice Effective Field Theory collaboration for their valuable discussions on my work. Specially I am grateful to Gautam Rupak for extensive discussions on several aspects of the adiabatic projection method, and I thank Shahin Bour, Hans-Werner Hammer and Ulf-G. Meißner for discussions on the impurity Monte Carlo method.

As a member of an internationally recognized group, I have had several opportunities to travel to many places and meet pioneers in the fields. I would like to thank Ruhr-Universität

Bochum for its hospitality during a couple of weeks in the summers of 2011, 2012 and 2013, and thank Evgeny Epelbaum and Hermann Krebs for useful discussions. I wish to thank the organizers of the program "Light nuclei from first principles" in the Institute of Nuclear Theory at the University of Washington for inviting me during two weeks of the program and thank the INT for its hospitality. Also I would like to thank the organizer of the Third UiO-MSU-ORNL-UT School on Topics in Nuclear Physics held at the Oak Ridge Laboratory for the financial support to attend the winter school.

Last, but surely not least, I would like to thank all my friends for their unquestioning support of my goals and dreams. I also wish to thank those whom I have met in the Triangle area for making the last four years of my life more fun, special thanks to Akođlu, Ay and Gökçe families, H. İbrahim Akyıldız, Murat An, Zubair Azad, Esra Öztürk, Shaan Qamar, Enis Üçüncü and Hasan Yıldırım.

TABLE OF CONTENTS

LIST OF TABLES	ix
LIST OF FIGURES	xi
Chapter 1 Overview	1
Chapter 2 Scattering Theory	4
2.1 Introduction	4
2.2 The Schrödinger wave equation	5
2.2.1 Single channel	6
2.2.2 Coupled channels	9
2.3 Interaction potential	11
2.4 Effective range expansion	12
2.5 Scattering solutions	14
2.5.1 Neutral particles	14
2.5.2 Charged particles	15
2.5.3 Wronskian integral formula	18
2.6 Loosely bound systems	21
2.6.1 Asymptotic Normalization Coefficients	21
Chapter 3 Lattice Effective Field Theory	26
3.1 Introduction	26
3.2 The path integral	29
3.3 Grassmann variables	33
3.4 Lattice formulation	34
3.4.1 The transfer matrix	36
3.4.2 Adiabatic projection methods	39
3.5 Scattering phase shifts from the lattice	41
3.5.1 Cubic rotational group	42
3.5.2 Lüscher's finite-volume method	42
3.5.3 Spherical wall method	44
3.6 Numerical methods	45
3.6.1 Monte Carlo methods	45
3.6.2 Importance sampling	46
3.6.3 Markov process	47
3.6.4 Metropolis algorithm	49
3.6.5 Sign problem	50
Chapter 4 Neutron-proton scattering	51

4.1	Introduction	51
4.2	Uncoupled Channels	55
4.3	Coupled Channels	56
4.4	Causality Bounds	65
4.5	Neutron-Proton Scattering	66
4.5.1	Uncoupled Channels	67
4.5.2	Coupled Channels	70
4.6	Results and Discussion	75
4.7	One-Pion Exchange Potential	79
4.8	Summary and Conclusions	88
Chapter 5 van der Waals interactions		92
5.1	Introduction	92
5.2	Causality bounds and effective field theory	95
5.3	Asymptotic solutions of the Schrödinger equation	96
5.4	Causality bounds for short-range K-matrix K_ℓ	98
5.5	Impact on effective field theory	102
5.6	Quantum defect theory and the modified effective range expansion	106
5.7	Causal range for single-channel scattering	108
5.8	Causal range near a magnetic Feshbach resonance	110
5.9	Summary and discussion	112
Chapter 6 Impurity Lattice Monte Carlo and the Adiabatic Projection Method . .		115
6.1	Introduction	115
6.2	Lattice Hamiltonian	118
6.3	Lattice path integrals and transfer matrices	120
6.4	Impurity Lattice Monte Carlo: Single Impurity	121
6.5	Adiabatic Projection Method	125
6.6	Impurity Monte Carlo Simulation	126
6.7	Composite particles in finite volume	131
6.7.1	Lüscher's finite-volume method	132
6.7.2	Results for the elastic phase shifts	133
6.8	Summary and discussion	138
BIBLIOGRAPHY		141
Appendices		154
Appendix A		155
A.1	Bessel and related Functions	155
A.2	Coulomb wave functions	156
A.2.1	Regular solution $f(\varepsilon, \ell; r_\gamma)$	158

A.2.2	Irregular solution.I	$h(\varepsilon, \ell; r_\gamma)$	159
A.2.3	Irregular solution.II	$g(\varepsilon, \ell; r_\gamma)$	160
A.3	van der Waals wave functions		165
A.4	Low-energy expansions of the function terms in van der Waals wave functions		168
Appendix B			169
B.1	Wronskians of the wave functions		169
B.1.1	Single channel		169
B.1.2	Coupled channels		172
Appendix C			175
C.1	Coupled-channel Parameterizations		175
C.2	Numerical Test using Delta-Function Shell Potentials in a coupled-channel system		177
Appendix D			184
D.1	Finite-volume binding energy corrections and topological volume corrections for scattering with arbitrary ℓ		184

LIST OF TABLES

Table 2.1	The integration constants $\Delta_{n,\ell}$ of a two-neutral-particles system for $\ell \leq 2$	22
Table 2.2	Integration constants $\Delta_{n,\ell}^c$ calculated from Eqs. (2.71)-(2.74) for $\ell \leq 2$ in Coulomb case	24
Table 2.3	The function $\gamma\tilde{h}_\ell(i\kappa)$ in the Coulomb modified effective range expansion for $\ell \leq 2$	25
Table 3.1	Decomposition of the SO(3) into the irreducible representations of the SO(3,Z) for $\ell \leq 6$	43
Table 4.1	The eigenphase low energy parameters of uncoupled channels for neutron-proton scattering by the NijmII and the Reid93 interaction potentials.	67
Table 4.2	The eigenphase low energy parameters of coupled channels for neutron-proton scattering by the NijmII and the Reid93 interaction potentials.	68
Table 4.3	The eigenphase low energy mixing parameters of coupled channels for neutron-proton scattering by the NijmII and the Reid93 interaction potentials.	68
Table 4.4	The causal ranges for uncoupled channels.	77
Table 4.5	The causal ranges for coupled channels.	77
Table 4.6	The Cauchy-Schwarz ranges for coupled channels.	77
Table 4.7	The potential range dependence of the causal range in various channels.	88
Table 5.1	Scattering parameters and causal ranges for s -wave scattering of ${}^7\text{Li}$, ${}^{23}\text{Na}$, and ${}^{133}\text{Cs}$ pairs. The scattering data collection is taken from Ref. [66]. In columns I and IV the scattering data for ${}^7\text{Li}$ are from Ref. [41], the scattering data for ${}^{23}\text{Na}$ are from Refs. [40, 41], and data for ${}^{133}\text{Cs}$ are from Ref. [129]. In column III the effective range parameters, R_0 , are calculated analytically in Refs. [66, 75]. In column IV, the R_0 are obtained from numerical calculations. The scattering parameters in columns II and V are calculated using Eq. (5.37) and Eq. (5.39), and the causal ranges in column VI are obtained from Eq. (5.40).	110
Table 6.1	Momentum of the dimer, \vec{p}_d , with $p = 2\pi/L$. The total momentum of the system is zero.	128
Table 6.2	The exact and Monte Carlo results for the ground state and lowest lying even-parity energies in a periodic box of length $La = 13.79$ fm. The Monte Carlo results are obtained from the $[\hat{M}^a(t)]_{4 \times 4}$ adiabatic matrix.	130
Table 6.3	The exact and Monte Carlo results for the energies of the lowest two odd-parity states in a periodic box of length $La = 13.79$ fm. The Monte Carlo results are obtained from the $[\hat{M}^a(t)]_{5 \times 5}$ adiabatic matrix.	132

Table C.1	Numerical results for scattering length and effective range in two-body interaction by the delta function potentials.	180
Table C.2	Numerical results for the mixing parameters in two-body interaction by the delta function potentials.	181

LIST OF FIGURES

Figure 4.1	The plot of $[b_\ell(r) - r_\ell]/2$ as a function of r for neutron-proton scattering via the NijmII potential in the $^{2s+1}\ell_j$ channel.	69
Figure 4.2	The plot of $f_{j-1}(r)$ as a function of r for neutron-proton scattering via the NijmII potential for $j \leq 3$. Here $f_1(r)$ is rescaled by a factor of 0.01 and $f_2(r)$ is rescaled by a factor of 10^{-4}	70
Figure 4.3	The plot of $g_{j+1}(r)$ as a function of r for neutron-proton scattering via the NijmII potential for $j \leq 3$. Here $g_3(r)$ is rescaled by a factor of 0.1.	71
Figure 4.4	We plot $\text{Re}\left[\sqrt{f_0(r)g_2(r)}\right]$, $-\text{Re}\left[\sqrt{f_0(r)g_2(r)}\right]$, and $\text{Re}[h_1(r)]$ as functions of r for neutron-proton scattering in 3S_1 - 3D_1 coupled channel.	72
Figure 4.5	We plot $\text{Re}\left[\sqrt{f_1(r)g_3(r)}\right]$, $-\text{Re}\left[\sqrt{f_1(r)g_3(r)}\right]$, and $\text{Re}[h_2(r)]$ as functions of r for neutron-proton scattering in 3P_2 - 3F_2 coupled channel. The functions are rescaled by a factor of 0.01.	74
Figure 4.6	We plot $\text{Re}\left[\sqrt{f_2(r)g_4(r)}\right]$, $-\text{Re}\left[\sqrt{f_2(r)g_4(r)}\right]$, and $\text{Re}[h_3(r)]$ as functions of r for neutron-proton scattering in 3D_3 - 3G_3 coupled channel. The functions are rescaled by a factor of 0.01.	76
Figure 4.7	Plot of the potential matrix elements $W_{11}(r) = V_C(r)$, $W_{12}(r) = W_{21}(r) = \sqrt{8}V_T(r)$ and $W_{22}(r) = V_C(r) - 2V_T(r)$ as a function of r in the 3S_1 - 3D_1 coupled channel.	82
Figure 4.8	Plot of the model potential in the 1P_1 channel. In this channel $S = 0$, $T = 0$, $C_\pi = 9$, $C_A = 405.9$, $C_B = 769.5$, $C_\Pi = 0$, $C_D = 0$, $C_F = 0$, $C_G = -7.6$, $m_A = 10.0m_\pi$, $m_B = 5.45m_\pi$, $m_G = 4.46m_\pi$, $C_1 = -7.464$, $C_2 = 0.179$, $C_3 = 73.933$ and $C_4 = -78.011$. We use $R_{\text{Gauss}} = 0.2$ fm and $R_{\text{Exch.}} = 0.7$ fm.	85
Figure 4.9	Plot of the model potential in the 1D_2 channel. In this channel $S = 0$, $T = 1$, $C_\pi = -3$, $C_A = -60.5$, $C_B = -30.0$, $C_\Pi = 0$, $C_D = 0$, $C_F = 0$, $C_G = 1.01$, $m_A = 9m_\pi$, $m_B = 6m_\pi$, $m_G = 7.02m_\pi$, $C_1 = 1.463$, $C_2 = -7.332$, $C_3 = 10.384$ and $C_4 = -4.585$. We use $R_{\text{Gauss}} = 0.2$ fm and $R_{\text{Exch.}} = 0.9$ fm.	86
Figure 4.10	Plot of the model potential in the 3D_2 channel. In this channel $S = 1$, $T = 0$, $C_\pi = -3$, $C_A = -660$, $C_B = -1140$, $C_\Pi = -3$, $C_D = -930$, $C_F = -927$, $C_G = 2.53$, $m_A = m_D = 8m_\pi$, $m_B = m_F = 5m_\pi$, $m_G = 3.25m_\pi$, $C_1 = 2.979$, $C_2 = -4.026$, $C_3 = -2.455$ and $C_4 = 2.409$. We use $R_{\text{Gauss}} = 0.3$ fm and $R_{\text{Exch.}} = 1.4$ fm.	87
Figure 5.1	(Color online) Plot of $W[f_{0,2}, f_{0,0}](r)$, $W[g_{0,2}, g_{0,0}](r)$, and $W[g_{0,2}, f_{0,0}](r)$ as a function of r for $\ell = 0$ and $\beta_6 = 50$ (a.u.).	103
Figure 5.2	(Color online) Plot of $W[f_{1,2}, f_{1,0}](r)$, $W[g_{1,2}, g_{1,0}](r)$, and $W[g_{1,2}, f_{1,0}](r)$ as a function of r for $\ell = 1$ and $\beta_6 = 50$ (a.u.).	103

Figure 5.3	(Color online) Plot of $W[f_{2,2}, f_{2,0}](r)$, $W[g_{2,2}, g_{2,0}](r)$, and $W[g_{2,2}, f_{2,0}](r)$ as a function of r for $\ell = 2$ and $\beta_6 = 50$ (a.u.).	104
Figure 6.1	A segment of a worldline configuration on a 1+1 dimensional Euclidean lattice. See the main text for derivations of the reduced transfer-matrix operators.	123
Figure 6.2	The ground state energy is shown versus projection time t using either one or four initial/final states in Panel (a) and the first two excited state energies with even parity in Panel (b). For comparison we show the exact lattice energies as dotted horizontal lines.	129
Figure 6.3	The lowest two odd parity energies as a function of Euclidean projection time t . For comparison we show the exact lattice energies as dotted horizontal lines.	131
Figure 6.4	The s -wave scattering phase shift versus the relative momentum between fermion and dimer.	134
Figure 6.5	The p -wave scattering phase shift versus the relative momentum between fermion and dimer.	135
Figure 6.6	The d -wave scattering phase shift versus the relative momentum between fermion and dimer.	136

Chapter 1

Overview

Nuclear structure and reaction studies are at the heart of low energy nuclear physics research. A broad goal of this research is to understand the basic interactions among fundamental particles. By fundamental particles we refer to the relevant degrees of freedom that can be probed by the energy scales of a given system. In nuclear physics physical phenomena are observed over a range of different energy scales. In low energy nuclear physics the relevant degrees of freedom are nucleons and light mesons which mediate forces between nucleons, and physical observables are insensitive to the details at high energies or equivalently short distances.

Effective field theory (EFT) is a very general framework to understand physics. The general idea is that a simple effective description of the physics can describe the relevant features of a given system even if the details at short distances are disregarded. In low-energy nuclear effective field theory the detailed shape of the short-range nuclear forces are not important. Instead effective field theory organizes the nuclear interactions as an expansion in powers of momenta and other low energy scales such as the pion mass.

Lattice effective field theory is a powerful numerical method which is formulated in the framework of effective field theory. The method is quite economical when one uses pionless

effective field theory with the nucleons interacting via only local contact interactions. Recent developments in lattice EFT allow one to study nuclear scattering and reactions. The adiabatic projection method is a general framework for calculating scattering and reactions on the lattice. This method uses a set of initial cluster states and Euclidean time projection to construct a low-energy effective field theory for the cluster states.

In this thesis we summarize work done on a number of topics in the framework of effective field theories during my Ph.D. study. We start with a brief review of scattering processes with strictly finite-range interactions in Chapter 2. We also discuss the case where long-range forces are present in addition to the short-range interactions, and we specifically consider Coulomb interactions.

In Chapter 3 after a brief introduction we define the basic continuum and lattice formulations of non-relativistic quantum mechanics. We then take a short detour to derive the connection between the operator formalism in quantum mechanics and lattice Grassmann path integrals. We introduce the adiabatic projection method and describe the implementation of the method in lattice effective field theory. We discuss the details of and some mathematical tools for scattering phase shift calculations at finite volume. Then we close this chapter by reviewing Monte Carlo simulations employed to compute observables in finite volumes with periodic boundary conditions.

In Chapter 4 we consider the Wigner causality constraint and unitarity for the low-energy interactions with strictly finite range. We derive the generalization of Wigner's causality bound to the case of non-vanishing partial-wave mixing. As an application in nuclear physics, we analyse the low-energy interactions of protons and neutrons. We investigate the constraints on the range of the interactions between neutrons and protons in effective field theory and universality in many-body Fermi systems.

In Chapter 5 we analyze low-energy scattering for arbitrary short-range interactions plus

any attractive potential $1/r^\alpha$ for $\alpha \geq 2$. This type of long-range force plays an important role in low-energy atomic and nuclear physics. In particular, we consider the van der Waals interaction and derive the constraints of causality and unitarity. We also briefly discuss multichannel systems near a magnetic Feshbach resonance.

In Chapter 6 we present scattering of composite particles using lattice Monte Carlo simulations with the adiabatic projection method. For our Monte Carlo simulations we introduce the impurity lattice Monte Carlo algorithm. As an application we consider fermion-dimer elastic scattering in the limit of zero-range interactions. Then we present results for the scattering phase shifts in the continuum and infinite volume limits as well as in finite volumes.

Scattering Theory

2.1 Introduction

The scattering of two spinless particles is described by an incident plane wave along the z direction and spherical outgoing scattered wave with amplitude f as

$$\psi(\vec{r}) \xrightarrow{r \rightarrow \infty} \frac{1}{(2\pi)^{3/2}} \left[e^{ipz} + f(p, \theta) \frac{e^{ipr}}{r} \right], \quad (2.1)$$

where \vec{p} is the outgoing relative momenta, \vec{r} is the relative coordinates and θ is the angle between \vec{p} and the z axis. The scattering amplitude is a non-trivial physical quantity in which all quantitative information about the scattering process is contained. An important constraint on the scattering amplitude is unitarity. Unitarity requires that the sum of all outcome probabilities is one. In other word the normalization of the incoming wave must be preserved.

In addition, the time evolution of any quantum mechanical system obeys *causality* as well as unitarity. Causality requires that the cause of an event must occur before any resulting consequences are produced. In non-relativistic quantum mechanics the causality constraint means that the outgoing wave may depart only after the incoming wave reaches the scattering

object. The constraints of causality in quantum mechanics with finite range interactions were first studied by Wigner [174]. Phillips and Cohen [142] derived the causality bound on the scattering parameters of low energy effective field theories by considering the s -wave case and finite-range interactions in three dimensions. Later, the causality bounds for arbitrary dimension d or arbitrary angular momentum ℓ were investigated in Refs. [94, 95].

The scattering processes described above is an idealized system with the assumptions that particles are structureless. This simplified process is called *single-channel* since there is only one possible final configuration which is the same as the initial one, $a(b,a)b$. In general, elementary or composite particles have spin structures; and accordingly, the interaction potentials become spin-dependent which makes the scattering processes more complicated. In these types of system different possible final outcomes exist [164], and the scattering processes are called *multi-channel* scattering. See Ref. [100] for a detailed rigorous mathematical formulation of the system with short-range interactions, and the general multi-channel problems in the presence of long-range potentials were studied in Ref. [49, 92].

2.2 The Schrödinger wave equation

In this and the following sections we will give brief reviews on several topics of the two-body elastic scattering problem. Following Refs. [136] with slightly changed notation, we will discuss the scattering of particles within the framework of the formal scattering theory in configuration space.

2.2.1 Single channel

We start with an idealized system and consider elastic scattering of two spinless¹ particles interacting via a spherically symmetric potential in the center-of-mass frame. We use units where $\hbar = 1$. The free radial Schrödinger equation with energy $E = p^2/(2\mu)$ is

$$\left[-\frac{1}{r^2} \frac{d}{dr} \left(r^2 \frac{d}{dr} \right) + \frac{\ell(\ell+1)}{r^2} \right] R_\ell^{(p)}(r) = p^2 R_\ell^{(p)}(r). \quad (2.2)$$

where ℓ is the orbital angular momentum. It is convenient to use the rescaled radial function $u_\ell^{(p)}(r)$ given by

$$u_\ell(pr) = r R_\ell^{(p)}(r), \quad (2.3)$$

then the Schrödinger equation describes the system is alternatively

$$\left[-\frac{d^2}{dr^2} + \frac{\ell(\ell+1)}{r^2} \right] u_\ell(pr) = p^2 u_\ell(pr), \quad (2.4)$$

Two linearly independent (regular and irregular) solutions of Eq. (2.4) are the Riccati-Bessel $S_\ell(pr)$ and Riccati-Neumann $C_\ell(pr)$ functions, respectively, which are defined in terms of Bessel and Neumann functions in Eq. (A.1) and Eq. (A.2). The asymptotic form of these functions for large arguments are

$$S_\ell(\rho) \stackrel{|\rho| \rightarrow \infty}{\sim} \sin \left(\rho - \frac{\ell\pi}{2} \right), \quad (2.5)$$

$$C_\ell(\rho) \stackrel{|\rho| \rightarrow \infty}{\sim} \cos \left(\rho - \frac{\ell\pi}{2} \right). \quad (2.6)$$

¹By spinless particles we mean either exactly spinless fundamental particles or composite particles with zero-intrinsic angular momentum.

The total wave function in the partial wave expansion form is

$$\Psi^\pm = (p, \vec{r}) = \left(\frac{2\mu p}{\pi} \right)^{1/2} \sum_{\ell} \sum_{m=-\ell}^{\ell} i^{\ell} \frac{\psi_{\ell}^{\pm}(pr)}{pr} Y_{\ell}^m(\hat{r}) Y_{\ell}^{m*}(\hat{z}), \quad (2.7)$$

where μ is the reduced mass, $Y_{\ell}^m(\hat{\rho})$ are the spherical harmonics, \hat{r} denotes the polar angles (θ, ϑ) of \vec{r} , $\psi_{\ell}^{\pm}(pr)$ is the radial part of the wave function. The solution with the superscript $+/-$ corresponds to the out/in asymptotic wave when we go to a time-dependent formalism. Using the Legendre polynomial,

$$P_{\ell}(\cos \theta) = \frac{4\pi}{2\ell + 1} \sum_{m_{\ell}=-\ell}^{\ell} Y_{\ell}^m(\hat{r}) Y_{\ell}^{m*}(\hat{z}), \quad (2.8)$$

the total wave function is rewritten as

$$\Psi^\pm(p, \vec{r}) = \left(\frac{2\mu}{\pi p} \right)^{1/2} \frac{1}{4\pi r} \sum_{\ell} i^{\ell} (2\ell + 1) P_{\ell}(\cos \theta) \psi_{\ell}^{\pm}(pr). \quad (2.9)$$

Now inserting the total wave function in the Lippmann-Schwinger integral equation, we get the following integral equation for the radial wave function,

$$\psi_{\ell}^{\pm}(pr) = S_{\ell}(pr) + 2\mu \int_0^{\infty} \int_0^{\infty} dr' dr'' G_{\ell}^{\pm}(p; r, r') W(r', r'') \psi_{\ell}^{\pm}(pr'), \quad (2.10)$$

where $W(r', r'')$ is the interaction potential assumed to be a rotationally invariant operator, and $G_{\ell}^{\pm}(p; r, r')$ is the partial wave Green's function which satisfies the differential equation

$$\left[-\frac{d^2}{dr^2} + \frac{\ell(\ell+1)}{r^2} - p^2 \right] G_{\ell}^{\pm}(p; r, r') = -\delta(r - r'). \quad (2.11)$$

The Green's function that satisfies Eq. (2.11) with suitable boundary conditions is defined in terms of the Riccati-Bessel and Riccati-Henkel functions as

$$G_{\ell}^{\pm}(p; r, r') = -\frac{1}{p} S_{\ell}(pr_{<}) h_{\ell}^{\pm}(pr_{>}), \quad (2.12)$$

where $r_{<}$ signifies the smaller of r and r' and $r_{>}$ is the larger, and h_{ℓ}^{\pm} are the Riccati-Henkel functions defined in terms of the Riccati-Bessel and Neumann functions

$$h_{\ell}^{\pm}(\rho) = \pm i S_{\ell}(\rho) + C_{\ell}(\rho), \quad (2.13)$$

and their asymptotic forms for large arguments are

$$h_{\ell}^{\pm}(\rho) \stackrel{|\rho| \rightarrow \infty}{\sim} e^{\pm i(\rho - \frac{\ell\pi}{2})}. \quad (2.14)$$

Eq. (2.10) is the solution of the following Schrödinger wave equation,

$$\left[-\frac{d^2}{dr^2} + \frac{\ell(\ell+1)}{r^2} \right] \psi_{\ell}^{+}(pr) + 2\mu \int_0^{\infty} dr' W(r, r') \psi_{\ell}^{+}(pr') = p^2 \psi_{\ell}^{+}(pr). \quad (2.15)$$

At the moment we do not impose any condition on the potential and postpone the discussion till Section 2.3. At $r \rightarrow \infty$ the asymptotic form of Eq. (2.10) has a formal solution written in terms of the incident wave, the scattered wave and the scattering matrix, $S_{\ell}(p)$, as

$$\psi_{\ell}^{+}(pr) = \frac{i}{2} [h_{\ell}^{-}(pr) - S_{\ell}(p) h_{\ell}^{+}(pr)], \quad (2.16)$$

where

$$S_{\ell}(p) = 1 - \frac{4i\mu}{p} \int_0^{\infty} \int_0^{\infty} dr' dr'' S_{\ell}(pr') W(r', r'') \psi_{\ell}^{+}(pr'), \quad (2.17)$$

The scattering matrix (S-matrix) $S_\ell(p)$ is a function of momentum and independent of r ; therefore, $S_\ell(p)$ can be defined in terms of a real and momentum dependent phase angle $\delta_\ell(p)$,

$$S_\ell(p) = e^{2i\delta_\ell(p)}. \quad (2.18)$$

Then Eq. (2.15) in the asymptotic limit, up to a normalization, becomes

$$\psi_\ell^+(pr) \sim \sin\left(pr - \frac{\ell\pi}{2} + \delta_\ell(p)\right). \quad (2.19)$$

This scattered wave relative to Eq. (2.5) implies that the impact of the scattering event is to introduce the shift $\delta_\ell(p)$ in the phase of the outgoing wave relative to the incoming wave. The radial wave function is usually written in terms of the reaction matrix² (K-matrix) rather than the S-matrix. The relation between the reaction and scattering matrix is

$$\mathbf{K}_\ell = i \frac{(1 - S_\ell)}{(1 + S_\ell)}, \quad (2.20)$$

and the radial wave function in terms of the reaction matrix reads, up to a normalization,

$$\psi_\ell^+(pr) \sim S_\ell(p) C_\ell(pr) + \mathbf{K}_\ell(p) C_\ell(pr). \quad (2.21)$$

2.2.2 Coupled channels

In this section we make the scattering problem more complicated by considering that particles have intrinsic spins. This brings some complications into the formalism introduced in the preceding sections due to the fact that the spin is an additional degree of freedom. We consider the scattering of two particles with total spin angular momenta $s = s_1 + s_2$ where s_1 and s_2 are the

²Sometimes it is called the reactance matrix [136].

individual particle spins. Here the orbital angular momentum ℓ and the spin angular momentum s are coupled to give the total angular momentum j . Denote the magnetic quantum number of j , ℓ and s in the z direction by M , m and m_s , respectively. Since the Hamiltonian of the system commutes with the total angular momentum operator \mathbf{J} in order to be rotationally invariant, the conserved quantities of the system are j and M . Therefore, depending on the values that s takes, the orbital angular momentum takes different values each of which corresponds to a different radial wave function.

Let us generalize the spherical harmonics for the system of particles with spin and define the following functions

$$\mathcal{Y}_{j\ell s}^M(\hat{r}) = \sum_{mm_s} C(\ell s j, m m_s M) Y_\ell^m(\hat{r}) \chi_{m_s}^s \quad (2.22)$$

and

$$\mathcal{Y}_j^M(\ell s m_s; \hat{z}) = -i \chi_{m_s}^{s*} \cdot \mathcal{Y}_{j\ell s}^M(\hat{z}) \quad (2.23)$$

where $\chi_{m_s}^s$ is the normalized eigenfunction of the total spin, $C(\ell s j, m_\ell m_s m)$ are the Clebsch-Gordan coefficients, and the dot signifies an inner product with respect to the internal coordinates. Since the individual particle spins are conserved, we will suppress them in the expressions. The completeness relation of the Clebsch-Gordan coefficients is

$$\sum_{m_\ell m_s} C(\ell s j, m_\ell m_s m) C(\ell s j', m_\ell m_s m') = \delta_{jj'} \delta_{mm'}. \quad (2.24)$$

Therefore, the total wave function is written as

$$\Psi^\pm(sm_s; p, \vec{r}) = \left(\frac{2\mu}{\pi p}\right)^{1/2} \sum_{jM\ell\ell's'} \frac{\Psi_{\ell's',\ell s}^{j(\pm)}(p, r)}{r} \mathcal{Y}_{j\ell's'}^M(\hat{r}) \mathcal{Y}_j^{M*}(\ell s m_s; \hat{z}). \quad (2.25)$$

After inserting Eq. (2.25) into the Lippmann-Schwinger integral equation, we obtain the general form of the radial wave function,

$$\begin{aligned} \Psi_{\ell's',\ell s}^{j(\pm)}(p,r) = & S_{\ell}(pr) \delta_{\ell\ell'} \delta_{ss'} \\ & + 2\mu \sum_{\ell''s''} \int_0^{\infty} \int_0^{\infty} d\bar{r}' d\bar{r}'' G_{\ell'}^{\pm}(p;r,r') W_{\ell's',\ell''s''}(r',r'') \Psi_{\ell''s'',\ell s}^{j(\pm)}(p,r'), \end{aligned} \quad (2.26)$$

where $G_{\ell'}^{\pm}$ is given in Eq. (2.12), and $W_{\ell's',\ell''s''}$ is the spin-dependent interaction potential

$$W_{\ell's',\ell''s''}(r',r'') = \int d\Omega \mathcal{Y}_{j\ell's'}^{M*}(\hat{r}') W(r',r'') \mathcal{Y}_{j\ell''s''}^M(\hat{r}''). \quad (2.27)$$

The radial wave function $\Psi_{\ell's',\ell s}^{j(\pm)}$ is the solution of the coupled Schrödinger equation,

$$\left[-\frac{d^2}{dr^2} + \frac{\ell'(\ell'+1)}{r^2} \right] \Psi_{\ell's',\ell s}^{j(+)} + 2\mu \sum_{\ell''s''} \int_0^{\infty} dr' W_{\ell's',\ell''s''}(r,r') \Psi_{\ell''s'',\ell s}^{j(+)} = p^2 \Psi_{\ell's',\ell s}^{j(+)}. \quad (2.28)$$

Therefore, the S-matrix for the particles of the total spin s is

$$S_{\ell's',\ell s} = \delta_{\ell\ell'} \delta_{ss'} - \frac{4i\mu}{p} \sum_{\ell''s''} \int_0^{\infty} \int_0^{\infty} dr' dr'' S_{\ell'}(pr') W_{\ell's',\ell''s''}(r',r'') \Psi_{\ell''s'',\ell s}^{j(+)}(p,r'). \quad (2.29)$$

2.3 Interaction potential

In Eq. (2.18) we have naïvely defined the S-matrix without imposing any conditions on the potential. However, in Eqs. (2.17) and (2.29) the unitarity condition we have discussed in Section 2.1 requires some constraints on the interaction potential.

Throughout our analysis we assume that the interaction is sufficiently well-behaved at the origin to admit the regular solution $S_{\ell}(pr)$. This assumption imposes the restriction that as

$r \rightarrow 0$ the potential is not too singular such that the radial wave function satisfies the regularity condition

$$\lim_{\rho \rightarrow 0} \psi_\ell(\rho) \frac{d}{d\rho} \psi_\ell(\rho) = 0. \quad (2.30)$$

In Ref. [21] it is proven that this condition is fulfilled by a class of potentials $V(r)$ provided that

$$\int_0^R dr' r' |V(r')| < \infty. \quad (2.31)$$

We also consider only energy independent interactions, and we assume that the interactions have a finite range R . The finite-range condition implies that

$$W(r, r') = 0 \quad \text{if } r > R \quad \text{or } r' > R. \quad (2.32)$$

These assumptions assure that the interaction can be written as a local potential,

$$W(r, r') = V(r) \delta(r - r'). \quad (2.33)$$

2.4 Effective range expansion

Under our assumptions on the potential in the preceding section we can obtain the scattering information by measuring Eq. (2.10) relative to the free solution in the asymptotic limit,

$$\psi_\ell(r) = S_\ell(pr) + pf_\ell(p) h_\ell^+(pr), \quad (2.34)$$

where $f_\ell(p)$ is the partial wave amplitude

$$f_\ell(p) = \frac{S_\ell(p) - 1}{2ip} = \frac{p^{2\ell}}{p^{2\ell+1} \cot \delta_\ell(p) - ip^{2\ell+1}}. \quad (2.35)$$

For the system of particles interacting with a finite-range potential, $p^{2\ell+1} \cot \delta_\ell(p)$ is described by the well-known power series expansion around p^2 , the so called *effective range expansion* [99, 18],

$$p^{2\ell+1} \cot \delta_\ell(p) = -\frac{1}{a_\ell} + \frac{1}{2} r_\ell p^2 + P_\ell p^4 + Q_\ell p^6 + \mathcal{O}(p^8), \quad (2.36)$$

where a_ℓ is the *scattering length*, r_ℓ is the *effective range*, and coefficients in higher order terms of p^2 are the shape parameters. The effective range formula for the multi channel scattering problem is of the following form [46, 149, 20, 19, 102],

$$\sum_{m',n'} \mathbf{p}_{mm'} [\mathbf{K}^{-1}]_{m'n'} \mathbf{p}_{n'n} = -\frac{1}{\mathbf{a}_{mn}} + \frac{1}{2} \mathbf{r}_{mn} p^2 + \mathbf{P}_{mn} p^4 + \mathbf{Q}_{mn} p^6 + O(p^8), \quad (2.37)$$

where $\hat{\mathbf{K}}$ is the multi channel reaction matrix, \mathbf{p} is the diagonal momentum matrix

$$\mathbf{p} = \begin{pmatrix} p^{j-s+\frac{1}{2}} & & \\ & \ddots & \\ & & p^{j+s+\frac{1}{2}} \end{pmatrix}, \quad (2.38)$$

\mathbf{a}_{mn} is the scattering length matrix, \mathbf{r}_{mn} is the effective range matrix, and \mathbf{P}_{mn} and \mathbf{Q}_{mn} are the first two lowest shape parameter matrices.

In the cases where particles are interacting via long-range forces the power series or the convergence (analyticity) of Eq. (2.36) is spoiled. Then the function $p^{2\ell+1} \cot \delta_\ell(p)$ needs special treatment to modify the expansion to make it an analytic function of p^2 . For instance, for a class of potentials falling off as e^{-mr} at large distances, the potential introduces a branch cut starting at $p^2 = -m^2/4$ where m is the mass of the particle which mediates the interaction, see Ref. [90] for the detailed proof. Nevertheless, the expansion is still converges in a circle of radius $m^2/4$ around the origin of the complex p^2 plane.

For the system of charged particles, a modified effective range expansion is used to deal with the Coulomb tails [39, 18, 21]. For long-range potentials of the form of $1/r^\alpha$ with $\alpha > 2$ the irregular behavior of the radial Schrödinger equation at short distances limits the determination of the partial wave amplitude. For example, for $\alpha = 4$ only the scattering length can be well-defined [139]. However, the so called quantum defect formulation for the scattering phase shifts allows one to define the total phase shift for $\alpha > 2$ as a sum of a weakly energy-dependent short-range phase shift and strongly energy-dependent long-range phase shift [78]. This formalism has been developed to describe atom-atom scattering. In particular, quantum defect theory and the modified effective range expansion for $\alpha = 6$ will be discussed in Section 5.6.

2.5 Scattering solutions

2.5.1 Neutral particles

In this section we return to the idealized system of two spinless particles. Here we consider the system of two-particle interacting via a spherically symmetric potential with finite-range R . This system is described by the radial Schrödinger equation

$$\left[-\frac{d^2}{dr^2} + \frac{\ell(\ell+1)}{r^2} - p^2 \right] U_\ell^{(p)}(r) + 2\mu \int_0^R dr' W(r, r') U_\ell^{(p)}(r') = 0. \quad (2.39)$$

where μ is the reduced mass, and $W(r, r')$ is the finite-range potential, $W(r, r') = 0$ for $r > R$ or $r' > R$. Therefore, for $r > R$ with an arbitrary normalization the solution of Eq. (2.39) is written as

$$U_\ell^{(p)}(r) = p^\ell [\cot \delta_\ell(p) S_\ell(pr) + C_\ell(pr)]. \quad (2.40)$$

For later convenience we define the rescaled Riccati-Bessel and Riccati-Neumann functions by

$$s_\ell(p, r) = p^{-\ell-1} S_\ell(pr) \quad \text{and} \quad c_\ell(p, r) = p^\ell C_\ell(pr). \quad (2.41)$$

Insertion of the rescaled functions and the effective range expansion, Eq. (2.40) is rewritten as an expansion in powers of p^2 ,

$$U_\ell^{(p)}(r) = u_{0,\ell}(r) + u_{2,\ell}(r)p^2 + u_{4,\ell}(r)p^4 + u_{6,\ell}(r)p^6 + \mathcal{O}(p^8), \quad (2.42)$$

where $u(r)$'s are defined in terms of the effective range expansion parameters by

$$u_{0,\ell}(r) = \frac{-1}{a_\ell} s_{0,\ell}(r) + c_{0,\ell}(r), \quad (2.43)$$

$$u_{2,\ell}(r) = \frac{1}{2} r_\ell s_{0,\ell}(r) - \frac{1}{a_\ell} s_{2,\ell}(r) + c_{2,\ell}(r), \quad (2.44)$$

$$u_{4,\ell}(r) = P_\ell s_{0,\ell}(r) + \frac{1}{2} r_\ell s_{2,\ell}(r) - \frac{1}{a_\ell} s_{4,\ell}(r) + c_{4,\ell}(r), \quad (2.45)$$

$$u_{6,\ell}(r) = Q_\ell s_{0,\ell}(r) + P_\ell s_{2,\ell}(r) + \frac{1}{2} r_\ell s_{4,\ell}(r) - \frac{1}{a_\ell} s_{6,\ell}(r) + c_{6,\ell}(r). \quad (2.46)$$

and the functions $s_{n,\ell}(r)$ and $c_{n,\ell}(r)$ are given in Appendix A.1.

2.5.2 Charged particles

We consider two particles interacting at long distances in addition to the short-range potential. The example we consider in detail is the system of two particles carrying electric charges eZ_1 and eZ_2 . The radial Schrödinger equation (2.39) has a Coulomb potential term γ/r ,

$$\left[-\frac{d^2}{dr^2} + \frac{\ell(\ell+1)}{r^2} + \frac{\gamma}{r} - p^2 \right] V_\ell^{(p)}(r) + 2\mu \int_0^R dr' W(r, r') V_\ell^{(p)}(r') = 0, \quad (2.47)$$

where $\gamma = 2\mu\alpha Z_1 Z_2$. Here $V_\ell^{(p)}(r)$ is the rescaled radial wave function of a two-body system of charged particles,

$$V_\ell^{(p)}(r) = r \cdot R_\ell^{(p)}(r). \quad (2.48)$$

We choose a normalization such that, for $r > R$, $V_\ell^{(p)}(r)$ is

$$\begin{aligned} V_\ell^{(p)}(r) &= p^\ell C_{\eta,\ell} \left[\cot \tilde{\delta}_\ell(p) \times F_\ell^{(p)}(r) + G_\ell^{(p)}(r) \right], \\ &= p^{2\ell+1} C_{\eta,\ell}^2 \cot \tilde{\delta}_\ell(p) \times f_\ell(p, r) + g_\ell(p, r), \end{aligned} \quad (2.49)$$

where $F_\ell^{(p)}(r)$ and $G_\ell^{(p)}(r)$ are the regular and irregular Coulomb wave functions, and the related functions $f_\ell(p, r)$ and $g_\ell(p, r)$ are defined for later convenience as

$$f_\ell(p, r) = \frac{1}{p^{\ell+1} C_{\eta,\ell}} F_\ell^{(p)}(r), \quad (2.50)$$

$$g_\ell(p, r) = p^\ell C_{\eta,\ell} G_\ell^{(p)}(r) = \tilde{g}_\ell(p, r) + \left[\gamma \tilde{h}_\ell(p) - ip^{2\ell+1} C_{\eta,\ell}^2 \right] f_\ell(p, r). \quad (2.51)$$

See Appendix A.2 for the functions $f_\ell(p, r)$, $g_\ell(p, r)$ and $\tilde{g}_\ell(p, r)$. The factor $C_{\eta,\ell}$ is given by

$$C_{\eta,\ell}^2 = \frac{2^{2\ell}}{\Gamma(2\ell+2)^2} \prod_{s=1}^{\ell} (s^2 + \eta^2) C_{\eta,0}^2, \quad (2.52)$$

and the function $\tilde{h}_\ell(p)$ is defined as

$$\tilde{h}_\ell(p) = \frac{(2p)^{2\ell}}{\Gamma(2\ell+2)^2} \frac{|\Gamma(\ell+1+i\eta)|^2}{|\Gamma(1+i\eta)|^2} \left[\psi(i\eta) + \frac{1}{2i\eta} - \log(i\eta) \right], \quad (2.53)$$

where

$$\eta = \frac{\gamma}{2p}, \quad (2.54)$$

$$C_{\eta,0}^2 = \frac{2\pi\eta}{e^{2\pi\eta} - 1}, \quad (2.55)$$

and $\psi(z)$ is the digamma function. Using these new expressions given in Eqs.(2.50)-(2.55), we can rewrite Eq. (2.49) as,

$$V_\ell^{(p)}(r) = \left[p^{2\ell+1} C_{\eta,\ell}^2 \left(\cot \tilde{\delta}_\ell(p) - i \right) + \gamma \tilde{h}_\ell(p) \right] \times f_\ell(p, r) + \tilde{g}_\ell(p, r), \quad (2.56)$$

The expression in square brackets is the modified Coulomb effective range expansion [21],

$$p^{2\ell+1} C_{\eta,\ell}^2 \left(\cot \tilde{\delta}_\ell(p) - i \right) + \gamma \tilde{h}_\ell(p) = \frac{-1}{a_\ell^c} + \frac{1}{2} r_\ell^c p^2 + P_\ell^c p^4 + Q_\ell^c p^6 + \mathcal{O}(p^8). \quad (2.57)$$

Finally, the Coulomb wave function is written as an expansion in powers of p^2 ,

$$V_\ell^{(p)}(r) = v_{0,\ell}(r) + v_{2,\ell}(r) p^2 + v_{4,\ell}(r) p^4 + v_{6,\ell}(r) p^6 + \mathcal{O}(p^8), \quad (2.58)$$

where $v(r)$'s are written in terms of the modified Coulomb effective range expansion parameters,

$$v_{0,\ell}(r) = \frac{-1}{a_\ell^c} f_{0,\ell}(r) + g_{0,\ell}(r), \quad (2.59)$$

$$v_{2,\ell}(r) = \frac{1}{2} r_\ell^c f_{0,\ell}(r) - \frac{1}{a_\ell^c} f_{2,\ell}(r) + g_{2,\ell}(r), \quad (2.60)$$

$$v_{4,\ell}(r) = P_\ell^c f_{0,\ell}(r) + \frac{1}{2} r_\ell^c f_{2,\ell}(r) - \frac{1}{a_\ell^c} f_{4,\ell}(r) + g_{4,\ell}(r), \quad (2.61)$$

$$v_{6,\ell}(r) = Q_\ell^c f_{0,\ell}(r) + P_\ell^c f_{2,\ell}(r) + \frac{1}{2} r_\ell^c f_{4,\ell}(r) - \frac{1}{a_\ell^c} f_{6,\ell}(r) + g_{6,\ell}(r). \quad (2.62)$$

2.5.3 Wronskian integral formula

In this section we follow the steps in Ref. [95] and derive the Wronskian integral formula for a two-particle system. We consider two solutions of Eq. (2.39) for momentum p_a and p_b ,

$$\left[-\frac{d^2}{dr^2} + \frac{\ell(\ell+1)}{r^2} - p_a^2 \right] U_a(r) + 2\mu \int_0^R dr' W(r, r') U_a(r') = 0, \quad (2.63)$$

$$\left[-\frac{d^2}{dr^2} + \frac{\ell(\ell+1)}{r^2} - p_b^2 \right] U_b(r) + 2\mu \int_0^R dr' W(r, r') U_b(r') = 0, \quad (2.64)$$

where we use the shorthand notation $U_a(r) = U_\ell^{(p_a)}(r)$ and $U_b(r) = U_\ell^{(p_b)}(r)$. We multiply Eq. (2.63) by $V_b(r)$ on the left, Eq. (2.64) by $V_a(r)$, and then subtracting the resulting equations yields

$$\begin{aligned} & U_a(r)U_b'(r) - U_b(r)U_a'(r) + (p_b^2 - p_a^2) U_b(r)U_a(r) \\ &= 2\mu \int_0^R dr' [U_a(r)W(r, r')U_b(r') - U_b(r)W(r, r')U_a(r')]. \end{aligned} \quad (2.65)$$

Integrating Eq. (2.65) from radius ρ to some radius $r \geq R$, we get

$$\begin{aligned} & [U_a U_b'' - U_b U_a'']|_{\rho}^r + (p_b^2 - p_a^2) \int_0^R dr' U_b(r') U_a(r') \\ &= 2\mu \int_{\rho}^R dr \int_0^R dr' [U_a(r) W(r, r') U_b(r') - U_b(r) W(r, r') U_a(r')] . \end{aligned} \quad (2.66)$$

Now for the right hand side of this equation using the condition given in Eq. (2.30), we finally obtain the Wronskian integral formula,

$$\frac{W[U_{\ell}^{(p_b)}, U_{\ell}^{(p_a)}](r)}{p_b^2 - p_a^2} = \int_0^r U_{\ell}^{(p_a)}(r') U_{\ell}^{(p_b)}(r') dr' . \quad (2.67)$$

In the low energy regime, when we set $p_a = p_b = p$, Eq. (2.67) reads

$$\begin{aligned} & W[u_{2,\ell}, u_{0,\ell}](r) + 2p^2 W[u_{4,\ell}, u_{0,\ell}](r) + p^4 W[u_{4,\ell}, u_{2,\ell}](r) \\ &+ 3p^4 W[u_{6,\ell}, u_{0,\ell}](r) - \int_0^r [U_{\ell}^{(p)}(r')]^2 dr' + \mathcal{O}(p^6) = 0 . \end{aligned} \quad (2.68)$$

In Appendix B.1 the Wronskians of the functions $u_n(r)$ are given in terms of the scattering parameters.

The integral terms can be rearranged and rewritten as

$$\int_0^r [U_{\ell}^{(p)}(r')]^2 dr' = \int_0^{\infty} [U_{\ell}^{(p)}(r')]^2 dr' - \int_r^{\infty} [U_{\ell}^{(p)}(r')]^2 dr' . \quad (2.69)$$

Since Eq. (2.42) is the solution of the function $U_{\ell}^{(p)}(r)$ for $r > R$, it can be used in the second

integral of the right hand side. Inserting Eq. (2.42) and Eq. (B.2)-(B.5) into Eq. (2.68) we get³

$$\int_0^\infty \left[U_\ell^{(p)}(r') \right]^2 dr' = -\frac{r_\ell}{2} + \Delta_{1,\ell} - 2(P_\ell - \Delta_{2,\ell}) p^2 - 3 \left(Q_\ell - \Delta_{3,\ell} - \frac{\Delta_{4,\ell}}{3} \right) p^4 + \mathcal{O}(p^6), \quad (2.70)$$

where $\Delta_{n,\ell}$ are integration constants and calculated from the following equations,

$$\Delta_{1,\ell} = \frac{1}{2} \frac{d}{dr} b_{1,\ell}(r) + \int_r^\infty dr' [u_{0,\ell}(r')]^2, \quad (2.71)$$

$$\Delta_{2,\ell} = \frac{d}{dr} b_{2,\ell}(r) + \int_r^\infty dr' [u_{2,\ell}(r') u_{0,\ell}(r')], \quad (2.72)$$

$$\Delta_{3,\ell} = \frac{d}{dr} b_{3,\ell}(r) + \int_r^\infty dr' [u_{4,\ell}(r') u_{0,\ell}(r')], \quad (2.73)$$

$$\Delta_{4,\ell} = \frac{d}{dr} b_{4,\ell}(r) + \int_r^\infty dr' [u_{2,\ell}(r')]^2 - \int_r^\infty dr' [u_{4,\ell}(r') u_{0,\ell}(r')], \quad (2.74)$$

where the $b_{n,\ell}(r)$ functions are given in Appendix B.1.

³Eq. (2.67)-(2.74) are valid for Coulomb case. In that case, $U_\ell^{(p)}(r)$ and $u_{n,\ell}(r)$ are replaced by $V_\ell^{(p)}(r)$ and $v_{n,\ell}(r)$, respectively. In addition, a superscript c is used in the scattering parameters to denote the Coulomb scattering parameters ($a_\ell^c, r_\ell^c, P_\ell^c$ and Q_ℓ^c).

2.6 Loosely bound systems

2.6.1 Asymptotic Normalization Coefficients

2.6.1.1 Neutral case

The bound state wave function with momentum $p = i\kappa$ in the asymptotic region is

$$\psi_\ell(r) = i^\ell A h_\ell^{(1)}(i\kappa r) \quad (2.75)$$

where A is the asymptotic normalization coefficient (ANC) and $h_\ell^{(1)}$ is the Riccati Hankel function. The bound state solution is normalized according to

$$\int_0^\infty [\psi_\ell(r')]^2 dr' = 1. \quad (2.76)$$

Furthermore, for the bound state regime, we have

$$\cot \delta_\ell(i\kappa) = i, \quad (2.77)$$

and the effective range expansion reads

$$(-1)^\ell \kappa^{2\ell+1} = \frac{1}{a_\ell} + \frac{1}{2} r_\ell \kappa^2 - P_\ell \kappa^4 + Q_\ell \kappa^6 + \mathcal{O}(\kappa^8), \quad (2.78)$$

Table 2.1 The integration constants $\Delta_{n,\ell}$ of a two-neutral-particles system for $\ell \leq 2$.

ℓ	$\Delta_{1,\ell}$	$\Delta_{2,\ell}$	$\Delta_{3,\ell}$	$\Delta_{4,\ell}$
0	$\frac{\kappa}{2}$	0	0	0
1	$-\frac{3\kappa^3}{2}$	0	0	0
2	$\frac{5\kappa^5}{2}$	0	0	0

The relation between $\psi_\ell(r)$ and $U_\ell^{(i\kappa)}(r)$ can be obtained, for $r > R$,

$$\begin{aligned}
 U_\ell^{(i\kappa)}(r) &= (i\kappa)^\ell [\cot \delta_\ell(i\kappa) \times S_\ell(i\kappa r) + C_\ell(i\kappa r)] \\
 &= (i\kappa)^\ell [i \times S_\ell(i\kappa r) + C_\ell(i\kappa r)] = (i\kappa)^\ell h_\ell^{(1)}(i\kappa r) = \frac{\kappa^\ell}{A} \psi_\ell(r) \quad (2.79)
 \end{aligned}$$

Inserting Eq. (2.79) into the integral term of Eq. (2.70) we obtain the following expression for the ANC

$$A_\ell \approx \frac{\kappa^\ell}{\sqrt{-\frac{r_\ell}{2} + \Delta_{1,\ell} + 2(P_\ell - \Delta_{2,\ell}) \kappa^2 - 3\left(Q_\ell - \Delta_{3,\ell} - \frac{\Delta_{4,\ell}}{3}\right) \kappa^4}}, \quad (2.80)$$

where integration constants $\Delta_{n,\ell}$ are given in Table 2.1. An alternative expression can be obtained by eliminating the effective range r_ℓ using Eq. (2.78)

$$A_\ell \approx \frac{\kappa^{\ell+1}}{\sqrt{\frac{1}{a_\ell} - (-1)^\ell \kappa^{2\ell+1} + \Delta_{1,\ell} \kappa^2 + (P_\ell - 2\Delta_{2,\ell}) \kappa^4 - (2Q_\ell - 3\Delta_{3,\ell} - \Delta_{4,\ell}) \kappa^6}}. \quad (2.81)$$

This expression agrees with Eq.(11) of Ref. [108] up to the given order.

2.6.1.2 Coulomb case

The bound state Coulomb wave function with binding momentum κ in the asymptotic region is

$$\psi_\ell^c(r) = A^c W_{-i\eta, \ell + \frac{1}{2}}(2\kappa r) \quad (2.82)$$

where A^c is the Coulomb-ANC and $W_{-i\eta, \ell + \frac{1}{2}}$ is the Whittaker function. The bound state solution is normalized according to

$$\int_0^\infty [\psi_\ell^c(r')]^2 dr' = 1. \quad (2.83)$$

In the bound state regime, we have

$$\cot \tilde{\delta}_\ell(i\kappa) = i. \quad (2.84)$$

Therefore, the wave function becomes, for $r > R$,

$$\begin{aligned} V_\ell^{(i\kappa)}(r) &= (i\kappa)^\ell C_{\eta, \ell} \left[iF_\ell^{(i\kappa)}(r) + G_\ell^{(i\kappa)}(r) \right] \\ &= (i\kappa)^\ell C_{\eta, \ell} e^{i\sigma_\ell} e^{-i\pi(\ell + i\eta)} W_{-i\eta, \ell + \frac{1}{2}}(2\kappa r), \end{aligned} \quad (2.85)$$

where σ_ℓ is the Coulomb phase shift,

$$e^{i\sigma_\ell} = \frac{\Gamma(\ell + 1 + i\eta)}{\Gamma(\ell + 1 - i\eta)}. \quad (2.86)$$

The wave function $V_\ell^{(i\kappa)}(r)$ in terms of the bound state Coulomb wave function reads

$$V_\ell^{(i\kappa)}(r) = \frac{\kappa^\ell}{A^c} \tilde{C}_{\eta,\ell} \psi_\ell^c(r), \quad (2.87)$$

where

$$\tilde{C}_{\eta,\ell} = \frac{2^\ell \Gamma(\ell + 1 + i\eta)}{\Gamma(2\ell + 2)}. \quad (2.88)$$

Finally, the ANC can be written as

$$|A_\ell^c| \approx \frac{\kappa^\ell \tilde{C}_{\eta,\ell}}{\left[-\frac{r_\ell^c}{2} + \Delta_{1,\ell}^c + 2 \left(P_\ell^c - \Delta_{2,\ell}^c \right) \kappa^2 - 3 \left(Q_\ell^c - \Delta_{3,\ell}^c - \frac{\Delta_{4,\ell}^c}{3} \right) \kappa^4 \right]^{1/2}}. \quad (2.89)$$

Integration constants $\Delta_{n,\ell}^c$ for $\ell \leq 2$ in the Coulomb case are given in Table 2.2.

Table 2.2 Integration constants $\Delta_{n,\ell}^c$ calculated from Eqs. (2.71)-(2.74) for $\ell \leq 2$ in Coulomb case .

ℓ	$\Delta_{1,\ell}^c$	$\Delta_{2,\ell}^c$	$\Delta_{3,\ell}^c$	$\Delta_{4,\ell}^c$
0	$\frac{1}{3\gamma}$	$\frac{2}{15\gamma^3}$	$\frac{16}{63\gamma^5}$	0
1	$\frac{\gamma}{108}$	$\frac{11}{270\gamma}$	$\frac{62}{2835\gamma^3}$	0
2	$\frac{\gamma^3}{43200}$	$\frac{17\gamma}{36000}$	$\frac{191}{113400\gamma}$	0

An alternative expression for A^c can be found by eliminating the effective range parameter r_ℓ^c in Eq. (2.89) using the Coulomb modified effective range expansion in the bound state regime,

$$\gamma \tilde{h}_\ell(i\kappa) = \frac{-1}{a_\ell^c} - \frac{1}{2} r_\ell^c \kappa^2 + P_\ell^c \kappa^4 - Q_\ell^c \kappa^6 + \mathcal{O}(k^8), \quad (2.90)$$

where $\gamma\tilde{h}_\ell(i\kappa)$ are given in Table 2.3 for $\ell \leq 2$. We find

Table 2.3 The function $\gamma\tilde{h}_\ell(i\kappa)$ in the Coulomb modified effective range expansion for $\ell \leq 2$.

ℓ	$\gamma\tilde{h}_\ell(i\kappa)$
0	$-\frac{\kappa^2}{3\gamma} + \frac{2\kappa^4}{15\gamma^3} - \frac{16\kappa^6}{63\gamma^5} + \mathcal{O}(\kappa^8)$
1	$-\frac{\gamma\kappa^2}{108} + \frac{11\kappa^4}{270\gamma} - \frac{62\kappa^6}{2835\gamma^3} + \mathcal{O}(\kappa^8)$
2	$-\frac{\gamma^3\kappa^2}{43200} + \frac{17\gamma\kappa^4}{36000} - \frac{191\kappa^6}{113400\gamma} + \mathcal{O}(\kappa^8)$

$$|A_\ell^c| \approx \frac{\kappa^{\ell+1}\tilde{C}_{\eta,\ell}}{\left[\frac{1}{a_\ell^c} + \gamma\tilde{h}_\ell(i\kappa) + \Delta_{1,\ell}^c\kappa^2 + \left(P_\ell^c - 2\Delta_{2,\ell}^c\right)\kappa^4 - \left(2Q_\ell^c - 3\Delta_{3,\ell}^c - \Delta_{4,\ell}^c\right)\kappa^6\right]^{1/2}} \quad (2.91)$$

This expression matches with Eq. (85) of Ref. [107] [cf. Eq.(5.87) of Ref.[105]] up to the given order and Eq. (21) of Ref. [159] for $\ell = 2$. The relation between our convention of the effective range parameters and the convention of Ref. [159] is

$$\tilde{A}^c = \left(\frac{2^\ell \ell!}{\Gamma(2\ell + 2)}\right)^2 A^c. \quad (2.92)$$

Lattice Effective Field Theory

3.1 Introduction

In the first theoretical descriptions initiated by Yukawa [178] the strong nuclear forces between nucleons are mediated by massive bosons called mesons. Phenomenological models which were only based on one-boson-exchange (OBE) well described the strong interactions at large distances [34, 64, 134]. Later, efforts were made to construct highly sophisticated potential models in order to improve the shape of the potentials in intermediate ranges [98, 115, 162, 176, 126]. For more on potential models and a historical review see Ref. [128, 127].

At the same time attempts were taken to describe the strong interactions between nucleons within the framework of quantum field theory (QFT), and a breakthrough came with the discovery of quarks [84]. Quarks are elementary particles in the Standard Model and they are constituents of hadrons. The theory of the strong interactions is called quantum chromodynamics (QCD). The fundamental degrees of freedom in QCD are gluons as well as quarks. Quarks have six different flavors (up, down, strange, charmed, top, bottom) and three colors (red, green, blue). Colors are the charges of quarks, and the strong interactions are governed by a non-abelian

gauge theory with the SU(3)-color group [69, 70]. The eight generators of the SU(3) group correspond with the eight gluons.

The running coupling constant of the strong interactions makes it possible to carry out calculations of observables perturbatively at higher energies. However, the same feature of the theory causes a breakdown in perturbative treatments at low energies. This clearly manifests the necessity of non-perturbative methods in order to predict observables from QCD. An elegant method was proposed by Wilson [175]. He formulated lattice gauge theory on a discretized space-time lattice, which is commonly known as lattice QCD (LQCD), and this method gave access to study QCD in the low energy limit or at large distances using numerical methods. Therefore, LQCD has become a powerful approach to probe the structure of hadrons using quarks and gluons as degrees of freedom [8, 67]. Also, LQCD has been used for studying elastic scattering of meson-mesons [114, 1, 121, 6, 4, 7], meson-baryon [72], and baryon-baryon [9, 3, 97, 5].

Another direct approach to access the low-energy regime of QCD is effective field theory (EFT) which is based upon the seminal work of Weinberg [171]. This idea is rooted in a general concept of separation of scales. Physical processes and observables are well defined in energy scales relevant to the dynamics of the system. In the low energy limit of QCD since quarks and gluons are strongly confined in hadrons by color charge forces, the relevant degrees of freedom at large distance scales are hadrons, instead of quarks and gluons. Therefore, a scale separation is inevitable here and it is indeed the key point of EFT. The spectrum of hadrons shows a visible large gap between the masses of light mesons (π^0, π^\pm) and the masses of nucleons (N) and heavier mesons. The EFT formulation sets a soft scale Q at the mass scale of light mesons and a hard scale Λ at the scale of the nucleon mass. Then using EFT one can perform systematic calculations as an expansion in powers of a small parameter Q/Λ . This formulation is known as chiral effective field theory (χ EFT).

The hard scale Λ also corresponds to the spontaneous chiral symmetry breaking scale. Chiral

symmetry is a symmetry of QCD associated with the smallness of the light quark masses. In the limit of zero quark mass, one can do independent unitary transformations of the left and the right components of the quarks. Chiral EFT enforces the fact that chiral symmetry must be manifested in the phenomenology of hadrons at low energies. Chiral EFT was first applied to the elastic scattering of $\pi\pi$ [81] and πN [82]. Later, its applicability to the nuclear structure and interactions was derived by Weinberg [172, 173]. Refs. [127] and [56] provide detailed reviews on the subject.

In such systems where momenta is smaller than the pion mass the pionless effective field theory ($\not{\pi}$ EFT) is a more economic and efficient formulation to use. In the $\not{\pi}$ EFT pions are integrated out and the interactions are only local contact interactions between dynamical nucleons [167, 11, 12, 13, 38, 145, 96]. For example, the deuteron binding momentum is $\gamma_d = 45$ MeV which is much smaller than the lightest pion mass $m_\pi = 140$ MeV. This clearly suggests here that the pion mass can be considered as the hard scale here since the relevant energy scale is much lower than the pion mass.

Interactions derived from EFT mentioned above have been combined with powerful numerical methods to study low energy nuclear physics from first principles. This growing field is known as lattice effective field theory (lattice EFT). Lattice EFT was formulated on discretized space-time from the chiral EFT [23]. Ref. [118] provides a detailed review of lattice EFT from the $\not{\pi}$ EFT and chiral EFT. In the last decade lattice EFT methods have proven its successes with significant contributions made to nuclear structure studies [22, 24, 62, 57]. Some recent successes of lattice EFT are the *ab initio* calculation of Hoyle state of carbon-12 [63], which is the states that is responsible for the carbon-12 production in the stars, and *ab initio* calculation of the spectrum and structure of ^{16}O [60]. Also, very recently these calculations have been extended to medium mass nuclei [116]. Nuclear reaction calculations from lattice EFT were initiated by Ref. [154].

3.2 The path integral

Following Dirac's pioneer work [48] that suggested that there is a connection between the exponent of the classical action $e^{iS[q(t)]}$ and the transition amplitude of a quantum mechanical particle at two points, Feynman was the first who incorporated classical Lagrangian approaches into quantum mechanics [65]. With his work, Feynman reformulated quantum mechanics and quantum field theory by the so called *path integral* (PI) method. The PI formulation has brought particular advantages in quantum field theories and become very a important tool for numerical techniques in quantum systems.

Starting with the time evolution operator e^{-iHt} in the Hamiltonian formalism, the transition amplitude of a quantum mechanical particle from an initial point q_I to a final point q_F is defined by

$$\langle q_F | e^{-iHt} | q_I \rangle, \quad (3.1)$$

where $|q\rangle$ denote the complete set of states in the Dirac bra-ket notation $1 = \int dq |q\rangle \langle q|$. Now, we want to obtain an expression from Eq. (3.1) in a path integral form. To achieve this we split the time t into L_t equal segments $\alpha_t = t/L_t$ and rewrite the evolution operator e^{-iHt} as L_t products of $e^{-iH\alpha_t}$. By insertion of the completeness relations between those segmented operators, Eq. (3.1) becomes the products of the transition amplitudes (the propagators) at two

points over a small time segment α_t ,

$$\begin{aligned} \langle q_F | e^{-iHt} | q_I \rangle &= \int \dots \int dq_1 dq_2 \dots dq_{L_t-2} dq_{L_t-1} \\ &\quad \times \langle q_F | e^{-iH\alpha_t} | q_{L_t-1} \rangle \langle q_{L_t-1} | e^{-iH\alpha_t} | q_{L_t-2} \rangle \dots \\ &\quad \dots \times \langle q_3 | e^{-iH\alpha_t} | q_2 \rangle \langle q_2 | e^{-iH\alpha_t} | q_1 \rangle \langle q_1 | e^{-iH\alpha_t} | q_I \rangle. \end{aligned} \quad (3.2)$$

An individual propagator for the Hamiltonian $H = \frac{\hat{p}^2}{2m} + V(\hat{q})$ which describes a particle in a potential $V(\hat{q})$ is of the following form,

$$\langle q_{n+1} | e^{-iH\alpha_t} | q_n \rangle = \langle q_{n+1} | e^{-i\frac{\hat{p}^2}{2m}\alpha_t} | q_n \rangle e^{-iV(q_n)\alpha_t} \quad (3.3)$$

$$= \sqrt{\frac{-im}{2\pi\alpha_t}} e^{i\frac{m\alpha_t}{2} \left(\frac{q_{n+1}-q_n}{\alpha_t} \right)^2} e^{-iV(q_n)\alpha_t}. \quad (3.4)$$

This is an infinitesimal transition amplitude which describes the particle's evolution from q_{n+1} to q_n . In Eq. (3.3) we use the Baker-Campbell-Hausdorff formula¹, and from Eq. (3.3) to Eq. (3.4) we use the state $|p\rangle$ which is the eigenstate of \hat{p} and whose normalization is such that $\int \frac{dp}{2\pi} |p\rangle \langle p| = 1$. Plugging in the individual propagator given by Eq. (3.4) into Eq. (3.2) we get

$$\langle q_F | e^{-iHt} | q_I \rangle = \left(\frac{-im}{2\pi\alpha_t} \right)^{L_t/2} \int \prod_{n=1}^{L_t-1} dq_n \exp \left\{ i\alpha_t \sum_{k=0}^{N-1} \left[\frac{m}{2} \left(\frac{q_{k+1}-q_k}{\alpha_t} \right)^2 - V(q_k) \right] \right\}, \quad (3.5)$$

and in the continuum limit $\alpha_t \rightarrow 0$ Eq. (3.5) is

$$\langle q_F | e^{-iHt} | q_I \rangle = \int \mathcal{D}q(t) e^{iS[q(t)]}, \quad (3.6)$$

¹ $e^{A+B+\frac{1}{2}[A,B]+\dots} = e^A e^B$

where the short-hand notation for the integral over all paths is

$$\int \mathcal{D}q(t) = \left(\frac{-im}{2\pi\alpha_t} \right)^{L_t/2} \left(\prod_{n=1}^{L_t-1} dq_n \int \right) \quad (3.7)$$

and $S[q(t)]$ is the action defined in terms of the classical Lagrangian $L(q, \dot{q}, t) = \frac{m}{2}\dot{q}^2 - V(q)$,

$$\exp iS[q(t)] = \exp i \int dt L(q, \dot{q}, t). \quad (3.8)$$

In this formalism the classical Lagrangian is the fundamental quantity. Eq. (3.6) is the Feynman PI formulation which reformulates the quantum mechanical amplitude as the integral over all possible paths weighted by e^{iS} .

The weighting function in the PI has an oscillatory nature. For later convenience and the favor of numerical methods to be employed we want to suppress these oscillations and desire the weighting function to be positive semi-definite and non-oscillating. Therefore, rotation² to the Euclidean time direction $it \rightarrow \tau$ is a crucial step to obtain the Euclidean action S_E ,

$$S_E[q(\tau)] = \int d\tau L_E(q, \dot{q}, \tau) = \int d\tau \left[\frac{m}{2}\dot{q}^2 + V(q) \right], \quad (3.9)$$

and the Euclidean time formulation of the PI becomes

$$\langle q_F | e^{-iHt} | q_I \rangle = \langle q_F | e^{-H\tau} | q_I \rangle = \int \mathcal{D}q(\tau) e^{-S_E[q(\tau)]}. \quad (3.10)$$

The PI formulations derived above hold for any quantum system as well as quantum field theory. Eq. (3.10) can be rearranged according to the following table,

²This is the so called Wick rotation. The integrand of the action is rotated from the $\text{Re } t$ axis to the $\text{Im } t$ in the complex t -plane.

$$q(\tau) \rightarrow \phi(\vec{r})$$

$$S_E[q(\tau)] \rightarrow S_E(\phi)$$

$$\int \mathcal{D}q(\tau) \rightarrow \int \mathcal{D}\phi$$

and the PI formulation for fields becomes

$$\langle \phi_F(\vec{r}) | e^{-H\tau} | \phi_I(\vec{r}) \rangle = \int \mathcal{D}\phi e^{-S_E(\phi)}. \quad (3.11)$$

Here ϕ is the field amplitude which is the dynamical variable of quantum field theory, and the euclidean action $S_E(\phi)$ is defined in terms of the Lagrangian in the non-relativistic limit of quantum field theory with

$$\begin{aligned} \mathcal{L}_E = & -\phi^\dagger \frac{\partial}{\partial \tau} \phi - \frac{1}{2m} (\nabla \phi^\dagger) \cdot (\nabla \phi) \\ & - \int d^3\vec{r}' \phi^\dagger(\vec{r}) \phi(\vec{r}) V(\vec{r} - \vec{r}') \phi^\dagger(\vec{r}') \phi(\vec{r}') \end{aligned} \quad (3.12)$$

with the density operator

$$\rho(\vec{r}) = \phi^\dagger(\vec{r}) \phi(\vec{r}). \quad (3.13)$$

The Hamiltonian of the Schrödinger field equation is

$$H = \int d^3\vec{r} \left[\pi(\vec{r}) \frac{\partial}{\partial \tau} \phi(\vec{r}) - \mathcal{L}_E \right] = H_0 + H_V, \quad (3.14)$$

where $\pi(\vec{r}) = \frac{\partial \mathcal{L}}{\partial(\partial\phi/\partial\tau)}$ is the momentum density conjugate to $\phi(\vec{r})$, H_0 is the free Hamiltonian

$$H_0 = \frac{1}{2m} \int d^3\vec{r} \nabla\phi^\dagger(\vec{r}) \cdot \nabla\phi(\vec{r}), \quad (3.15)$$

and H_V is the interaction term

$$H_V = \int \int d^3\vec{r} d^3\vec{r}' \rho(\vec{r}) V(\vec{r} - \vec{r}') \rho(\vec{r}'). \quad (3.16)$$

3.3 Grassmann variables

The quantizations of bosonic fields are based upon the commutation relation, while only the anti-commutation relation yields a consistent theory for the fermionic fields. See Refs.[179, 141] for details and comprehensive discussions on the topic.

The anti-commuting variables that we are in need of are Grassmann variables. In order to study the PI for fermions we necessarily reconsider Eqs.(3.11)-(3.14) in terms of Grassmann variables. Therefore, we discuss some basic properties of Grassmann variables, and their integration and differentiation are introduced.

Let η_k for $l = 1, 2, \dots, N$ be a set of Grassmann variables which satisfy the anti-commutation relation

$$\eta_k \eta_l + \eta_l \eta_k \equiv \{\eta_k, \eta_l\} = 0, \quad (3.17)$$

for any k and l . Eq. (3.17) imposes that $\eta_k^2 = 0$. Assuming that Grassmann variables can be expanded in a Taylor series, the most general function of a Grassmann variable has the form $f(\eta) = a + b\eta$ where a and b are ordinary numbers.

The left and right differentiation of Grassmann variables are defined as

$$\frac{\overrightarrow{\partial}}{\partial \eta_k} \eta_l = -\eta_l \frac{\overleftarrow{\partial}}{\partial \eta_k} = \delta_{kl}, \quad (3.18)$$

and using this we can write

$$\frac{\overrightarrow{\partial}}{\partial \eta_k} \eta_l \eta_k = -\eta_l = \eta_l \eta_k \frac{\overleftarrow{\partial}}{\partial \eta_k}. \quad (3.19)$$

We use the standard notation for Grassmann variables so that the integration can be written by

$$\int d\eta_k 1 = 0 \quad \text{and} \quad \int d\eta_k \eta_k = - \int \eta_k d\eta_k = 1. \quad (3.20)$$

A complex Grassmann variable can be written as a combination of two real Grassmann variables, $\theta = \eta_k + i\eta_l$. The properties of the complex Grassmann variables can be defined by using the properties of real Grassmann variables above,

$$\theta^2 = \theta^{*2} = 0 \quad \text{and} \quad \theta^* \theta = i[\eta_k, \eta_l], \quad (3.21)$$

where $\theta^* = \eta_k - i\eta_l$. Ref. [163] provides detailed discussions on Grassmann algebra and some interesting physics applications of Grassmann variables.

3.4 Lattice formulation

In this section by following Ref. [118, 117] we introduce a lattice formalism in which spacetime is a discretized periodic cubic lattice with $L^3 \times L_t$ points. In the lattice formalism of our discussion, the lattice spatial spacing is denoted by a , and the lattice temporal spacing is a_t .

Also, we introduce $\alpha_t = a_t/a$ as the ratio of temporal lattice spacing to spacial lattice spacing. Here we use dimensionless parameters and physical quantities in lattice units multiplied by the appropriate power of a .

We consider two-component fermions interacting via zero-range potentials, and we call the two components \uparrow and \downarrow spins. The PI for fermions is defined by the anti-commuting Grassmann variables on lattice,

$$Z = \int \left[\prod_{n_t, \vec{n}, s=\uparrow, \downarrow} d\theta_s(n_t, \vec{n}) d\theta_s^*(n_t, \vec{n}) \right] e^{-S[\theta, \theta^*]}. \quad (3.22)$$

Grassmann variables are periodic along the spatial direction,

$$\theta(\vec{n} + L, n_t) = \theta(\vec{n}, n_t) \quad \theta^*(\vec{n} + L, n_t) = \theta^*(\vec{n}, n_t), \quad (3.23)$$

and anti-periodic in the temporal direction,

$$\theta(\vec{n}, n_t + L_t) = -\theta(\vec{n}, n_t) \quad \theta^*(\vec{n}, n_t + L_t) = -\theta^*(\vec{n}, n_t). \quad (3.24)$$

The non-relativistic lattice action is defined by

$$S[\theta, \theta^*] = \sum_{n_t} \{S_t[\theta, \theta^*, n_t] + S_{H_0}[\theta, \theta^*, n_t] + S_V[\theta, \theta^*, n_t]\}, \quad (3.25)$$

where S_t and S_{H_0} contain temporal hopping and spatial hopping terms of the free lattice action respectively,

$$S_t[\theta, \theta^*, n_t] = \sum_{s=\uparrow, \downarrow} \sum_{\vec{n}} [\theta_s^*(n_t + \hat{0}, \vec{n}) \theta_s(n_t, \vec{n}) - \theta_s^*(n_t, \vec{n}) \theta_s(n_t, \vec{n})], \quad (3.26)$$

$$S_{H_0}[\theta, \theta^*, n_t] = \frac{\alpha_t}{2m} \sum_{s=\uparrow, \downarrow} \sum_{\vec{n}} \sum_{l=1}^3 \theta_s^*(n_t, \vec{n}) [2\theta_s(n_t, \vec{n}) - \theta_s(n_t, \vec{n} + \hat{l}) - \theta_s(n_t, \vec{n} - \hat{l})]. \quad (3.27)$$

Here $\hat{0}$ denotes the lattice unit vector in the forward temporal direction. We can also write

$$S_{H_0}[\theta, \theta^*, n_t] = \alpha_t H_0^\uparrow[\theta_s, \theta_s^*, n_t] + \alpha_t H_0^\downarrow[\theta_s, \theta_s^*, n_t], \quad (3.28)$$

and the interaction term $S_V[\theta, \theta^*, n_t]$ as

$$S_V[\theta, \theta^*, n_t] = \alpha_t H_V[\theta, \theta^*, n_t], \quad (3.29)$$

where

$$H_0^s[\theta_s, \theta_s^*, n_t] = \frac{1}{2m} \sum_{\vec{n}} \sum_{l=1}^3 \theta_s^*(n_t, \vec{n}) [2\theta_s(n_t, \vec{n}) - \theta_s(n_t, \vec{n} + \hat{l}) - \theta_s(n_t, \vec{n} - \hat{l})], \quad (3.30)$$

and

$$H_V[\theta, \theta^*, n_t] = C_0 \sum_{\vec{n}} \theta_\uparrow^*(n_t, \vec{n}) \theta_\uparrow(n_t, \vec{n}) \theta_\downarrow^*(n_t, \vec{n}) \theta_\downarrow(n_t, \vec{n}). \quad (3.31)$$

In the last equation C_0 is the coupling strength of the zero-range potential.

3.4.1 The transfer matrix

The Grassmann formalism given by Eq. (6.10) is convenient for deriving the lattice Feynman rules. On the other hand, the operator formalism or so called *transfer matrix* formalism is more convenient for numerical calculations. Therefore, in this section we review the connection between the PI formulation and the operator formalism in quantum mechanics [42].

As a first step we analyze the connection in quantum mechanics and rewrite Eq. (3.5) for the Euclidean time lattice,

$$Z = \int \mathcal{D}q(\alpha_t) \exp \left\{ -\alpha_t \sum_{n=0}^{L_t-1} \left[\frac{m}{2} \left(\frac{q_{n+1} - q_n}{\alpha_t} \right)^2 + V(q_n) \right] \right\}. \quad (3.32)$$

For finite lattice of L_t sites this expression can be rewritten in the form of

$$Z = \int \prod_{n=0}^{L_t-1} dq_n M_{n+1,n}. \quad (3.33)$$

where the matrix $M_{n+1,n}$ is the transfer matrix,

$$M_{n',n} = \left(\frac{m}{2\pi\alpha_t} \right)^{1/2} \exp \left[-\alpha_t \frac{m}{2} \left(\frac{q_{n'} - q_n}{\alpha_t} \right)^2 - \alpha_t V(q_n) \right]. \quad (3.34)$$

From Eqs. (3.3) and (3.4), we already know that $M_{n',n}$ describes the evolution of particles over one lattice spacing in the temporal direction

$$M_{n',n} = \langle q_{n+1} | e^{-\alpha_t H} | q_n \rangle. \quad (3.35)$$

It should be noted that the n, n' subscripts are not the matrix indices of the transfer matrix, but rather the coordinates of the particle.

Now we turn to the exact correspondence between the Grassmann path integral and the transfer matrix formalism. For the moment let us consider a single component fermion and use b and b^\dagger to denote fermion anti-commuting creation and annihilation operators, respectively,

$$\{b, b\} = \{b^\dagger, b^\dagger\} = 0, \quad \{b, b^\dagger\} = 1. \quad (3.36)$$

For any function $f(b, b^\dagger)$ the exact relation between the Grassmann path integral and the transfer matrix formalism is given by [44],

$$\text{Tr} \left[: f(b, b^\dagger) : \right] = \int d\theta^* d\theta e^{2\theta^* \theta} f(\theta^*, \theta), \quad (3.37)$$

where the symbol $::$ signifies normal ordering. Normal ordering rearranges operators between the symbol $::$ such that all annihilation operators are on the right and creation operators are on the left. Using anti-periodicity of Grassmann fields in temporal direction, i.e. $\theta(1) = -\theta(0)$, Eq. (3.37) can be rewritten as a path integral over a short time interval,

$$\text{Tr} \left[: f(b, b^\dagger) : \right] = \int d\theta^*(0) d\theta(0) e^{\theta^*(0)[\theta(0) - \theta(1)]} f(\theta^*(0), \theta(0)), \quad (3.38)$$

This can be applied to the product of any normal-ordered functions of different component fermion creation and annihilation operators, which leads to the following exact correspondence between the PI integral and operator formalism [43, 44],

$$\begin{aligned} & \text{Tr} \left[: f_{L_t-1} [b_{s'}^\dagger(\vec{n}'), b_s(\vec{n})] : \cdots : f_0 [b_{s'}^\dagger(\vec{n}'), b_s(\vec{n})] : \right] \\ &= \int \left[\prod_{n_t, \vec{n}, s=\uparrow, \downarrow} d\theta_s^*(n_t, \vec{n}) d\theta_s(n_t, \vec{n}) \right] e^{-S_t[\theta, \theta^*]} \prod_{n_t=0}^{L_t-1} f_{n_t} [\theta_{s'}^*(n_t, \vec{n}'), \theta_s(n_t, \vec{n})], \end{aligned} \quad (3.39)$$

Therefore the transfer matrix formulations of the path integral given in Eq. (3.22) has the the following form,

$$Z(L_t) = \text{Tr} [\hat{M}^{L_t}], \quad (3.40)$$

where \hat{M} is the normal-ordered transfer matrix operator,

$$\hat{M} =: \exp \left[-\alpha_t \hat{H}_0 - \alpha_t C_0 \sum_{\vec{n}} \hat{\rho}_\uparrow(\vec{n}) \hat{\rho}_\downarrow(\vec{n}) \right] : . \quad (3.41)$$

Here \hat{H}_0 is the free non-relativistic lattice Hamiltonian in terms of anti-commuting creation and annihilation operators

$$\hat{H}_0 = \hat{H}_0^\uparrow + \hat{H}_0^\downarrow, \quad (3.42)$$

where

$$\hat{H}_0^s = \frac{1}{2m} \sum_{\hat{l}=1}^3 \sum_{\vec{n}} \left[2b_s^\dagger(\vec{n})b_s(\vec{n}) - b_s^\dagger(\vec{n})b_s(\vec{n} + \hat{l}) - b_s^\dagger(\vec{n})b_s(\vec{n} - \hat{l}) \right], \quad (3.43)$$

and $\hat{\rho}_s$ are the lattice density operators,

$$\hat{\rho}_s(\vec{r}) = b_s^\dagger(\vec{r})b_s(\vec{r}). \quad (3.44)$$

s signify the spin component of fermions and \hat{l} denotes the spatial lattice unit vectors.

3.4.2 Adiabatic projection methods

The adiabatic projection method is a general procedure for calculating scattering and reactions on the lattice. The main tools of the method are initial cluster states of the system. By clusters we mean either a single particle or a composite state of several particles. The method constructs a low energy effective theory for clusters, and in the limit of large Euclidean time projection these cluster states will span the low-energy subspace of the Hamiltonian.

The initial cluster states can be parameterized by either the initial spatial separations [143]

or alternatively the relative momentum between clusters. The latter reduces the number of required initial states, and it is quite advantageous to adopt for improving the efficiency of the calculations. Let us use $|\Psi_{\vec{\rho}}\rangle$ to denote a set of initial cluster states where $\vec{\rho}$ stands for the parameters chosen to define the state, i.e., \vec{R} and \vec{p} . The dressed cluster states are formed by projecting the states $|\Psi_{\vec{\rho}}\rangle$ in the Euclidean time,

$$|\Psi_{\vec{\rho}}\rangle_t = e^{-\hat{H}t} |\Psi_{\vec{\rho}}\rangle \quad (3.45)$$

Now the adiabatic projection method uses these dressed cluster states to calculate the matrix elements of observables such as the Hamiltonian and the transfer matrix.

The dressed cluster states are generally non-orthogonal, and as a result of this the method involves calculating a norm matrix. As an example in the following we consider the calculation of the adiabatic matrix representation of the Hamiltonian operator \hat{H} by following the procedure used in Ref. [143]. Let us define the dual state ${}_t\langle\Psi_{\vec{\rho}}|$ written as a linear functional,

$${}_t\langle\Psi_{\vec{\rho}}|u\rangle = \sum_{\vec{\rho}'} {}_t\langle\Psi_{\vec{\rho}}|\Psi_{\vec{\rho}'}\rangle_t {}_t\langle\Psi_{\vec{\rho}'}|u\rangle, \quad (3.46)$$

such that the dual state ${}_t\langle\Psi_{\vec{\rho}}|$ satisfies that

$${}_t\langle\Psi_{\vec{\rho}}|u\rangle = 0 \quad \text{for all } \vec{\rho} \quad \Rightarrow \quad {}_t\langle\Psi_i|u\rangle = 0 \quad \text{for all } \vec{\rho} \quad (3.47)$$

$${}_t\langle\Psi_{\vec{\rho}}|\Psi_{\vec{\rho}'}\rangle_t = \delta_{\vec{\rho}\vec{\rho}'}. \quad (3.48)$$

The inner product of the propagated initial and final state is the norm matrix,

$$[N_t]_{\vec{\rho}\vec{\rho}'} = {}_t\langle\Psi_{\vec{\rho}}|\Psi_{\vec{\rho}'}\rangle_t. \quad (3.49)$$

and the inner product of the propagated initial and dual state defines

$${}_t\langle\Psi_{\bar{\rho}}|\Psi_{\bar{\rho}'}\rangle_t = [N_t^{-1}]_{\bar{\rho}\bar{\rho}'}. \quad (3.50)$$

Therefore, the adiabatic matrix of the Hamiltonian \hat{H} projected onto the set of dressed cluster states,

$$\begin{aligned} [\hat{H}_t^a]_{\bar{\rho}\bar{\rho}'} &= \sum_{\bar{\rho}''} {}_t\langle\Psi_{\bar{\rho}}|\Psi_{\bar{\rho}''}\rangle_t \langle\Psi_{\bar{\rho}''}|\hat{H}|\Psi_{\bar{\rho}'}\rangle_t \\ &= [N_t^{-1}]_{\bar{\rho}\bar{\rho}''} {}_t\langle\Psi_{\bar{\rho}''}|\hat{H}|\Psi_{\bar{\rho}'}\rangle_t. \end{aligned} \quad (3.51)$$

By using a similarity transformation, we can define the Hermitian adiabatic Hamiltonian as

$$[\hat{H}_t^a]_{\bar{\rho}\bar{\rho}'} = [N_t^{-1/2}]_{\bar{\rho}\bar{\rho}''} {}_t\langle\Psi_{\bar{\rho}''}|\hat{H}|\Psi_{\bar{\rho}'}\rangle_t [N_t^{-1/2}]_{\bar{\rho}''\bar{\rho}'}. \quad (3.52)$$

\hat{H}_t^a is the two-body adiabatic Hamiltonian describing the scattering and reactions between interacting clusters, and the calculations become systematically more accurate as the projection time t is increased. See Ref. [143] for detailed analysis on an estimate of the residual error as a function of the projection time.

3.5 Scattering phase shifts from the lattice

In the finite-volume calculation, we compute the volume dependent energy spectrum of the system. However, the information about the short-range interaction potentials between two clusters is encoded in the scattering phase shifts. Therefore, in the following we review the mathematical tools and methods that we use in order to determine the scattering phase shift in

finite volume calculations.

3.5.1 Cubic rotational group

In the discretized lattice the rotational symmetry cannot be explored using an arbitrary rotation angle since the $SO(3)$ rotational symmetry of continuum space is broken to the finite rotational group $SO(3, Z)$. The cubic rotational group $SO(3, Z)$ which is also known as the octahedral group consists of 24 rotations about the x , y and z axes. Since a finite rotation can be obtained by a set of infinitesimal rotations about an axis, the rotation operator $R_{\hat{n}}(\phi)$ of the $SO(3)$ also defines elements of the $SO(3, Z)$ group for a rotation by $\phi = m\pi/2$ about the n axis, where m is integer and n denotes the axes. Therefore, the angular momentum operators L_x , L_y and L_z in the $SO(3, Z)$ group are defined by

$$R_{\hat{n}}(\phi) = \exp(-iL_{\hat{n}}\phi) \quad (3.53)$$

It is clear that the eigenvalues of $L_{\hat{n}}$ are integers modulo 4.

The $2\ell + 1$ elements of angular momentum transform according to the irreducible representations of the $SO(3)$ group. Under the $SO(3, Z)$ group these representations are reducible in most cases and they break up into the five irreducible representations denoted by A_1 , T_1 , E , T_2 and A_2 . Examples for the decompositions of the orbital angular momentum eigenstates $\ell \leq 6$ into the irreducible representation of the $SO(3, Z)$ group are given in Table 3.1 [101]

3.5.2 Lüscher's finite-volume method

Lüscher's method [122, 124] is a well-known tool used to determine elastic phase shifts for two-body scattering from the volume dependence of two-body scattering states in a periodic cubic box. The method has been extended to higher partial waves, two-body systems in moving

Table 3.1 Decomposition of the $SO(3)$ into the irreducible representations of the $SO(3, Z)$ for $\ell \leq 6$.

$SO(3)$	$SO(3, Z)$
$\ell = 0$	A_1
$\ell = 1$	T_1
$\ell = 2$	$E \oplus T_2$
$\ell = 3$	$T_1 \oplus T_2 \oplus A_2$
$\ell = 4$	$A_1 \oplus T_1 \oplus E \oplus T_2$
$\ell = 5$	$T_1 \oplus T_1 \oplus E \oplus T_2$
$\ell = 6$	$A_1 \oplus T_1 \oplus E \oplus T_2 \oplus T_2 \oplus A_2$

frames, multi-channel scattering cases, and scattering of particles with spin [152, 125, 71, 119, 30, 32, 33, 31]. Lüscher's framework has also been successfully applied to the determination of resonance parameters [15], and recently this technique has been applied to moving frame calculations [51, 89]. See Ref. [16, 130, 50, 120, 52] for further studies on the extraction of resonance properties at finite volume. We note also recent work on improving lattice interactions in effective field theories using Lüscher's method [55].

In the following we summarize how Lüscher's method relates the s -wave scattering phase shift to two-body energy levels in a periodic cubic box. Later we come back to this discussion for higher angular momentum in Section 6.7.1.

We consider a two-body system in a periodic box of length L . The relation between the s -wave scattering phase shift and the two-particle energy levels in the center of mass frame is defined by

$$p \cot \delta_0(p) = \frac{2}{\sqrt{\pi L}} \mathcal{Z}_{0,0}(1; \eta) \quad (3.54)$$

where

$$\eta = \left(\frac{Lp}{2\pi} \right)^2, \quad (3.55)$$

and $\mathcal{Z}_{0,0}(1; \eta)$ is the three-dimensional zeta function,

$$\mathcal{Z}_{0,0}(1; \eta) = \frac{1}{\sqrt{4\pi}} \lim_{\Lambda \rightarrow \infty} \left[\sum_{\vec{n}} \frac{\theta(\Lambda^2 - \vec{n}^2)}{|\vec{n}|^2 - \eta} - 4\pi\Lambda \right]. \quad (3.56)$$

Alternatively, we can evaluate the zeta function using exponentially-accelerated expression [125]

$$\begin{aligned} \mathcal{Z}_{0,0}(1; \eta) = \pi e^\eta (2\eta - 1) + \frac{e^\eta}{2\sqrt{\pi}} \sum_{\vec{n}} \frac{e^{-|\vec{n}|^2}}{|\vec{n}|^2 - \eta} \\ - \frac{\pi}{2} \int_0^1 d\lambda \frac{e^{\lambda\eta}}{\lambda^{3/2}} \left(4\lambda^2 \eta^2 - \sum_{\vec{n}} e^{-\pi^2 |\vec{n}|^2 / \lambda} \right). \end{aligned} \quad (3.57)$$

3.5.3 Spherical wall method

While Lüscher's method is very powerful at low energies, the method is limited to calculations of scattering phase shifts below the inelastic threshold. Also, the phase shifts obtained using Lüscher's method depend crucially on an accurate calculation and analysis of finite-volume energy levels. Furthermore, since the eigenstates of the angular momentum for $\ell > 1$ decompose into the irreducible representations of the $\text{SO}(3, Z)$, there is no one-to-one correspondence between the finite-volume energy spectrum and the phase shifts [125]. Therefore, the scattering phase shift calculations become more and more difficult at higher angular momentum.

Borasoy et al. [23] proposed how to compute phase shifts for non-relativistic fundamental particles on the lattice without encountering some of the difficulties mentioned above. This method uses a spherical boundary condition on the lattice. A hard wall boundary of radius R_{wall}

is imposed on the relative separation of the two particles which removes the periodic lattice effects between particles.

For two particles interacting via a finite-range R potential, the radial part of the solution at values $r > R$ is described by Eq. (2.40) which vanishes at $r = R_{\text{wall}}$,

$$\cot \delta_\ell(p) S_\ell(pR_{\text{wall}}) + C_\ell(pR_{\text{wall}}) = 0. \quad (3.58)$$

Here p is the relative momentum of the particles, and it can be determined from the energy $E = p^2/2\mu$ with the reduced mass μ . Therefore, the scattering phase shifts can be computed by the following expression,

$$\cot \delta_\ell(p) = \cot^{-1} \left[-\frac{C_\ell(pR_{\text{wall}})}{S_\ell(pR_{\text{wall}})} \right]. \quad (3.59)$$

See Ref. [23, 118] for the detailed discussion on the topic and for the case of partial-wave mixing.

3.6 Numerical methods

3.6.1 Monte Carlo methods

In the preceding sections we have derived two elegant approaches which describe evolutions of particles between two space-time points in quantum systems. In principle numerical solutions for Eqs. (6.10) or (3.40) are not impossible, but it is computationally very expensive, perhaps not practical, due to the multi-dimensional integral in the PI formula and massive matrix operations in the operator formalism. In the presence of such difficulties Monte Carlo methods are the most powerful and commonly used techniques to approximate physical observables.

Monte Carlo techniques are based on the idea of simulating particle configurations by using random numbers as dynamics of the method. The fact that makes Monte Carlo techniques very advantageous is that among all states of the physical system only a small fraction are chosen at random according to some weighting function $P(c)$ in order to estimate mean values of physical quantities. Suppose \mathcal{O} be an observable that we want to estimate from Monte Carlo simulations, then the approximated expectation value (the estimator) of \mathcal{O} is the average over some subset states M of the complete states of the system³,

$$\langle \mathcal{O} \rangle_M = \frac{\sum_{i=1}^M \mathcal{O}(c_i) P(c_i)}{\sum_{i=1}^M P(c_i)}, \quad (3.60)$$

where $\mathcal{O}(c_i)$ is the value of the observable for the configuration c_i . The neglected subset states introduce some statistical errors in Monte Carlo simulations which are suppressed by the size of the sample.

3.6.2 Importance sampling

The chosen subset states in Eq. (3.60) determines the accuracy of the estimator and the performance of Monte Carlo simulations. One powerful technique that improves the accuracy of the simulations is *importance sampling*.

Importance sampling is implemented by selecting states with the probability function $P(c)$ in Eq. (3.60). Then Eq. (3.60) takes the following simpler form⁴

$$\langle \mathcal{O} \rangle_M = \frac{1}{M} \sum_{i=1}^M \mathcal{O}(c_i), \quad (3.61)$$

³The path integrals in Euclidean time are computed using a larger samples weighted by the exponential Boltzmann factor, $P(c) = e^{-\beta E(c)}$.

⁴The estimator is simply the average of the selected configurations.

and the statistical error is determined from the variance of the estimator by

$$\sigma = \sqrt{\frac{\sum_{i=0}^N [\mathcal{O}(c_i) - \langle \mathcal{O} \rangle_N]^2}{N-1}}. \quad (3.62)$$

This expression indicates that the statistical error can be easily kept under control by the size of the sample used in simulations, and the estimator can be made as accurate as desired by increasing the number of samples.

3.6.3 Markov process

Importance sampling has the key role of reducing the variance. However, if we randomly generate states, then most of them would be rejected and the computation time would be mostly wasted in such simulations. In order to make computations more efficient, we need a technique that generates some random set of states according to the distribution $P(c)$. This is done using a *Markov process*, which we now explain.

Suppose the probability distribution is time dependent and at time t the system is in a state A with probability $P(c_A, t)$. Let $\Omega(A \rightarrow B)$ be the probability that generates a state B at a later time $t + \Delta t$, then the evolution of $P(c_A, t)$ is

$$P(c_A, t) - P(c_A, t + \Delta t) = \sum_{B \neq A} [P(c_B, t) \Omega(B \rightarrow A) - P(c_A, t) \Omega(A \rightarrow B)], \quad (3.63)$$

where $\Omega(B \rightarrow A)$ is the transition probability for selecting the state A from the state B . The most important features of the transition probability for a Markov process are that;

- it is independent of time,
- it does not depend on any prior state that the system in before the state B ,

- $\Omega(A \rightarrow B) \geq 0$,
- $\sum_B \Omega(A \rightarrow B) = 1$.

It should be stressed that every state in a simulation must be accessible despite the fact that the transition probability from one particular state to another could be zero. This requires a Markov process to reach any state of the system from any other state, and it is known as *ergodicity*.

After the simulation runs for many steps, the system comes to an equilibrium,

$$\lim_{t \rightarrow \infty} P(c, t) \simeq P(c), \quad (3.64)$$

and the Markov process eventually generates successive states with the probability $P(c)$. If we repeat this Markov process in the simulation to generate successive states, we construct a *Markov chain* which is a set of states each of which is selected with the probability $P(c)$.

A sufficient condition which ensures that in equilibrium all states are generated according to the probability distribution $P(c)$ is the condition of *detailed balance*. The detailed balance requires that each term in the sum in Eq. (3.63) must be zero⁵. This will then satisfy Eq. 3.64,

$$P(c_B, t) \Omega(B \rightarrow A) = P(c_A, t) \Omega(A \rightarrow B). \quad (3.65)$$

This condition also ensures that the transition rate into any state is equal to the transition rate out of the same state.

⁵See Ref.[135] for rigorous proofs and detailed discussions.

3.6.4 Metropolis algorithm

The detailed balance equation (3.65) imposes a constraint on the transition probability from a state A to another state B by

$$\frac{\Omega(A \rightarrow B)}{\Omega(B \rightarrow A)} = \frac{P(c_B, t)}{P(c_A, t)} = e^{-\beta[E(c_B) - E(c_A)]}. \quad (3.66)$$

where the equilibrium distribution is chosen to be the Boltzmann distribution, $P(c) = P_0 e^{-\beta E(c)}$. Therefore, the states of the desired Markov chain are distributed according to the probability distribution $P_0 e^{-\beta E(c)}$. The most popular method for generating such successive states by respecting the detailed balance condition is the Metropolis algorithm [132]. In the following we give a simple recipe for the Metropolis algorithm.

Step 1: Initially start with an arbitrarily configuration C_i .

Step 2: Generate a proposed configuration C_p from the configuration C_i .

Step 3: Select a random number $r \in [0, 1)$.

Step 4: Accept the proposed configuration if $r < e^{-\beta[E(C_p) - E(C_i)]}$ and set $C_i = C_p$. Otherwise leave C_i the same.

Step 5: Repeat **Step 2-4**.

If the proposed configuration has a lower energy, $E(C_p) - E(C_i) \leq 0$, then the Metropolis algorithm always accept that configuration. If a configuration with higher energy is proposed, then it is only accepted with some probability given in **Step 4**.

3.6.5 Sign problem

Before ending this chapter we would like to discuss the sign problem that Monte Carlo methods suffer from simulating fermions. The main difficulty of simulations with fermions is the sign cancellation due to the identical particle permutations. When we perform calculations by sampling configurations, the fluctuation in the signs associated with Fermi-Dirac statistics results in significant cancellations. In order for rigorous expression let us consider the calculation of the expectation value of a physical observable \mathcal{O} ,

$$\langle \mathcal{O} \rangle = \frac{\sum_c s(c) P(c) \mathcal{O}(c)}{\sum_c s(c) P(c)} \equiv \frac{\langle s(c) \mathcal{O} \rangle}{\langle s(c) \rangle}, \quad (3.67)$$

where c is the number of configurations, $s(c) = \pm 1$ is the sign, and $P(c)$ is the magnitude of the weight. Since the average sign appears as the denominator in Eq. (3.67), it is crucial that the cancellation is tolerable. The average sign over c configurations is

$$\langle s(c) \rangle = \frac{\sum_c s(c) P(c)}{\sum_c P(c)} = \exp(-t \Delta E), \quad (3.68)$$

where $\Delta E = E_{phy} - E_{bos}$ is the difference between the physical ground state energy (E_{phy}) and the ground state energy (E_{bos}) due to the bosonic ensemble. Since $\Delta E > 0$ and scales with the system size, the average sign is exponentially small in the size of the system which makes the simulations exponentially difficult for large systems.

Neutron-proton scattering

4.1 Introduction

Chiral effective field theory describes the low-energy interactions of protons and neutrons. If one neglects electromagnetic effects, the long range behavior of the nuclear interactions is determined by pion exchange processes. See Ref. [166, 14, 58, 59] for reviews on chiral effective field theory. But there are also systems of interest where momenta smaller than the pion mass are relevant. In such cases it is more economical to use pionless effective field theory with only local contact interactions involving the nucleons. The pionless formulation is theoretically elegant since the theory at leading order is renormalizable and the momentum cutoff scale can be arbitrarily large [167, 11, 12, 13, 38, 145, 96]. This allows an elegant connection with the universal low-energy physics of fermions at large scattering length and other systems such as ultracold atoms [29, 88].

For local contact interactions the range of the interactions are set by the momentum cutoff scale for the effective theory. There are rigorous constraints for strictly finite-range interactions set by causality and unitarity. Some violations of unitarity can relax these constraints if one

works at finite order in perturbation theory or includes unphysical propagating modes with negative norm. However at some point one must accurately reproduce the underlying unitary quantum system by going to sufficiently high order in perturbation theory or decoupling the effects of propagating unphysical modes.

The time evolution of any quantum mechanical system obeys causality and unitarity. Causality requires that the cause of an event must occur before any resulting consequences are produced, and unitarity requires that the sum of all outcome probabilities equals one. In the case of non-relativistic scattering, these constraints mean that the outgoing wave may depart only after the incoming wave reaches the scattering object and must preserve the normalization of the incoming wave. In this chapter we discuss the constraints of causality and unitarity for finite range interactions. Specifically we consider neutron-proton scattering in all spin channels up to $j = 3$.

The constraints of causality and unitarity for two-body scattering with finite-range interactions were first investigated by Wigner [174]. The time delay between an incoming wave packet and the scattered outgoing wave packet is equal to the energy derivative of the elastic phase shift,

$$\Delta t = 2 \frac{d\delta}{dE}. \quad (4.1)$$

If $d\delta/dE$ is negative, the outgoing wave is produced earlier than that for the non-interacting system. However the incoming wave must first arrive in the interacting region before the outgoing wave can be produced. For each partial wave, ℓ , this puts an upper bound on the effective range parameter, r_ℓ , in the effective range expansion,

$$p^{2\ell+1} \cot \delta_\ell(p) = -\frac{1}{a_\ell} + \frac{1}{2} r_\ell p^2 + O(p^4). \quad (4.2)$$

We introduce the effective range expansion in Eq. (2.36). In this chapter we truncate the series

at p^2 .

Phillips and Cohen [142] derived the causality bound for the s -wave effective range parameter for finite-range interactions in three dimensions. Constraints on nucleon-nucleon scattering and the chiral two-pion exchange potential was considered in Ref. [140], and correlations between the scattering length and effective range have been explored for one-boson exchange potentials [36]. Same authors studied the relationship between the scattering length and effective range for the van der Waals interaction [35, 151]

In Refs. [94, 95] the causality and unitarity bounds for finite-range interactions were extended to an arbitrary number of space-time dimensions or value of angular momentum. A complementary discussion based upon conformal symmetry and scaling dimensions can be found in Ref. [137]. Also the interactions with attractive and repulsive Coulomb tails were first considered in Ref. [107].

Let R be the range of the interaction. For the case $d = 3$, it was found that the effective range parameter must satisfy the upper bound [94, 95]

$$r_\ell \leq b_\ell(r) = -\frac{2\Gamma(\ell - \frac{1}{2})\Gamma(\ell + \frac{1}{2})}{\pi} \left(\frac{r}{2}\right)^{-2\ell+1} - \frac{4}{\ell + \frac{1}{2}} \frac{1}{a_\ell} \left(\frac{r}{2}\right)^2 + \frac{2\pi}{\Gamma(\ell + \frac{3}{2})\Gamma(\ell + \frac{5}{2})} \frac{1}{a_\ell^2} \left(\frac{r}{2}\right)^{2\ell+3}, \quad (4.3)$$

for any $r \geq R$. This inequality can be used to determine a length scale, R^b , which we call the causal range,

$$r_\ell = b_\ell(R^b). \quad (4.4)$$

The physical meaning of R^b is that any set of interactions with strictly finite range that reproduces the physical scattering data must have a range greater than or equal to R^b .

In this chapter we extend the causality bound to the case of two coupled partial-wave

channels. For applications to nucleon-nucleon scattering the relevant coupled channels are 3S_1 - 3D_1 , 3P_2 - 3F_2 , 3D_3 - 3G_3 , etc. As we will show, there is some modification of the effective range bound in Eq. (4.3) due to mixing. For total spin j we show that the lower partial-wave channel $\ell = j - 1$ satisfies the new causality bound,

$$r_{j-1} \leq b_{j-1}(r) - 2q_0^2 \frac{\Gamma(j + \frac{1}{2})\Gamma(j + \frac{3}{2})}{\pi} \left(\frac{r}{2}\right)^{-2j-1}, \quad (4.5)$$

where q_0 is the first term in the expansion of the mixing angle ε_j in the Blatt-Biedenharn eigenphase convention [20],

$$\tan \varepsilon_j(p) = q_0 p^2 + q_1 p^4 + O(p^6). \quad (4.6)$$

We note that the last term in Eq. (4.5) is negative semi-definite and diverges as $r \rightarrow 0$. From this observation we make the general statement that non-vanishing partial-wave mixing is inconsistent with zero-range interactions. We will explore in detail the consequences of this result as it applies to nuclear effective field theory.

We also derive a new causality bound associated with the mixing angle itself. Using the Cauchy-Schwarz inequality we derive a bound for the parameter q_1 in the expansion Eq. (4.6). This leads to another minimum interaction length scale, which we call the Cauchy-Schwarz range, $R^{\text{C-S}}$. We use the new causality bounds to determine the minimum causal and Cauchy-Schwarz ranges for each ${}^{2s+1}\ell_j$ channel in neutron-proton scattering up to $j = 3$. Since the long range behavior of the nuclear interactions is determined by pion exchange processes, one expects $R^b \sim R^{\text{C-S}} \sim m_\pi^{-1} = 1.5$ fm. However in some higher partial-wave channels we find that these length scales are as large as 5 fm. We show these large ranges are generated by the one-pion exchange tail. Using a potential model we show that the causal range and Cauchy-Schwarz

range are both significantly reduced when the one-pion exchange tail is chopped off at distances beyond 5 fm. We discuss the impact of this finding on the choice of momentum cutoff scales in effective field theory.

In the limit of isospin symmetry our analysis of the isospin triplet channels can also be applied to neutron-neutron scattering and therefore has relevance to dilute neutron matter. The physics of dilute neutron matter is important for describing the crust of neutron stars as well as connections to the universal physics of fermions near the unitarity limit. Our analysis of the causality and unitarity bounds show that there are constraints on the universal character of neutron-neutron interactions in channels with partial-wave mixing as well as higher uncoupled partial-wave channels. In other words some low-energy phenomenology cannot be cleanly separated from microscopic details such the range of the interaction. Reviews of the theory of ultracold Fermi gases close to the unitarity limit and their numerical simulations are given in Ref. [88, 118]. A general overview of universality at large scattering length can be found in Ref. [29]. See Ref. [104, 147] for reviews of recent cold atom experiments at unitarity.

4.2 Uncoupled Channels

We analyze in this section the channels with only one partial wave, ℓ . We summarize the results obtained Section 2.5 [cf. in Ref. [95]]. For simplicity, we will assume throughout the calculations that the interaction has finite range R , and we use units where $\hbar = 1$. For the two-body system the rescaled radial wave function $U_\ell^{(p)}(r)$ satisfies the radial Schrödinger equation,

$$\left[-\frac{d^2}{dr^2} + \frac{\ell(\ell+1)}{r^2} - p^2 \right] U_\ell^{(p)}(r) + 2\mu \int_0^R W(r, r') U_\ell^{(p)}(r') dr' = 0. \quad (4.7)$$

We write $W(r, r')$ for the non-local interaction potential as a real symmetric integral operator. As we discuss in Section 2.3 we assume that the potential has finite range R which requires that $W(r, r') = 0$ for $r > R$ or $r' > R$.

In Eq. (2.68) taking the limit $p \rightarrow 0$, we obtain that for any $r > R$ the effective range satisfies the following relation,

$$r_\ell = b_\ell(r) - 2 \int_0^r \left[U_\ell^{(0)}(r') \right]^2 dr', \quad (4.8)$$

where $b_\ell(r)$ is

$$b_\ell(r) = \frac{1}{a_\ell^2} \frac{2\pi}{\Gamma(\ell + \frac{3}{2}) \Gamma(\ell + \frac{5}{2})} \left(\frac{r}{2}\right)^{2\ell+3} - \frac{1}{a_\ell} \frac{4}{\ell + \frac{1}{2}} \left(\frac{r}{2}\right)^2 - \frac{2\Gamma(\ell - \frac{1}{2}) \Gamma(\ell + \frac{1}{2})}{\pi} \left(\frac{r}{2}\right)^{-2\ell+1}. \quad (4.9)$$

Since the wave function is real and the integral term in Eq. (4.8) is positive semi-definite, this equation puts an upper bound on the effective range, $r_\ell \leq b_\ell(r)$. This relation and causality bound are analyzed in Ref. [95] for arbitrary dimension or angular momentum ℓ .

4.3 Coupled Channels

In this section we derive the general wave functions for spin-triplet scattering with mixing between orbital angular momentum $\ell = j - 1$ and $\ell = j + 1$. The coupled-channel wave functions satisfy the following coupled radial Schrödinger equations,

$$\left[-\frac{d^2}{dr^2} - p^2 + \frac{j(j-1)}{r^2} \right] U_{j-1}^{(p)}(r) + 2\mu \int_0^R [W_{11}(r, r') U_{j-1}^{(p)}(r') + W_{12}(r, r') V_{j+1}^{(p)}(r')] dr = 0, \quad (4.10)$$

$$\left[-\frac{d^2}{dr^2} - p^2 + \frac{(j+1)(j+2)}{r^2} \right] V_{j+1}^{(p)}(r) + 2\mu \int_0^R [W_{21}(r, r') U_{j-1}^{(p)}(r') + W_{22}(r, r') V_{j+1}^{(p)}(r')] dr' = 0. \quad (4.11)$$

Here the non-local interaction potentials are represented by a real symmetric 2×2 matrix $W(r, r')$,

$$W(r, r') = \begin{pmatrix} W_{11}(r, r') & W_{12}(r, r') \\ W_{12}(r, r') & W_{22}(r, r') \end{pmatrix}. \quad (4.12)$$

In Eq. (4.10)-Eq. (4.11) the $U_{j-1}^{(p)}(r)$ corresponds with the spin-triplet $\ell = j - 1$ channel and the $V_{j+1}^{(p)}(r)$ is for the spin-triplet $\ell = j + 1$. These wave functions are the rescaled form of the radial wave functions. In the non-interacting region $r \geq R$ the coupled radial Schrödinger equations reduce to the free radial Schrödinger equations

$$\left[-\frac{d^2}{dr^2} - p^2 + \frac{j(j-1)}{r^2} \right] U_{j-1}^{(p)}(r) = 0, \quad (4.13)$$

$$\left[-\frac{d^2}{dr^2} - p^2 + \frac{(j+1)(j+2)}{r^2} \right] V_{j+1}^{(p)}(r) = 0. \quad (4.14)$$

The solutions of these differential equations are the Riccati-Bessel functions,

$$U_{j-1}^{(p)}(r) = A_1 S_{j-1}(pr) + B_1 C_{j-1}(pr), \quad (4.15)$$

$$V_{j+1}^{(p)}(r) = A_2 S_{j+1}(pr) + B_2 C_{j+1}(pr). \quad (4.16)$$

where $A_{1,2}$ and $B_{1,2}$ are amplitudes associated with incoming and outgoing waves, respectively. More details regarding the Riccati-Bessel functions are given in Appendix A.1. The relation

between incoming and outgoing wave amplitudes is

$$B = KA, \quad (4.17)$$

K is the reaction matrix and is defined in terms of the unitary scattering matrix S by Eq. (2.20). Therefore, the Eq. (4.17) is written as

$$\tilde{B} = S\tilde{A}, \quad (4.18)$$

where $\tilde{A}_{1,2}$ and $\tilde{B}_{1,2}$ are rescaled amplitudes associated with incoming and outgoing waves. For two coupled channels the 2×2 scattering matrix can also be made symmetric. It is possible to write several different 2×2 S -matrices which satisfy the unitarity and symmetry properties. In the literature, there are two conventionally used 2×2 S -matrices [160, 20]. In this study we adopt the ‘‘eigenphase’’ parameterizations of Blatt and Biedernharn [20], and the relations between the eigenphase and nuclear bar [160] parameterizations are shown in Appendix C.1.

The S -matrix can be diagonalized by an orthogonal matrix U

$$S_d = USU^{-1} = \begin{pmatrix} e^{2i\delta_\alpha} & 0 \\ 0 & e^{2i\delta_\beta} \end{pmatrix}, \quad (4.19)$$

that contains one real parameter ε ,

$$U = \begin{pmatrix} \cos \varepsilon & \sin \varepsilon \\ -\sin \varepsilon & \cos \varepsilon \end{pmatrix}. \quad (4.20)$$

$\delta_\alpha(p)$ and $\delta_\beta(p)$ are the two phase shifts, and $\varepsilon(p)$ is the mixing angle. The S -matrix explicitly

is

$$S = \begin{pmatrix} e^{2i\delta_\alpha} \cos^2 \varepsilon + e^{2i\delta_\beta} \sin^2 \varepsilon & \cos \varepsilon \sin \varepsilon (e^{2i\delta_\alpha} - e^{2i\delta_\beta}) \\ \cos \varepsilon \sin \varepsilon (e^{2i\delta_\alpha} - e^{2i\delta_\beta}) & e^{2i\delta_\alpha} \sin^2 \varepsilon + e^{2i\delta_\beta} \cos^2 \varepsilon \end{pmatrix}. \quad (4.21)$$

The eigenvalue equation $S |X\rangle = \lambda |X\rangle$ results in eigenvalues $\lambda_1 = e^{2i\delta_\alpha}$ and $\lambda_2 = e^{2i\delta_\beta}$, with corresponding eigenstates,

$$|X_1\rangle = \begin{pmatrix} \cos \varepsilon \\ \sin \varepsilon \end{pmatrix} \quad \text{and} \quad |X_2\rangle = \begin{pmatrix} -\sin \varepsilon \\ \cos \varepsilon \end{pmatrix}, \quad (4.22)$$

which satisfy the orthogonality condition

$$\langle X_1 | X_2 \rangle = 0. \quad (4.23)$$

We can write Eq. (4.18) as

$$\begin{pmatrix} \tilde{B}_{1\alpha} & \tilde{B}_{1\beta} \\ \tilde{B}_{2\alpha} & \tilde{B}_{2\beta} \end{pmatrix} = \begin{pmatrix} S_{11} & S_{12} \\ S_{12} & S_{22} \end{pmatrix} \begin{pmatrix} \tilde{A}_{1\alpha} & \tilde{A}_{1\beta} \\ \tilde{A}_{2\alpha} & \tilde{A}_{2\beta} \end{pmatrix}, \quad (4.24)$$

where the matrices \tilde{A} and \tilde{B} are

$$\tilde{A} = \begin{pmatrix} e^{-i\delta_\alpha} \cos \varepsilon & -e^{-i\delta_\beta} \sin \varepsilon \\ e^{-i\delta_\alpha} \sin \varepsilon & e^{-i\delta_\beta} \cos \varepsilon \end{pmatrix}, \quad (4.25)$$

$$\tilde{B} = \begin{pmatrix} e^{i\delta_\alpha} \cos \varepsilon & -e^{i\delta_\beta} \sin \varepsilon \\ e^{i\delta_\alpha} \sin \varepsilon & e^{i\delta_\beta} \cos \varepsilon \end{pmatrix}. \quad (4.26)$$

We now define some additional notation. We write all α -state phaseshifts $\delta_\alpha(p)$ as $\delta_{j-1}(p)$

and all β -state phaseshifts $\delta_\beta(p)$ as $\delta_{j+1}(p)$. The notation is appropriate since in the $p \rightarrow 0$ limit the α -state is purely $\ell = j - 1$ and the β -state is purely $\ell = j + 1$. We also drop the superscript p in the wave functions. We choose the normalization of the wave function to be well-behaved in the zero-energy limit. Using the relations

$$S_{j\pm 1}(pr) \xrightarrow{\text{as } p \rightarrow 0} \sqrt{\pi}(pr)^{j\pm 1+1} \frac{2^{-j\mp 1-1}}{\Gamma(j\pm 1 + 3/2)}, \quad (4.27)$$

$$C_{j\pm 1}(pr) \xrightarrow{\text{as } p \rightarrow 0} \frac{(pr)^{-j\mp 1}}{\sqrt{\pi}} 2^{j\pm 1} \Gamma(j\pm 1 + 1/2), \quad (4.28)$$

and removing an overall phase factor, we get wave functions of the form

$$U_\alpha(r) = \cos \varepsilon_j(p) p^{j-1} [\cot \delta_{j-1}(p) S_{j-1}(pr) + C_{j-1}(pr)], \quad (4.29)$$

$$V_\alpha(r) = \sin \varepsilon_j(p) p^{j-1} [\cot \delta_{j-1}(p) S_{j+1}(pr) + C_{j+1}(pr)], \quad (4.30)$$

$$U_\beta(r) = -\sin \varepsilon_j(p) p^{j+1} [\cot \delta_{j+1}(p) S_{j-1}(pr) + C_{j-1}(pr)], \quad (4.31)$$

$$V_\beta(r) = \cos \varepsilon_j(p) p^{j+1} [\cot \delta_{j+1}(p) S_{j+1}(pr) + C_{j+1}(pr)]. \quad (4.32)$$

For later convenience we define

$$s_\ell(p, r) = p^{-\ell-1} S_\ell(pr), \quad (4.33)$$

$$c_\ell(p, r) = p^\ell C_\ell(pr). \quad (4.34)$$

$s_\ell(p, r)$ and $c_\ell(p, r)$ are given in Appendix A.1. Plugging in these function into Eq. (4.29)-

Eq. (4.32) we obtain

$$U_\alpha(r) = \cos \varepsilon_j(p) [p^{2j-1} \cot \delta_{j-1}(p) s_{j-1}(p, r) + c_{j-1}(p, r)], \quad (4.35)$$

$$V_\alpha(r) = \sin \varepsilon_j(p) [p^{2j+1} \cot \delta_{j-1}(p) s_{j+1}(p, r) + p^{-2} c_{j+1}(p, r)], \quad (4.36)$$

$$U_\beta(r) = -\sin \varepsilon_j(p) [p^{2j+1} \cot \delta_{j+1}(p) s_{j-1}(p, r) + p^2 c_{j-1}(p, r)], \quad (4.37)$$

$$V_\beta(r) = \cos \varepsilon_j(p) [p^{2j+3} \cot \delta_{j+1}(p) s_{j+1}(p, r) + c_{j+1}(p, r)]. \quad (4.38)$$

The multi channel effective range expansion formula is given in Eq. (2.37), and here we truncate the expansion at p^2 and write the two-channel effective range expansion for the total spin angular momentum $s = 1$ in the following form,

$$\sum_{m', n'} \mathbf{p}_{mm'} [\mathbf{K}^{-1}]_{m'n'} \mathbf{p}_{n'n} = -\frac{1}{\mathbf{a}_{mn}} + \frac{1}{2} \mathbf{r}_{mn} p^2 + O(p^4), \quad (4.39)$$

where \mathbf{a}_{mn} is the scattering length matrix, \mathbf{r}_{mn} is the effective range matrix, and \mathbf{p}_{mn} is the diagonal momentum matrix $\text{diag}(p^{j-1/2}, p^{j+3/2})$. The two-channel effective range expansion in the Blatt and Biedernharn parameterization is

$$\sum_{m' m'' n' n''} \mathbf{p}_{mm'} U_{m' m''} [\mathbf{K}^{-1}]_{m'' n''} [U^{-1}]_{n'' n'} \mathbf{p}_{n' n} = -\frac{1}{a_{mn}} + \frac{1}{2} r_{mn} p^2 + \mathcal{O}(p^4) \quad (4.40)$$

where $a_{mn} = \text{diag}(a_{j-1}, a_{j+1})$, $r_{mn} = \text{diag}(r_{j-1}, r_{j+1})$, and we drop the indices the reaction and unitary matrices for the sake of simplicity. In addition we get an analytic expansion for the tangent mixing angle [19]

$$\tan \varepsilon_j(p) = q_0 p^2 + q_1 p^4 + \mathcal{O}(p^6) \quad (4.41)$$

with mixing parameters q_0 and q_1 . Now using Eq. (4.41) we obtain the following final forms of wave functions for $r \geq R$,

$$U_\alpha(r) = \frac{-1}{a_{j-1}} s_{0,j-1}(r) + c_{0,j-1}(r) + p^2 \left\{ \frac{1}{2} r_{j-1} s_{0,j-1}(r) - \frac{1}{a_{j-1}} s_{2,j-1}(r) + c_{2,j-1}(r) \right\} + \mathcal{O}(p^4), \quad (4.42)$$

$$V_\alpha(r) = q_0 c_{0,j+1}(r) + p^2 \left\{ q_1 c_{0,j+1}(r) + q_0 c_{2,j+1}(r) \right\} + \mathcal{O}(p^4), \quad (4.43)$$

$$U_\beta(r) = q_0 \frac{1}{a_{j+1}} s_{0,j-1}(r) + p^2 \left\{ q_0 \frac{1}{a_{j+1}} s_{2,j-1}(r) - q_0 \frac{r_{j+1}}{2} s_{0,j-1}(r) + q_1 \frac{1}{a_{j+1}} s_{0,j-1}(r) \right\} + \mathcal{O}(p^4), \quad (4.44)$$

$$V_\beta(r) = \frac{-1}{a_{j+1}} s_{0,j+1}(r) + c_{0,j+1}(r) + p^2 \left\{ \frac{1}{2} r_{j+1} s_{0,j+1}(r) - \frac{1}{a_{j+1}} s_{2,j+1}(r) + c_{2,j+1}(r) \right\} + \mathcal{O}(p^4). \quad (4.45)$$

As in the single channel case, the tool that we use to derive the causality bound is the Wronskian identity. Through the derivation we recall assumption on the potential in Section 2.3. We assume that the potential is not singular at the origin and regular solutions of the Schrödinger equations $U(r)$ and $V(r)$ for two different values of momenta, p_a and p_b , satisfy

$$\lim_{\rho \rightarrow 0^+} U_b(\rho) U_a'(\rho) = \lim_{\rho \rightarrow 0^+} U_a(\rho) U_b'(\rho) = 0, \quad (4.46)$$

$$\lim_{\rho \rightarrow 0^+} V_b(\rho) V_a'(\rho) = \lim_{\rho \rightarrow 0^+} V_a(\rho) V_b'(\rho) = 0. \quad (4.47)$$

Following the procedure given in Section. 2.5.3, for $\gamma = \alpha, \beta$ states we obtain

$$\begin{aligned} (p_a^2 - p_b^2) \int_0^r [U_{a\gamma}(r')U_{b\gamma}(r') + V_{a\gamma}(r')V_{b\gamma}(r')] dr' \\ = W[U_{a\gamma}(r), U_{b\gamma}(r)] + W[V_{a\gamma}(r), V_{b\gamma}(r)], \end{aligned} \quad (4.48)$$

and for the combination of α and β states, we get

$$\begin{aligned} (p_a^2 - p_b^2) \int_0^r [U_{a\alpha}(r')U_{b\beta}(r') + V_{a\alpha}(r')V_{b\beta}(r') + U_{b\alpha}(r')U_{a\beta}(r') + V_{b\alpha}(r')V_{a\beta}(r')] dr' \\ = W[U_{a\alpha}(r), U_{b\beta}(r)] + W[U_{a\beta}(r), U_{b\alpha}(r)] + W[V_{a\alpha}(r), V_{b\beta}(r)] + W[V_{a\beta}(r), V_{b\alpha}(r)]. \end{aligned} \quad (4.49)$$

The Wronskian of the α -state wave functions and the β -state wave functions for the non-interacting region $r \geq R$ are given in Appendix B.1.2.

In Eq. (4.48), we set $p_a = 0$ and take the limit $p = p_b \rightarrow 0$. In the region $r \geq R$ we obtain the following relations for the effective range parameters,

$$r_{j-1} = b_{j-1}(r) + 2q_0^2 W[c_2(r), c_0(r)]_{j+1} - 2 \int_0^r \left([U_\alpha^{(0)}(r')]^2 + [V_\alpha^{(0)}(r')]^2 \right) dr', \quad (4.50)$$

$$r_{j+1} = b_{j+1}(r) + 2q_0^2 \frac{1}{a_{j+1}^2} W[s_2(r), s_0(r)]_{j-1} - 2 \int_0^r \left([U_\beta^{(0)}(r')]^2 + [V_\beta^{(0)}(r')]^2 \right) dr'. \quad (4.51)$$

Here $b_{j\mp 1}$ are

$$\begin{aligned} b_{j\mp 1}(r) = \frac{2}{a_{j\mp 1}^2} W[s_2(r), s_0(r)]_{j\mp 1} + \frac{2}{a_{j\mp 1}} W[c_0(r), s_2(r)]_{j\mp 1} \\ + \frac{2}{a_{j\mp 1}} W[s_0(r), c_2(r)]_{j\mp 1} + 2W[c_2(r), c_0(r)]_{j\mp 1}, \end{aligned} \quad (4.52)$$

which reduce to the form

$$b_{j\mp 1}(r) = \frac{1}{a_{j\mp 1}^2} \frac{2\pi}{\Gamma(j\mp 1 + \frac{3}{2}) \Gamma(j\mp 1 + \frac{5}{2})} \left(\frac{r}{2}\right)^{2(j\mp 1)+3} - \frac{1}{a_{j\mp 1}} \frac{4}{j\mp 1 + \frac{1}{2}} \left(\frac{r}{2}\right)^2 - \frac{2\Gamma(j\mp 1 - \frac{1}{2}) \Gamma(j\mp 1 + \frac{1}{2})}{\pi} \left(\frac{r}{2}\right)^{-2(j\mp 1)+1}. \quad (4.53)$$

In Eq. (4.49), we set $p_a = 0$ and take the same limit, $p = p_b \rightarrow 0$. In the region $r \geq R$ we obtain

$$q_1 \frac{2}{a_{j+1}} = d_j(r) - 2 \int_0^r \left[U_\alpha^{(0)}(r') U_\beta^{(0)}(r') + V_\alpha^{(0)}(r') V_\beta^{(0)}(r') \right] dr'. \quad (4.54)$$

Here $d_j(r)$ is

$$d_j(r) = -q_0 \frac{2}{a_{j-1} a_{j+1}} W[s_2(r), s_0(r)]_{j-1} + 2q_0 W[c_2(r), c_0(r)]_{j+1} + q_0 \frac{2}{a_{j+1}} \left\{ W[c_2(r), s_0(r)]_{j-1} - W[c_2(r), s_0(r)]_{j+1} \right\}, \quad (4.55)$$

and this can be written as

$$d_j(r) = \frac{-q_0}{a_{j-1} a_{j+1}} \frac{2\pi}{\Gamma(\frac{1}{2} + j) \Gamma(\frac{3}{2} + j)} \left(\frac{r}{2}\right)^{2j+1} + \frac{q_0}{a_{j+1}} \frac{4}{(2j-1)(2j+3)} r^2 - 2q_0 \frac{\Gamma(j + \frac{1}{2}) \Gamma(j + \frac{3}{2})}{\pi} \left(\frac{r}{2}\right)^{-2j-1}. \quad (4.56)$$

All of equations derived here have been numerically checked using a simple potential model. The numerical calculations using delta-function shell potentials with partial-wave mixing have been performed, and details are given in Appendix. C.2.

4.4 Causality Bounds

The terms in the integrals in Eq. (4.50) and Eq. (4.51) are positive semi-definite since the wave functions are real. Therefore Eq. (4.50) and Eq. (4.51) place upper bounds for the effective range r_{j-1} and r_{j+1} respectively. As noted in the introduction, these upper bounds result from the causality and unitarity in the quantum scattering problem. Our results are extensions of single-channel results in Ref. [142] for the s -wave in three dimensions and in Ref. [94] for arbitrary angular momentum and arbitrary dimensions.

The causality bounds for the lower and higher partial-wave effective ranges are

$$r_{j-1} \leq b_{j-1}(r) - 2q_0^2 \frac{\Gamma(j + \frac{1}{2})\Gamma(j + \frac{3}{2})}{\pi} \left(\frac{r}{2}\right)^{-2j-1}, \quad (4.57)$$

$$r_{j+1} \leq b_{j+1}(r) + \frac{2q_0^2}{a_{j+1}^2} \frac{\pi}{\Gamma(j + \frac{1}{2})\Gamma(j + \frac{3}{2})} \left(\frac{r}{2}\right)^{2j+1}. \quad (4.58)$$

We note that the effective range bounds are modified due to partial-wave mixing. The causality upper bound for r_{j-1} is lowered by the negative term on the right hand side of Eq. (4.57), while the causality upper bound for the higher partial-wave is increased by the term on the right hand side of Eq. (4.58). When q_0 is nonzero and we take the limit of zero range interactions, Eq. (4.57) tells us that r_{j-1} is driven to negative infinity for any j . We conclude that the physics of partial-wave mixing requires a non-zero range for the interactions in order to comply with the constraints of causality and unitarity. In Ref. [94] a similar negative divergence in the effective range parameter was found for single-channel partial waves with $\ell > 0$. What is interesting here is that the negative divergence of the effective range occurs already in the 3S_1 channel due to partial-wave mixing.

We note that the integral terms in Eq. (4.50), Eq. (4.51) and Eq. (4.54) are closely related.

Analysis of these equations using the Cauchy-Schwarz inequality provides another useful relation for the coupled-channel wave functions. For real functions $f_1(r)$, $f_2(r)$, $g_1(r)$ and $g_2(r)$, the Cauchy-Schwarz inequality is

$$\left(\int [f_1(r) \ f_2(r)] \begin{bmatrix} f_1(r) \\ f_2(r) \end{bmatrix} dr \right) \left(\int [g_1(r) \ g_2(r)] \begin{bmatrix} g_1(r) \\ g_2(r) \end{bmatrix} dr \right) \geq \left| \int [f_1(r)g_1(r) + f_2(r)g_2(r)] dr \right|^2. \quad (4.59)$$

When we apply the inequality to our coupled wave functions, we get

$$f_{j-1}(r)g_{j+1}(r) \geq [h_j(r)]^2, \quad (4.60)$$

where

$$f_{j-1}(r) = b_{j-1}(r) - 2q_0^2 \frac{\Gamma(j + \frac{1}{2})\Gamma(j + \frac{3}{2})}{\pi} \left(\frac{r}{2}\right)^{-2j-1} - r_{j-1}, \quad (4.61)$$

$$g_{j+1}(r) = b_{j+1}(r) + \frac{2q_0^2}{a_{j+1}^2} \frac{\pi}{\Gamma(j + \frac{1}{2})\Gamma(j + \frac{3}{2})} \left(\frac{r}{2}\right)^{2j+1} - r_{j+1}, \quad (4.62)$$

and

$$h_j(r) = d_j(r) - q_1 \frac{2}{a_{j+1}}. \quad (4.63)$$

This inequality is used to define a Cauchy-Schwarz range, $R^{\text{C-S}}$, as the minimum r for each coupled channel where Eq. (4.57), Eq. (4.58) and Eq. (4.60) hold.

4.5 Neutron-Proton Scattering

We now apply our causality bounds to physical neutron-proton data. In this study, we use the low energy neutron-proton scattering data (0-350 MeV) from the NN data base by the Nijmegen

Group [161]. Tables 4.1- 4.3 show the low-energy threshold parameters in the eigenphase parameterization for the NijmII and the Reid93 potentials. These parameters are calculated using the results obtained in Ref. [165] for the low-energy threshold parameters of the nuclear bar parameterization and relations between eigenphase and nuclear bar parameterizations given in Appendix C.1. Using these numbers we analyze Eq. (4.50), Eq. (4.51) and Eq. (4.54), as well as causality bounds for the uncoupled channels.

Table 4.1 The eigenphase low energy parameters of uncoupled channels for neutron-proton scattering by the NijmII and the Reid93 interaction potentials.

Channel	a_ℓ [fm $^{2\ell+1}$] NijmII (Reid93)	r_ℓ [fm $^{-2\ell+1}$] NijmII (Reid93)
1S_0	-23.727 (-23.735)	2.670 (2.753)
1P_1	2.797 (2.736)	-6.399 (-6.606)
3P_0	-2.468 (-2.469)	3.914 (3.870)
3P_1	1.529 (1.530)	-8.580 (-8.556)
1D_2	-1.389 (-1.377)	14.87 (15.04)
3D_2	-7.405 (-7.411)	2.858 (2.851)
1F_3	8.383 (8.365)	-3.924 (-3.936)
3F_3	2.703 (2.686)	-9.932 (-9.994)

4.5.1 Uncoupled Channels

We start with channels of a single uncoupled partial wave. Since there is no mixing between different partial-waves, we evaluate Eq. (4.50) and Eq. (4.51) with zero mixing angle, and we obtain the following equation for the effective range

$$r_\ell = b_\ell(r) - 2 \int_0^r \left[U_\ell^{(0)}(r') \right]^2 dr', \quad (4.64)$$

Table 4.2 The eigenphase low energy parameters of coupled channels for neutron-proton scattering by the NijmII and the Reid93 interaction potentials.

Channel	a_ℓ [fm $^{2\ell+1}$] NijmII (Reid93)	r_ℓ [fm $^{-2\ell+1}$] NijmII (Reid93)
3S_1	5.418 (5.422)	1.7531 (1.7554)
3D_1	6.0043 (5.9539)	-3.523 (-3.566)
3P_2	-0.2844 (-0.2892)	-11.1465 (-10.7127)
3F_2	8.126 (7.882)	-5.640 (-5.821)
3D_3	-0.1449 (-0.177)	288.428 (198.528)
3G_3	648.813 (534.594)	-0.03306 (-0.0529)

Table 4.3 The eigenphase low energy mixing parameters of coupled channels for neutron-proton scattering by the NijmII and the Reid93 interaction potentials.

Mixing angle	q_0 [fm 2] NijmII (Reid93)	q_1 [fm 4] NijmII (Reid93)
ε_1	0.303987 (0.303394)	-2.00228 (-1.99129)
ε_2	-5.65752 (-5.5325)	65.8602 (64.2979)
ε_3	66.6632 (54.7062)	340.988 (94.9015)

where b_ℓ is given in Eq. (4.9). These solutions were derived by Hammer and Lee [95] for arbitrary dimension and angular momentum.

Here, we analyze the causality bound of the effective range for $\ell \leq 3$ using the scattering parameters in Table 4.1. In Figure 4.1, we plot $\frac{1}{2}[b_\ell(r) - r_\ell]$ for all of uncoupled channels with $\ell \leq 3$. The physical region corresponds with $\frac{1}{2}[b_\ell(r) - r_\ell] \geq 0$.

For s -wave scattering

$$b_0(r) = \frac{2}{3a_0^2}r^3 - \frac{2}{a_0}r^2 + 2r, \quad (4.65)$$

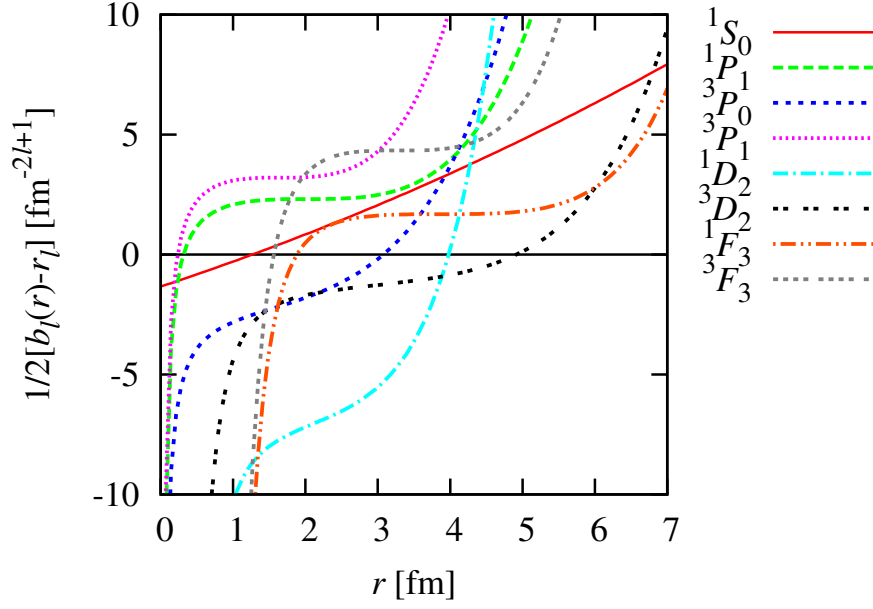


Figure 4.1 The plot of $[b_\ell(r) - r_\ell]/2$ as a function of r for neutron-proton scattering via the NijmII potential in the $^{2s+1}\ell_j$ channel.

for p -wave,

$$b_1(r) = \frac{2r^5}{45a_1^2} - \frac{2r^2}{3a_1} - \frac{2}{r}, \quad (4.66)$$

for d -wave,

$$b_2(r) = \frac{2}{1575a_2^2}r^7 - \frac{2}{5a_2}r^2 - \frac{6}{r^3}, \quad (4.67)$$

for f -wave,

$$b_3(r) = \frac{2r^9}{99225a_3^2} - \frac{2r^2}{7a_3} - \frac{90}{r^5}, \quad (4.68)$$

and for g -wave,

$$b_4(r) = \frac{2r^{11}}{9823275a_4^2} - \frac{2r^2}{9a_4} - \frac{3150}{r^7}. \quad (4.69)$$

4.5.2 Coupled Channels

We now analyze channels with coupled partial waves. We plot Eq. (4.61) and Eq. (4.62) for all coupled channels with $j \leq 3$. The physical region correspond both $f_{j-1}(r) \geq 0$ and $g_{j+1}(r) \geq 0$.

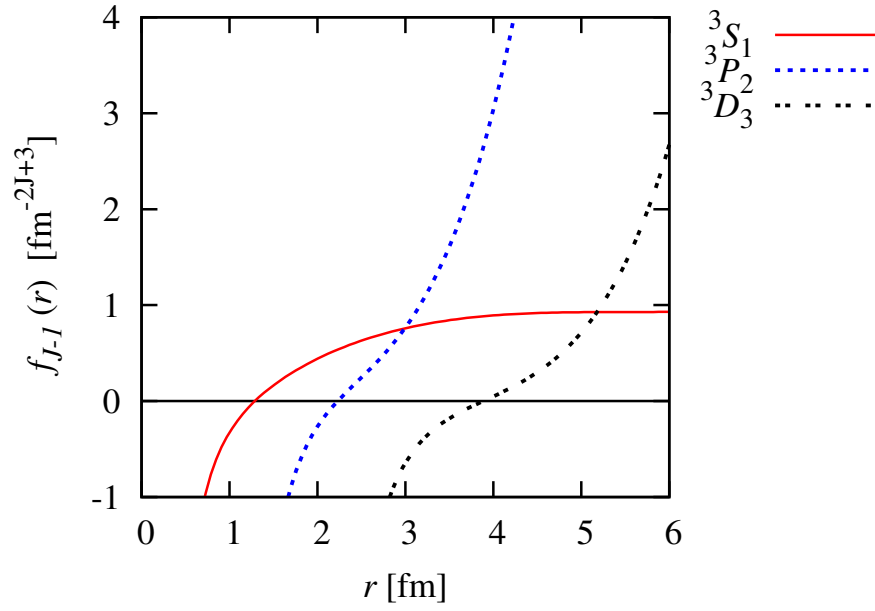


Figure 4.2 The plot of $f_{j-1}(r)$ as a function of r for neutron-proton scattering via the NijmII potential for $j \leq 3$. Here $f_1(r)$ is rescaled by a factor of 0.01 and $f_2(r)$ is rescaled by a factor of 10^{-4} .

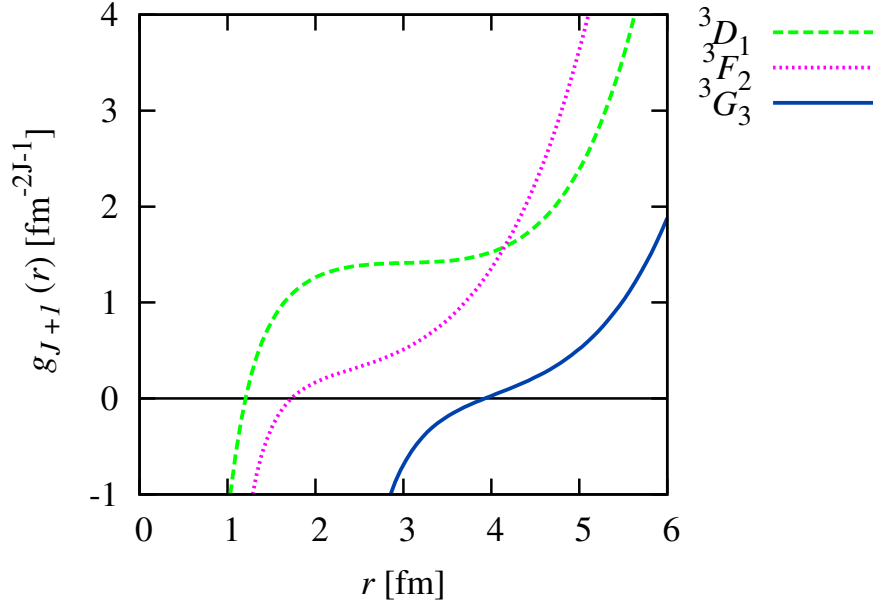


Figure 4.3 The plot of $g_{j+1}(r)$ as a function of r for neutron-proton scattering via the NijmII potential for $j \leq 3$. Here $g_3(r)$ is rescaled by a factor of 0.1.

4.5.2.1 3S_1 - 3D_1 Coupling.

We consider Eq. (4.50) - Eq. (4.55) for the 3S_1 - 3D_1 coupled channel. We evaluate the Wronskians for $j = 1$ and get

$$b_0(r) - q_0^2 \frac{6}{r^3} - r_0 = 2 \int_0^r \left([U_\alpha^{(0)}(r')]^2 + [V_\alpha^{(0)}(r')]^2 \right) dr', \quad (4.70)$$

$$b_2(r) + q_0^2 \frac{2r^3}{3a_2^2} - r_2 = 2 \int_0^r \left([U_\beta^{(0)}(r')]^2 + [V_\beta^{(0)}(r')]^2 \right) dr', \quad (4.71)$$

$$d_1(r) - q_1 \frac{2}{a_2} = 2 \int_0^r [U_{0\alpha}(r')U_{0\beta}(r') + V_{0\alpha}(r')V_{0\beta}(r')] dr'. \quad (4.72)$$

$b_0(r)$ and $b_2(r)$ are given in Eq. (4.65) and in Eq. (4.67), respectively, and $d_1(r)$ is

$$d_1(r) = -q_0 \frac{1}{a_0 a_2} \frac{2r^3}{3} + q_0 \frac{1}{a_2} \frac{4r^2}{5} - q_0 \frac{6}{r^3}. \quad (4.73)$$

Using the scattering parameters in Tables 4.2 - 4.3, we plot Eq. (4.70), Eq. (4.71) and Eq. (4.72) as functions of r . In Figure 4.4 we show the physical region where the causality

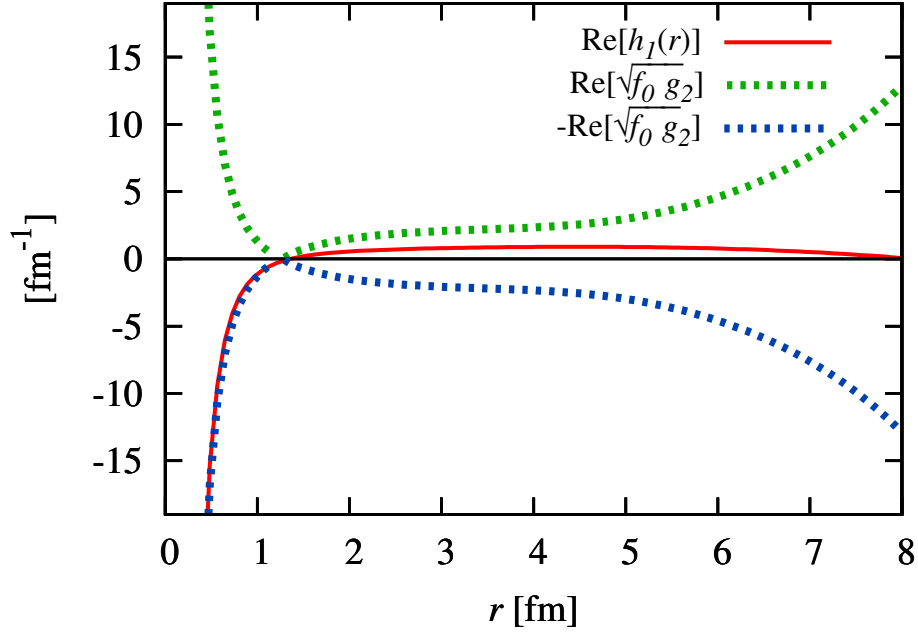


Figure 4.4 We plot $\text{Re}[\sqrt{f_0(r)g_2(r)}]$, $-\text{Re}[\sqrt{f_0(r)g_2(r)}]$, and $\text{Re}[h_1(r)]$ as functions of r for neutron-proton scattering in 3S_1 - 3D_1 coupled channel.

bounds $f_0(r) \geq 0$, $g_2(r) \geq 0$, and $f_0(r)g_2(r) \geq h_1^2(r)$, are satisfied. Here we have

$$f_0(r) = \frac{2}{3a_0^2} r^3 - \frac{2}{a_0} r^2 + 2r - q_0^2 \frac{6}{r^3} - r_0, \quad (4.74)$$

$$g_2(r) = \frac{2}{1575a_2^2}r^7 - \frac{2}{5a_2}r^2 - \frac{6}{r^3} + q_0^2 \frac{2r^3}{3a_2^2} - r_2, \quad (4.75)$$

$$h_1(r) = -q_0 \frac{1}{a_0a_2} \frac{2r^3}{3} + q_0 \frac{1}{a_2} \frac{4r^2}{5} - q_0 \frac{6}{r^3} - q_1 \frac{2}{a_2}. \quad (4.76)$$

4.5.2.2 ${}^3P_2 - {}^3F_2$ Coupling.

In the ${}^3P_2 - {}^3F_2$ coupled channel Eq. (4.50) - Eq. (4.55) take the following forms,

$$b_1(r) - q_0^2 \frac{90}{r^5} - r_1 = 2 \int_0^r \left([U_\alpha^{(0)}(r')]^2 + [V_\alpha^{(0)}(r')]^2 \right) dr', \quad (4.77)$$

$$b_3(r) + q_0^2 \frac{1}{a_3^2} \frac{2r^5}{45} - r_3 = 2 \int_0^r \left([U_\beta^{(0)}(r')]^2 + [V_\beta^{(0)}(r')]^2 \right) dr', \quad (4.78)$$

$$d_2(r) - q_1 \frac{2}{a_3} = 2 \int_0^r [U_{0\alpha}(r')U_{0\beta}(r') + V_{0\alpha}(r')V_{0\beta}(r')] dr'. \quad (4.79)$$

$b_1(r)$ and $b_3(r)$ are defined in Eq. (4.66) and Eq. (4.68), respectively, and $d_2(r)$ is

$$d_2(r) = -q_0 \frac{1}{a_1a_3} \frac{2r^5}{45} + q_0 \frac{1}{a_3} \frac{4r^2}{21} - q_0 \frac{90}{r^5}. \quad (4.80)$$

The causality bounds are $f_1(r) \geq 0$, $g_3(r) \geq 0$, and $f_1(r)g_3(r) \geq h_2^2(r)$, where

$$f_1(r) = \frac{2r^5}{45a_1^2} - \frac{2r^2}{3a_1} - \frac{2}{r} - q_0^2 \frac{90}{r^5} - r_1, \quad (4.81)$$

$$g_3(r) = \frac{2r^9}{99225a_3^2} - \frac{2r^2}{7a_3} - \frac{90}{r^5} + q_0^2 \frac{1}{a_3^2} \frac{2r^5}{45} - r_3, \quad (4.82)$$

$$h_2(r) = -q_0 \frac{1}{a_1a_3} \frac{2r^5}{45} + q_0 \frac{1}{a_3} \frac{4r^2}{21} - q_0 \frac{90}{r^5} - q_1 \frac{2}{a_3}. \quad (4.83)$$

In Figure 4.5 we show the physical region for the ${}^3P_2 - {}^3F_2$ coupled channel wave functions.

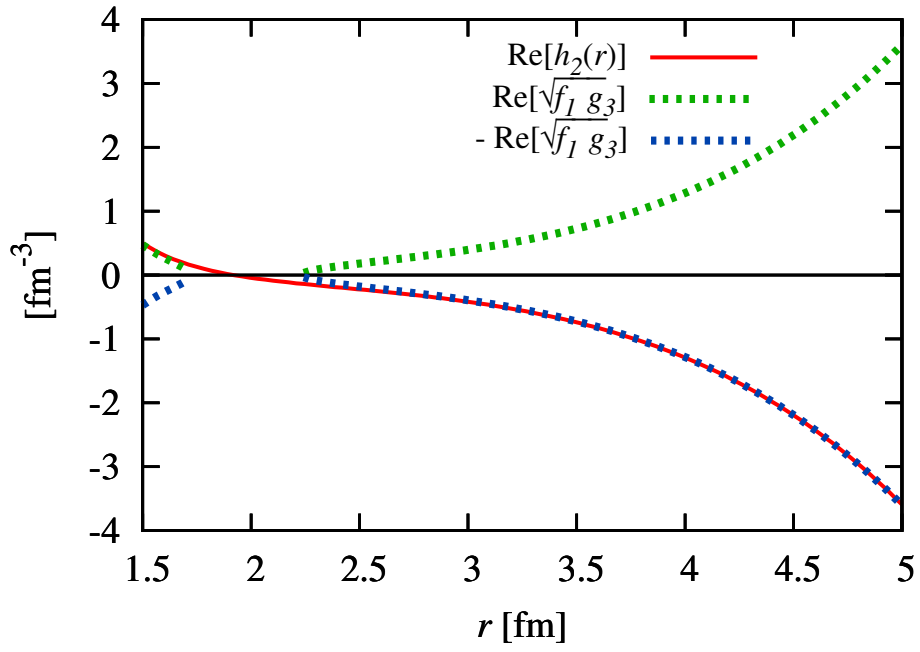


Figure 4.5 We plot $\text{Re}[\sqrt{f_1(r)g_3(r)}]$, $-\text{Re}[\sqrt{f_1(r)g_3(r)}]$, and $\text{Re}[h_2(r)]$ as functions of r for neutron-proton scattering in 3P_2 - 3F_2 coupled channel. The functions are rescaled by a factor of 0.01.

4.5.2.3 ${}^3D_3 - {}^3G_3$ Coupling.

For $j = 3$, the 3D_3 and 3G_3 channels are coupled. In this case Eq. (4.50)-Eq. (4.55) read

$$b_2(r) - q_0^2 \frac{3150}{r^7} - r_2 = 2 \int_0^r \left([U_\alpha^{(0)}(r')]^2 + [V_\alpha^{(0)}(r')]^2 \right) dr', \quad (4.84)$$

$$b_4(r) + \frac{q_0^2}{a_4^2} \frac{2r^7}{1575} - r_4 = 2 \int_0^r \left([U_\beta^{(0)}(r')]^2 + [V_\beta^{(0)}(r')]^2 \right) dr', \quad (4.85)$$

$$d_3(r) - q_1 \frac{2}{a_4} = 2 \int_0^r [U_{0\alpha}(r')U_{0\beta}(r') + V_{0\alpha}(r')V_{0\beta}(r')] dr'. \quad (4.86)$$

Here $d_3(r)$ is

$$d_3(r) = -\frac{q_0}{a_2 a_4} \frac{2r^7}{1575} + q_0 \frac{1}{a_4} \frac{4r^2}{45} - q_0 \frac{3150}{r^7}. \quad (4.87)$$

The causality bounds are again $f_2(r) \geq 0$, $g_4(r) \geq 0$, and $f_2(r)g_4(r) \geq h_3^2(r)$, where

$$f_2(r) = \frac{2r^7}{1575a_2^2} - \frac{2r^2}{5a_2} - \frac{6}{r^3} - q_0^2 \frac{3150}{r^7} - r_2, \quad (4.88)$$

$$g_4(r) = \frac{2r^{11}}{9823275a_4^2} - \frac{2r^2}{9a_4} - \frac{3150}{r^7} + \frac{q_0^2}{a_4^2} \frac{2r^7}{1575} - r_4, \quad (4.89)$$

$$h_3(r) = -\frac{q_0}{a_2 a_4} \frac{2r^7}{1575} + q_0 \frac{1}{a_4} \frac{4r^2}{45} - q_0 \frac{3150}{r^7} - q_1 \frac{2}{a_4}. \quad (4.90)$$

We show plots for the 3D_3 - 3G_3 channel in Figure 4.6.

4.6 Results and Discussion

In this section we present the results for the causal and Cauchy-Schwarz ranges, R^b , and R^{C-S} .

We use the NijmII scattering data for neutron-proton scattering presented above. In Table 4.4

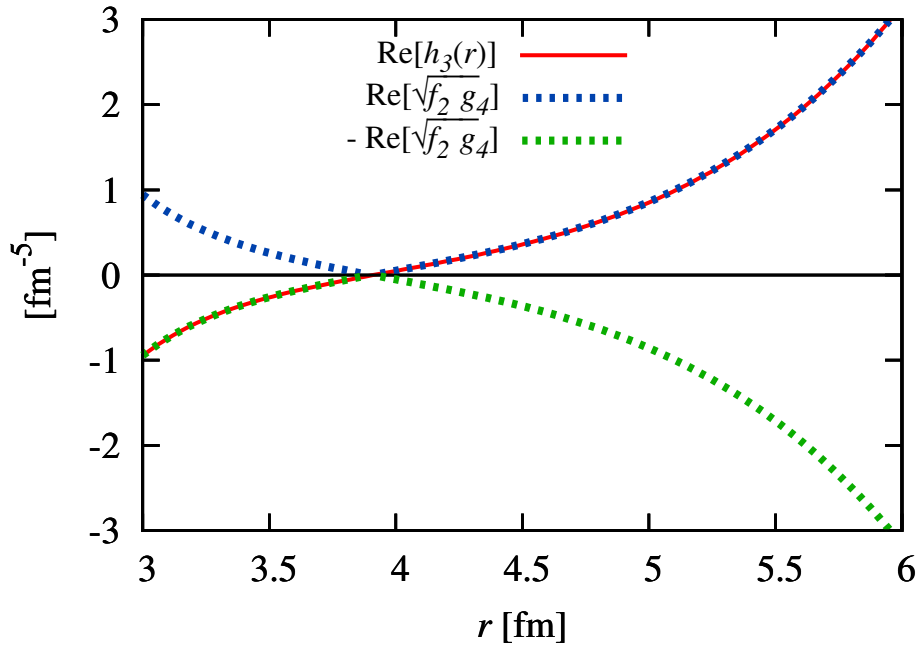


Figure 4.6 We plot $\text{Re}\left[\sqrt{f_2(r)g_4(r)}\right]$, $-\text{Re}\left[\sqrt{f_2(r)g_4(r)}\right]$, and $\text{Re}[h_3(r)]$ as functions of r for neutron-proton scattering in 3D_3 - 3G_3 coupled channel. The functions are rescaled by a factor of 0.01.

we show results for the causal range for all uncoupled channels by setting

$$r_\ell = b_\ell(r). \quad (4.91)$$

In Table 4.5 we determine the causal range for all coupled channels using Eqs. 4.61 - 4.62. Also, we find the Cauchy-Schwarz ranges shown in Table 4.6 using Eq. (4.60).

Table 4.4 The causal ranges for uncoupled channels.

Channels	1S_0	1P_1	3P_0	3P_1	1D_2	3D_2	1F_3	3F_3
R^b [fm]	1.27	0.31	3.07	0.23	3.98	4.91	1.88	1.56

Table 4.5 The causal ranges for coupled channels.

Channels	3S_1	3D_1	3P_2	3F_2	3D_3	3G_3
R^b [fm]	1.29	1.20	2.23	1.73	4.03	3.92

Table 4.6 The Cauchy-Schwarz ranges for coupled channels.

Channels	3S_1 - 3D_1	3P_2 - 3F_2	3D_3 - 3G_3
R^{C-S} [fm]	1.29	4.65	5.68

We find that in some channels the causal and Cauchy-Schwarz ranges are surprisingly large, and it is worthwhile to probe the origin of these large ranges. It is convenient to collect together some of the key formulas derived above. The Cauchy-Schwarz inequality has the form

$$f_{j-1}(r)g_{j+1}(r) \geq [h_j(r)]^2, \quad (4.92)$$

where

$$f_{j-1}(r) = b_{j-1}(r) - 2q_0^2 \frac{\Gamma(j + \frac{1}{2})\Gamma(j + \frac{3}{2})}{\pi} \left(\frac{r}{2}\right)^{-2j-1} - r_{j-1}, \quad (4.93)$$

$$g_{j+1}(r) = b_{j+1}(r) + \frac{2q_0^2}{a_{j+1}^2} \frac{\pi}{\Gamma(j + \frac{1}{2})\Gamma(j + \frac{3}{2})} \left(\frac{r}{2}\right)^{2j+1} - r_{j+1}, \quad (4.94)$$

$$h_j(r) = d_j(r) - q_1 \frac{2}{a_{j+1}}, \quad (4.95)$$

$$b_{j\mp 1}(r) = \frac{1}{a_{j\mp 1}^2} \frac{2\pi}{\Gamma(j\mp 1 + \frac{3}{2})\Gamma(j\mp 1 + \frac{5}{2})} \left(\frac{r}{2}\right)^{2(j\mp 1)+3} - \frac{1}{a_{j\mp 1}} \frac{4}{j\mp 1 + \frac{1}{2}} \left(\frac{r}{2}\right)^2 - \frac{2\Gamma(j\mp 1 - \frac{1}{2})\Gamma(j\mp 1 + \frac{1}{2})}{\pi} \left(\frac{r}{2}\right)^{-2(j\mp 1)+1}, \quad (4.96)$$

$$d_j(r) = \frac{-q_0}{a_{j-1}a_{j+1}} \frac{2\pi}{\Gamma(\frac{1}{2} + j)\Gamma(\frac{3}{2} + j)} \left(\frac{r}{2}\right)^{2j+1} + \frac{q_0}{a_{j+1}} \frac{4}{(2j-1)(2j+3)} r^2 - 2q_0 \frac{\Gamma(j + \frac{1}{2})\Gamma(j + \frac{3}{2})}{\pi} \left(\frac{r}{2}\right)^{-2j-1}. \quad (4.97)$$

We note that the leading power of r in $g_{j+1}(r)$ is

$$\frac{1}{a_{j+1}^2} \frac{2\pi}{\Gamma(j+1 + \frac{3}{2})\Gamma(j+1 + \frac{5}{2})} \left(\frac{r}{2}\right)^{2j+5}. \quad (4.98)$$

This has a very small numerical prefactor multiplying $a_{j+1}^{-2} r^{2j+5}$. For $j = 1$ the factor is $2/1575$, for $j = 2$ it is $2/99225$, and for $j = 3$ it is $2/9823275$. Therefore the term is negligible unless r is large compared with $(a_{j+1})^{1/(2j+3)}$. If we neglect this term, then the term with the leading power of r on the left hand side of Eq. (4.92) is the same as that on the right hand side,

$$\begin{aligned} & \frac{1}{a_{j-1}^2} \frac{2\pi}{\Gamma(j-1+\frac{3}{2})\Gamma(j-1+\frac{5}{2})} \left(\frac{r}{2}\right)^{2j+1} \cdot \frac{2q_0^2}{a_{j+1}^2} \frac{\pi}{\Gamma(j+\frac{1}{2})\Gamma(j+\frac{3}{2})} \left(\frac{r}{2}\right)^{2j+1} \\ &= \left[\frac{-q_0}{a_{j-1}a_{j+1}} \frac{2\pi}{\Gamma(\frac{1}{2}+j)\Gamma(\frac{3}{2}+j)} \left(\frac{r}{2}\right)^{2j+1} \right]^2. \end{aligned} \quad (4.99)$$

As a result the curves for $f_{j-1}(r)g_{j+1}(r)$ and $[h_j(r)]^2$ are approximately parallel for large r until the term that we have neglected becomes significant. These nearly parallel trajectories inflate the value of the Cauchy-Schwarz range $r = R^{\text{C-S}}$ where the two curves cross.

For the 3S_1 - 3D_1 coupled channel we find $R^{\text{C-S}}$ is about the same size as the Compton wavelength of the pion, $m_\pi^{-1} = 1.5$ fm. This is also comparable to what one expects for the range of the nucleon-nucleon interaction. However the results are more interesting for $j > 1$. In the 3P_2 - 3F_2 channel we have $R^{\text{C-S}} = 4.65$ fm. And for the 3D_3 - 3G_3 coupled channel we find $R^{\text{C-S}} = 5.68$ fm. These values are surprisingly large in comparison with m_π^{-1} .

4.7 One-Pion Exchange Potential

We note that there are some channels where the causal range R^b is also quite large. By definition $R^{\text{C-S}} \geq R^b$ and so the Cauchy-Schwarz range will then also be large. The causal range is the minimum value for r such that

$$f_{j-1}(r) = b_{j-1}(r) - 2q_0^2 \frac{\Gamma(j+\frac{1}{2})\Gamma(j+\frac{3}{2})}{\pi} \left(\frac{r}{2}\right)^{-2j-1} - r_{j-1} \geq 0 \quad (4.100)$$

for the lower partial wave, or

$$g_{j+1}(r) = b_{j+1}(r) + \frac{2q_0^2}{a_{j+1}^2} \frac{\pi}{\Gamma(j+\frac{1}{2})\Gamma(j+\frac{3}{2})} \left(\frac{r}{2}\right)^{2j+1} - r_{j+1} \geq 0 \quad (4.101)$$

for the higher partial wave. For uncoupled channels we take $q_0 = 0$.

The largest values for R^b occur when the effective range parameter is positive or near zero. See for example the causal ranges for the 1D_2 , 3D_2 , 3D_3 , and 3G_3 channels. What happens is that the function $f_{j-1}(r)$ or $g_{j+1}(r)$ remains negative with a rather small slope until r becomes quite large. The small slope is again associated with the fact that the term with the highest power of r has a small numerical prefactor.

The range of the interaction plays the dominant role in setting the causal range. In the language of local potentials, this is the radius at which the magnitude of the potential is numerically very small. However there is also some influence of the exponential tail of the potential upon the causal range.

In all channels where the causal range is unusually large, 1D_2 , 3D_2 , 3D_3 , and 3G_3 , we find that the tail of the one-pion exchange potential is attractive. At smaller radii, the potential crosses over at some classical turning point to become repulsive. See for example Figures 2 - 4 in Ref. [162].

The detailed mechanism requires further study, but it appears that this geometry can cause a near-threshold wavepacket to reflect before reaching the classical turning point, thus mimicking a longer range potential. However some fine tuning is needed to produce a large causal range, as there is no enhancement in the 1S_0 and 3S_1 channels and a smaller amount of enhancement in the 3P_0 channel.

There seems to be no such enhancement of the causal range in the 1P_1 , 3P_1 , and 3D_1 channels where the tail of the potential is repulsive. In fact, the causal range for the 1P_1 and 3P_1 channels

are unusually small. This appears to be related to quantum tunneling into the inner region where the potential is attractive.

In the following analysis we will investigate the importance of the tail of the one-pion exchange potential in setting the causal range, R^b . We show that even though the one-pion exchange potential is numerically small at distances larger than 5 fm, chopping off the one-pion exchange tail at such distances produces a non-negligible effect. The one-pion exchange potential tail appears to be the source of the large values for R^b in higher partial waves where the central one-pion exchange tail is attractive.

If we neglect electromagnetic effects, then the neutron-proton interaction potential at large distances is governed by the one-pion exchange (OPE) potential, which in configuration space is

$$V_{OPE}(r) = V_C(r) + S_{12}V_T(r). \quad (4.102)$$

Here $V_C(r)$ is the central potential,

$$V_C(r) = \frac{g_{\pi N}^2}{12\pi} \left(\frac{m_\pi}{2M_N} \right)^2 (\vec{\tau}_1 \cdot \vec{\tau}_2)(\vec{\sigma}_1 \cdot \vec{\sigma}_2) \frac{e^{-m_\pi r}}{r}, \quad (4.103)$$

$V_T(r)$ is the tensor potential,

$$V_T(r) = \frac{g_{\pi N}^2}{12\pi} \left(\frac{m_\pi}{2M_N} \right)^2 (\vec{\tau}_1 \cdot \vec{\tau}_2) \left(1 + \frac{3}{m_\pi r} + \frac{3}{(m_\pi r)^2} \right) \frac{e^{-m_\pi r}}{r}, \quad (4.104)$$

and S_{12} is the tensor operator,

$$S_{12} = 3(\vec{\sigma}_1 \cdot \hat{r})(\vec{\sigma}_2 \cdot \hat{r}) - \vec{\sigma}_1 \cdot \vec{\sigma}_2. \quad (4.105)$$

Here m_π is the pion mass, M_N is the nucleon mass, and $g_{\pi N} = 13.0$ is the pion-nucleon coupling

constant. The one-pion exchange potential is local in space and the interaction matrix in Eq. (4.12) takes the following form for $j = 1$,

$$W(r, r') = \begin{pmatrix} V_C(r) & \sqrt{8}V_T(r) \\ \sqrt{8}V_T(r) & V_C(r) - 2V_T(r) \end{pmatrix} \delta(r - r'). \quad (4.106)$$

In Figure (4.7) we plot $W_{11}(r) = V_C(r)$, $W_{12}(r) = W_{21}(r) = \sqrt{8}V_T(r)$, and $W_{22}(r) = V_C(r) - 2V_T(r)$ in the 3S_1 - 3D_1 coupled channel.

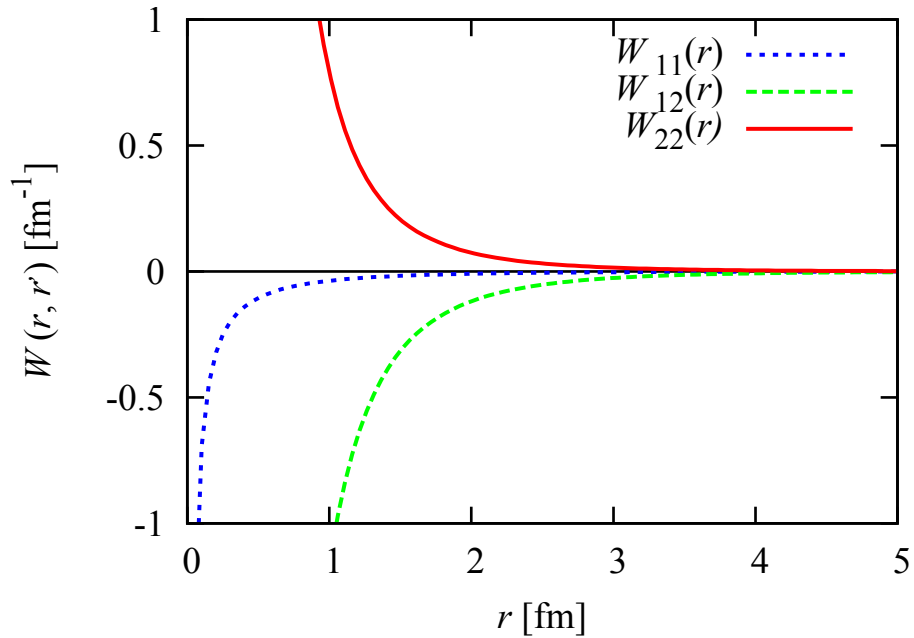


Figure 4.7 Plot of the potential matrix elements $W_{11}(r) = V_C(r)$, $W_{12}(r) = W_{21}(r) = \sqrt{8}V_T(r)$ and $W_{22}(r) = V_C(r) - 2V_T(r)$ as a function of r in the 3S_1 - 3D_1 coupled channel.

To demonstrate the origin of large causal ranges found in Table 4.4 and Table 4.5, we will present some simple but illustrative numerical examples. For each channel we add a short range potential to the one-pion exchange potential in order to reproduce the physical low-energy

scattering parameters. The specific model we use for the short range potential is not important to our general analysis nor is it the most economical. We choose a simple scheme which consists of three well-defined functions in three different regions and which is continuously differentiable everywhere. The potential has the form

$$V(r) = V_{\text{Gauss}}(r)\theta(R_{\text{Gauss}} - r) + V_{\text{Spline}}(r)\theta(r - R_{\text{Gauss}})\theta(R_{\text{Exch.}} - r) + V_{\text{Exch.}}(r)\theta(r - R_{\text{Exch.}}), \quad (4.107)$$

where θ is a unit step function.

The short-range part is a Gaussian function

$$V_{\text{Gauss}}(r) = C_G e^{-m_G^2 r^2}. \quad (4.108)$$

The intermediate-range part of the potential is a cubic spline use to connect the short- and long-range regions,

$$V_{\text{Spline}}(r) = C_1 + C_2 r + C_3 r^2 + C_4 r^3. \quad (4.109)$$

The long-range part consists of the usual one-pion exchange potential together with two additional heavy meson exchange terms,

$$V_{\text{Exch.}}(r) = V_C^{\pi,A,B}(r) + S_{12} V_T^{\pi,D,F}(r). \quad (4.110)$$

The central part of the potential is composed of Yukawa functions

$$V_C^{\pi,A,B}(r) = \frac{g^2 \pi N}{12\pi} \left(\frac{m_\pi}{2M_N} \right)^2 \left\{ C_\pi \frac{e^{-m_\pi r}}{r} + C_A \frac{e^{-m_A r}}{r} + C_B \frac{e^{-m_B r}}{r} \right\}, \quad (4.111)$$

and the tensor part of the potential has the form

$$V_T^{\pi,D,F}(r) = \frac{g_{\pi N}^2}{12\pi} \left(\frac{m_\pi}{2M_N} \right)^2 \left\{ C_\Pi \left[1 + \frac{3}{m_\pi r} + \frac{3}{(m_\pi r)^2} \right] \frac{e^{-m_\pi r}}{r} + C_D \left[1 + \frac{3}{m_D r} + \frac{3}{(m_D r)^2} \right] \frac{e^{-m_D r}}{r} + C_F \left[1 + \frac{3}{m_F r} + \frac{3}{(m_F r)^2} \right] \frac{e^{-m_F r}}{r} \right\}. \quad (4.112)$$

Here $C_\pi = (2\vec{S}^2 - 3)(2\vec{T}^2 - 3)$, $C_\Pi = 2\vec{T}^2 - 3$, $g_{\pi N} = 13.0$, $m_\pi = 140$ MeV, and $M_N = 938.0$ MeV. The coefficients which are not parts of the one-pion exchange potential are used as free parameters to reproduce the physical low-energy scattering parameters. Due to the abundance of free parameters, the fit process is not unique. However, in each case we attempt to qualitatively reproduce the shape of the NijmegenII potentials [162]. In each case the heavy meson masses are kept significantly larger than the pion mass. In Figure 4.8 we show the potential in the 1P_1 channel. Figure 4.9 shows the potential in the 1D_2 channel, and Figure 4.10 shows the potential in the 3D_2 channel.

After having recovered the physical low-energy scattering parameters, we now multiply an additional step function to the potential,

$$V(r) \rightarrow V(r)\theta(R-r), \quad (4.113)$$

which removes the tail of the potential beyond range R . We then recalculate the low-energy scattering parameters with this modification. The results are shown in Table 4.7 for the 1P_1 , 1D_2 , and 3D_2 channels. The causal ranges for the 1D_2 and 3D_2 channels are quite large for the physical scattering data, 4.0 and 4.9 fm, respectively. However, if we remove the tail of the model potential at $R = 5$ fm, the causal ranges drop to 2.4 and 2.7 fm respectively.

The tail of the model potential is dominated by the one-pion exchange potential. Even though the numerical size of the one-pion exchange potential is small at distances of 5 fm, these

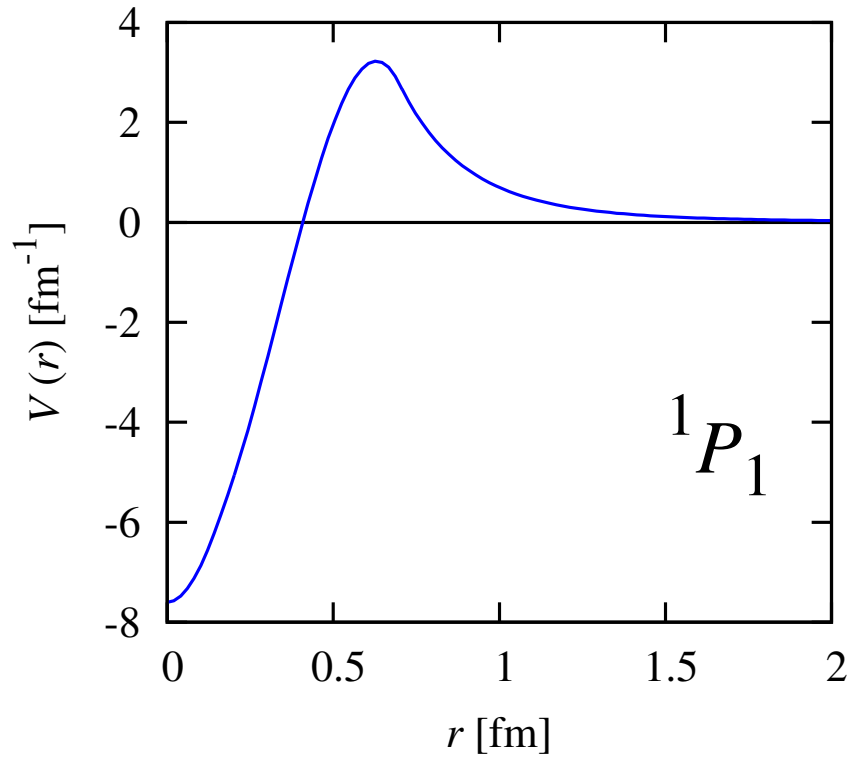


Figure 4.8 Plot of the model potential in the 1P_1 channel. In this channel $S = 0$, $T = 0$, $C_\pi = 9$, $C_A = 405.9$, $C_B = 769.5$, $C_\Pi = 0$, $C_D = 0$, $C_F = 0$, $C_G = -7.6$, $m_A = 10.0m_\pi$, $m_B = 5.45m_\pi$, $m_G = 4.46m_\pi$, $C_1 = -7.464$, $C_2 = 0.179$, $C_3 = 73.933$ and $C_4 = -78.011$. We use $R_{\text{Gauss}} = 0.2$ fm and $R_{\text{Exch.}} = 0.7$ fm.

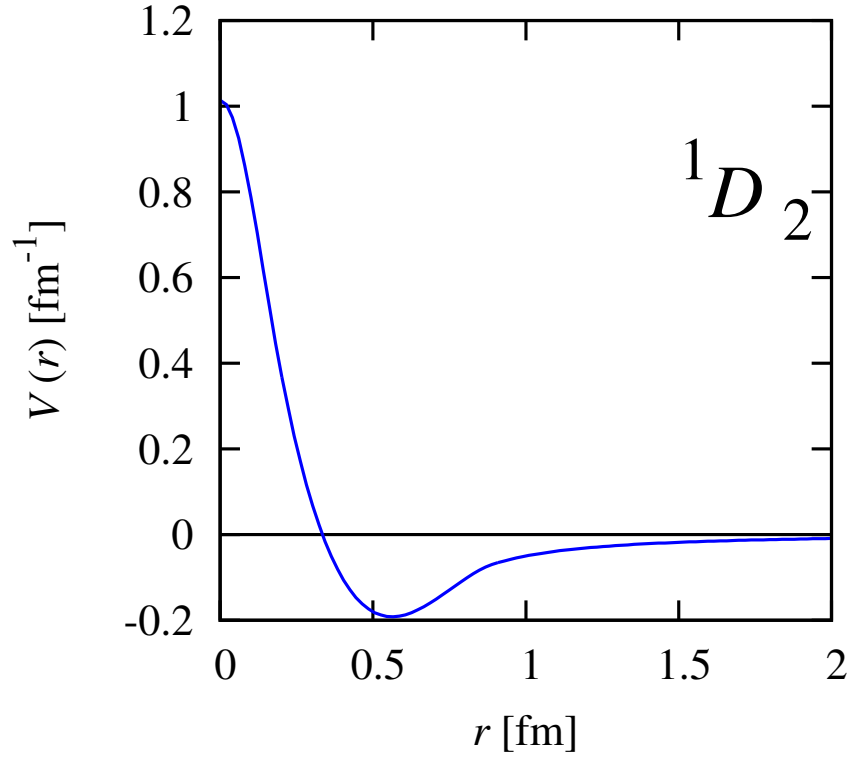


Figure 4.9 Plot of the model potential in the 1D_2 channel. In this channel $S = 0$, $T = 1$, $C_\pi = -3$, $C_A = -60.5$, $C_B = -30.0$, $C_\Pi = 0$, $C_D = 0$, $C_F = 0$, $C_G = 1.01$, $m_A = 9m_\pi$, $m_B = 6m_\pi$, $m_G = 7.02m_\pi$, $C_1 = 1.463$, $C_2 = -7.332$, $C_3 = 10.384$ and $C_4 = -4.585$. We use $R_{\text{Gauss}} = 0.2$ fm and $R_{\text{Exch.}} = 0.9$ fm.

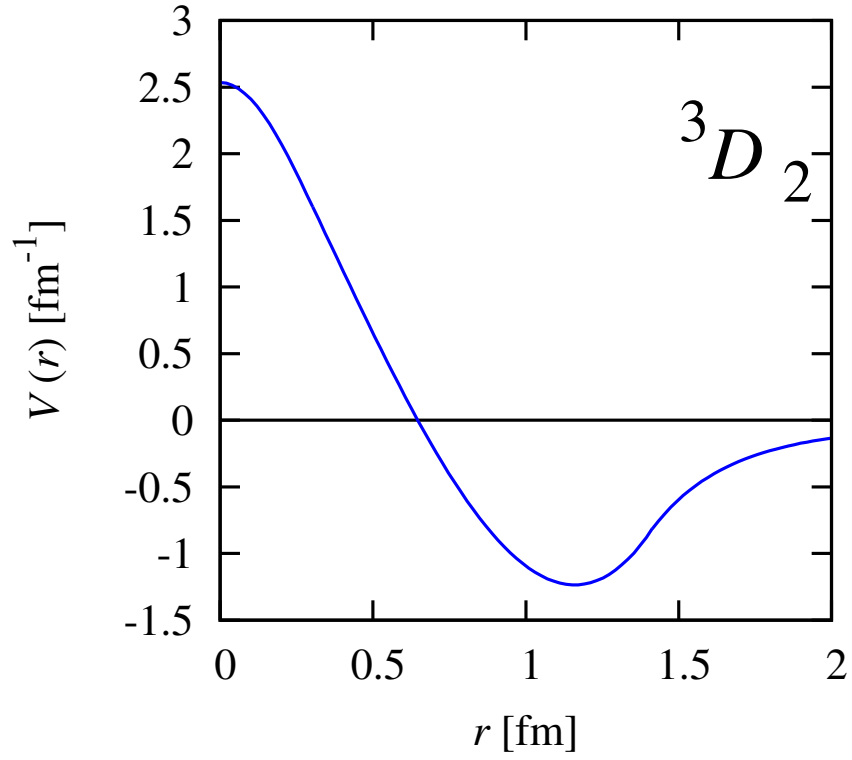


Figure 4.10 Plot of the model potential in the 3D_2 channel. In this channel $S = 1$, $T = 0$, $C_\pi = -3$, $C_A = -660$, $C_B = -1140$, $C_\Pi = -3$, $C_D = -930$, $C_F = -927$, $C_G = 2.53$, $m_A = m_D = 8m_\pi$, $m_B = m_F = 5m_\pi$, $m_G = 3.25m_\pi$, $C_1 = 2.979$, $C_2 = -4.026$, $C_3 = -2.455$ and $C_4 = 2.409$. We use $R_{\text{Gauss}} = 0.3$ fm and $R_{\text{Exch.}} = 1.4$ fm.

Table 4.7 The potential range dependence of the causal range in various channels.

Potential range Causal range	2 fm	5 fm	12 fm	15 fm	50 fm
$R_{1P_1}^b$	0.4	0.4	0.3	0.3	0.3
$R_{1D_2}^b$	2.0	2.4	3.8	4.0	4.0
$R_{3D_2}^b$	1.3	2.7	4.7	4.9	4.9

numerical results show clearly that the one-pion exchange tail is controlling the size of the causal range. The one-pion exchange potential tail appears to be the source of the large values for R^b in higher partial waves where the central one-pion exchange tail is attractive.

4.8 Summary and Conclusions

In this study we have derived the constraints of causality and unitarity for neutron-proton scattering for all spin channels up to $j = 3$. We have defined and calculated interaction length scales which we call the causal range, R^b , and the Cauchy-Schwarz range, R^{C-S} . The causal range is the minimum value for r such that the causal bounds,

$$f_{j-1}(r) = b_{j-1}(r) - 2q_0^2 \frac{\Gamma(j + \frac{1}{2})\Gamma(j + \frac{3}{2})}{\pi} \left(\frac{r}{2}\right)^{-2j-1} - r_{j-1} \geq 0, \quad (4.114)$$

$$g_{j+1}(r) = b_{j+1}(r) + \frac{2q_0^2}{a_{j+1}^2} \frac{\pi}{\Gamma(j + \frac{1}{2})\Gamma(j + \frac{3}{2})} \left(\frac{r}{2}\right)^{2j+1} - r_{j+1} \geq 0, \quad (4.115)$$

are satisfied. For uncoupled channels these bounds simplify to the form

$$f_\ell(r) = g_\ell(r) = b_\ell(r) - r_\ell \geq 0. \quad (4.116)$$

For coupled channels the Cauchy-Schwarz range is the minimum value for r satisfying the causal bounds as well as the Cauchy-Schwarz inequality,

$$f_{j-1}(r)g_{j+1}(r) \geq [h_j(r)]^2. \quad (4.117)$$

If one reproduces the physical scattering data using strictly finite range interactions, then the range of these interactions must be larger than R^b and R^{C-S} . From these bounds we have derived the general result that non-vanishing partial-wave mixing cannot be reproduced with zero-range interactions. As the range of the interaction goes to the zero, the effective range for the lower partial-wave channel is driven to negative infinity.

This finding has consequences for pionless effective theory where the range of the interactions is set entirely by the value of the cutoff momentum. If the cutoff momentum is too high, then it is impossible to obtain the correct threshold physics in coupled channels without violating causality or unitarity. In some channels we find that the causal range and Cauchy-Schwarz range are as large 5 fm. We have shown that these large values are driven by the tail of the one-pion exchange potential. In these channels the problems will be even more severe, and the cutoff momentum will need to be rather low in order to reproduce the physical scattering data in pionless effective field theory. How low this cutoff momentum must be depends on the particular regularization scheme.

We should note that all of these mixing observables are non-vanishing only when one reaches higher orders in the power counting expansion, and there is no direct impact on pionless effective field theory calculations at lower orders. See, for example, Ref. [38] for details on power counting in pionless effective field theory. In the zero-range limit, the term which drives

the negative divergence of the effective range parameter r_{j-1} is

$$-2q_0^2 \frac{\Gamma(j + \frac{1}{2})\Gamma(j + \frac{3}{2})}{\pi} \left(\frac{r}{2}\right)^{-2j-1}. \quad (4.118)$$

At leading order there is no divergence since there is no partial wave mixing and $q_0 = 0$. If higher-order terms are iterated non-perturbatively as in Ref. [167], then the divergence appears at order Q^2 , the first order at which q_0 is non-vanishing. If higher-order terms are iterated order-by-order in perturbation theory, then the term in Eq. (4.118) appears at order Q^4 . This is one order higher than the analysis presented in Ref. [38], and we predict that zero-range divergences in r_{j-1} will first appear at this order.

It is important to note that if one works order-by-order in perturbation theory, then the constraints of causality and unitarity always appear somewhat hidden. At every order in the effective field theory calculation there are new operator coefficients which appear and are determined by matching to physical data. There are no obstructions to setting these operator coefficients to reproduce physical values.

It is only when one iterates the new interactions, i.e., by solving the Schrödinger equation, that non-linear dependencies on the operator coefficients appear. In this case one finds that the constraints of causality and unitarity give necessary conditions for keeping the operator coefficients real. Once we fix the regularization, the bound corresponds with branch cuts of the effective theory when viewed as a function of physical scattering parameters.

These branch cuts cannot be seen at any finite order in perturbation theory. However a nearby branch point may spoil the convergence of the perturbative expansion. In this context, our causality and unitarity bounds can be viewed as setting physical constraints for the convergence of perturbative calculations in pionless effective field theory.

If the cutoff is taken too high, a branch cut develops which jeopardizes the convergence of the

perturbative calculation. Similarly if one does calculations using dimensional regularization, then the renormalization scale sets the scale at which the infrared and ultraviolet physics are regulated [85]. Similar problems with perturbative convergence would arise if the renormalization scale is taken too high.

There is much theoretical interest in the connection between dilute neutron matter and the universal physics of fermions in the unitarity limit [86, 25, 61, 117, 87, 177, 131]. In the limit of isospin symmetry our analysis of the isospin triplet channels can be applied to neutron-neutron scattering in dilute neutron matter. In this study we have shown there are intrinsic length scales associated with the causal range and the Cauchy-Schwarz range. When the average separation between neutrons is smaller than these length scales, one expects non-universal behavior controlled by the details of the neutron-neutron interactions. For the 1S_0 channel, $R^b = 1.3$ fm. For the 3P_2 channel, $R^b = 2.2$ fm, and for the 3F_2 channel, $R^b = 1.7$ fm. For 3P_2 - 3F_2 mixing, we find $R^{C-S} = 4.7$ fm. We see that the physics of 3P_2 - 3F_2 mixing will become non-universal at lower densities than the 1S_0 interactions. In particular the densities where 3P_2 superfluidity is expected to occur will be well beyond this universal regime.

van der Waals interactions

5.1 Introduction

Low-energy universality appears when there is a large separation between the short-distance scale of the interaction and the physically relevant long-distance scales. Some well-known examples include the unitarity limit of two-component fermions [138, 103, 180, 2, 113] and the Efimov effect in three-body and four-body systems [53, 54, 11, 144, 96, 168, 47, 93, 83, 110]. See Refs. [29, 88] for reviews of the subject and literature. There have been many theoretical studies of low-energy phenomena and universality for interactions with finite range. These studies have direct applications to nuclear physics systems such as cold dilute neutron matter or light nuclei such as the triton and alpha particle. To a good approximation, the van der Waals interactions between alkali-metal atoms can also be treated as a finite-range interaction.

However, there are some differences. For potentials with an attractive $1/r^\alpha$ tail and $\alpha > 2$, the s -wave scattering phase shift near threshold has been formulated in Ref. [133]. For $\alpha > 3$, the modified scattering parameters for an s -wave Feshbach resonance were derived in Ref. [156] using coupled-channel calculations. Analytical expressions for the s -wave scattering length and

effective range for two neutral atoms and $\alpha = 6$ have been derived in Ref. [66]. However, the applicability of the effective range theory is limited for interactions with attractive tails. In order to define the scattering length for angular momentum $\ell \geq 2$ and the effective range for $\ell \geq 1$, a modified version of effective range theory known as quantum-defect theory is needed [75, 79]. Furthermore, scattering parameters of magnetically tunable multichannel systems have been studied in the context of multichannel quantum-defect theory [146, 80]. See Ref. [155] for a very recent development of multichannel quantum-defect theory for higher partial waves. There is also growing empirical evidence that there exists a new type of low-energy universality that ties together all interactions with an attractive $1/r^6$ tail. This might seem surprising since there is no such analogous behavior for interactions with a Coulomb tail. In this chapter we derive the theoretical foundations for this van der Waals universality at low energies by studying the near-threshold behavior and the constraints of causality. We also show that this universality extends to any power-law interaction $1/r^\alpha$ with $\alpha \geq 2$ in any number of dimensions. Our analysis applies to energy-independent interactions. We first consider a single scattering channel but then also consider multichannel systems near a magnetic Feshbach resonance.

In our analysis we assume that the two-body potential has a long-distance attractive tail of the form $-C_6/r^6$. We define the van der Waals length scale, β_6 , as

$$\beta_6 = (2\mu C_6)^{\frac{1}{4}}, \quad (5.1)$$

where μ is the reduced mass of the scattering particles. For simplicity we use atomic units (a.u.) throughout our discussion. So, in particular, we set $\hbar = 1$. In Refs. [35, 151] it was noticed that an approximate universal relationship exists between the effective range and inverse scattering length for s -wave scattering in many different pairs of scattering alkali-metal atoms. If we write

A_0 as the scattering length and R_0 as the effective range, the relation is

$$R_0 \approx \frac{\beta_6 \Gamma(1/4)^2}{3\pi} - \frac{4\beta_6^2}{3A_0} + \frac{8\pi\beta_6^3}{3\Gamma(1/4)^2 A_0^2}. \quad (5.2)$$

This approximate relation becomes exact for a pure $-C_6/r^6$ potential. What is surprising about Eq. (5.2) is that the van der Waals length β_6 dominates over other length scales which characterize the short-distance repulsive force between alkali-metal atoms. This approximate universality suggests there is some separation of scales between the van der Waals length β_6 and the length scales of the short-range forces. This separation of scales will become more transparent later in our analysis when we determine the coefficients of the short-range \hat{K} -matrix. It would be useful to exploit the separation of scales as an effective field theory with an explicit van der Waals tail plus contact interactions. In this chapter, we discuss the constraints on such a van der Waals effective field theory.

We note that a similar dominance of the van der Waals length β_6 has been discovered for the three-body parameter in the Efimov effect [17, 169, 170]. In the analysis here we focus only on two-body systems. However, our analysis should be useful in developing the foundations for van der Waals effective field theory. This in turn could be used to investigate the Efimov effect and other low-energy phenomena in a model-independent way. An extension of our analysis may be useful to understand the recently observed universality of the three-body parameter for narrow Feshbach resonances [150].

The organization of this chapter is as follows. We first discuss the connection between causality bounds and effective field theory. Next we consider asymptotic solutions of the Schrödinger equation. After that, we derive causality bounds for the short-range \hat{K} -matrix and consider the impact of these results on van der Waals effective field theory. Then we discuss quantum-defect theory and calculate causal ranges for several examples of single-channel s -wave

scattering in alkali-metal atoms. We also consider the constraints of causality near magnetic Feshbach resonances. We then conclude with a summary and discussion.

5.2 Causality bounds and effective field theory

For an effective field theory with local contact interactions, the range of the interactions is controlled by the momentum cutoff scale. Problems with convergence can occur if the cutoff scale is set higher than the scale of the new physics not described by the effective theory. It is useful to have a quantitative measure of when problems may or may not appear, and this is where the causality bound provides a useful diagnostic tool. For each scattering channel we use the physical scattering parameters to compute the causal range, R^b , which is the minimum range for the interactions consistent with the requirements of causality and unitarity and discussed in details in Chapter 4. For any fixed cutoff scale, the causality bound marks a branch cut of the effective theory when viewed as a function of physical scattering parameters, see Chapter 4 and Ref. [107]. The coupling constants of the effective theory become complex for scattering parameters violating the causality bound. These branch cuts do not appear in perturbation theory, but they can spoil the convergence pattern of the perturbative expansion.

Wigner was the first to recognize the constraints of causality and unitarity for two-body scattering with finite-range interactions [174]. The time delay of a scattered wave packet is given by the energy derivative of the phase shift, $\Delta t = 2d\delta/dE$. It is clear that the incoming wave packet must first reach the interacting region before the outgoing wave packet can leave. So the causality bound can be viewed as a lower bound on the time delay, Δt . When applied to wave packets near threshold, the causality bound becomes an upper bound on the effective range parameter.

A brief historical review on the analysis of the constraints of causality and universality is

given in the introduction of Chapter 4. Also in that chapter we have presented the first study of coupled-channel systems with partial-wave mixing

5.3 Asymptotic solutions of the Schrödinger equation

We consider a system of two spinless particles interacting via a spherically symmetric finite range potential in the center-of-mass frame. In addition to the non-singular finite-range interactions parameterized by $W(r, r')$, we assume that there is a long-range local van der Waals potential $-C_6/r^6$ for $r > R$. The van der Waals length scale β_6 was defined in Eq. (5.1). As noted in the Introduction, we use atomic units where $\hbar = 1$. The radial Schrödinger equation is

$$\left[\frac{d^2}{dr^2} - \frac{\ell(\ell+1)}{r^2} + \frac{\beta_6^4}{r^6} \theta(r-R) + p^2 \right] U_\ell^{(p)}(r) = 2\mu \int_0^R dr' W(r, r') U_\ell^{(p)}(r'). \quad (5.3)$$

The step function $\theta(r-R)$ cuts off the long-range potential at distances less than R . This ensures that we satisfy the regularity condition discussed in Eq. (2.30) and avoids mathematical problems associated with unregulated singular potentials [68]. The general form of the solutions for Eq. (5.3) has been discussed by Gao in Ref. [78].

In order to simplify some of the more lengthy expressions to follow, we introduce dimensionless rescaled variables $r_s = r/\beta_6$, $p_s = \beta_6 p$, and $\rho_s = 1/(2r_s^2)$. In the outer region, $r > R$, the Schrödinger equation reduces to

$$\left[\frac{d^2}{dr^2} - \frac{\ell(\ell+1)}{r^2} + \frac{\beta_6^4}{r^6} + p^2 \right] U_\ell^{(p)}(r) = 0 \quad (5.4)$$

or

$$\left[\frac{d^2}{dr_s^2} - \frac{\ell(\ell+1)}{r_s^2} + \frac{1}{r_s^6} + p_s^2 \right] U_\ell^{(p)}(r) = 0. \quad (5.5)$$

The exact solutions for Eq. (5.5) have been studied in detail in Ref. [76] using the formalism of quantum-defect theory [157, 91, 92].

The van der Waals wave functions F_ℓ and G_ℓ are linearly independent solutions of Eq. (5.5). In order to write these out we first need several functions defined in Appendix A.3. The van der Waals wave functions F_ℓ and G_ℓ can be written as summations of Bessel and Neumann functions,

$$F_\ell(p, r) = \frac{r_s^{1/2}}{x_\ell^2(p_s) + y_\ell^2(p_s)} \left[x_\ell(p_s) \sum_{m=-\infty}^{\infty} b_m(p_s) J_{\nu+m}(\rho_s) - y_\ell(p_s) \sum_{m=-\infty}^{\infty} b_m(p_s) N_{\nu+m}(\rho_s) \right], \quad (5.6)$$

$$G_\ell(p, r) = \frac{r_s^{1/2}}{x_\ell^2(p_s) + y_\ell^2(p_s)} \left[x_\ell(p_s) \sum_{m=-\infty}^{\infty} b_m(p_s) N_{\nu+m}(\rho_s) + y_\ell(p_s) \sum_{m=-\infty}^{\infty} b_m(p_s) J_{\nu+m}(\rho_s) \right]. \quad (5.7)$$

The function x_ℓ is defined in Eq. (A.52), and y_ℓ is defined in Eq. (A.53). For $m \geq 0$ the function b_m is given in Eq. (A.47), while b_{-m} is given in Eq. (A.48). The offset ν appearing in the order of the Bessel functions is given by the solution of Eq. (A.51) in Appendix A.3. For notational convenience, however, we omit writing the explicit p_s dependence of ν . Let us define $\delta_\ell^{(\text{short})}(p)$ to be the phase shift of the van der Waals wave functions due to the scattering from the short-range interaction. The normalization of $U_\ell^{(p)}(r)$ is chosen so that, for $r > R$,

$$U_\ell^{(p)}(r) = F_\ell(p, r) - \tan \delta_\ell^{(\text{short})}(p) G_\ell(p, r). \quad (5.8)$$

Our van der Waals wave functions are related to the functions f_ℓ^{c0} and g_ℓ^{c0} defined of Ref. [78] by

the normalization factors $F_\ell = f_\ell^{c0}/\sqrt{2}$ and $G_\ell = -g_\ell^{c0}/\sqrt{2}$. Henceforth, we write all expressions in terms of the short-range reaction matrix

$$\mathbf{K}_\ell(p) = \tan \delta_\ell^{(\text{short})}(p), \quad (5.9)$$

which is related to the short-range scattering matrix via

$$\mathbf{S}_\ell = e^{2i\delta_\ell^{(\text{short})}} = \frac{i - \mathbf{K}_\ell}{i + \mathbf{K}_\ell}. \quad (5.10)$$

For any finite-range interaction, \mathbf{K}_ℓ is analytic in p^2 and can be calculated by matching solutions for $r \leq R$ and $r > R$ at the boundary. It can be written in compact form as

$$\mathbf{K}_\ell = \frac{W(U_\ell^{(p)}, F_\ell^{(p)})}{W(U_\ell^{(p)}, G_\ell^{(p)})} \Big|_{r=R}, \quad (5.11)$$

where $U_\ell^{(p)}$ is the solution of Eq. (5.3) that is regular at the origin, and W denotes the Wronskian of two functions,

$$W(f, g) = fg' - f'g.$$

5.4 Causality bounds for short-range K-matrix \mathbf{K}_ℓ

In this section we derive causality bounds for the short-range K-matrix. For this we need to expand the wave function $U_\ell^{(p)}(r)$ in powers of p^2 . The steps we follow are analogous to those used in Chapter 4 [cf. in Refs. [94, 95, 107]]. We first expand \mathbf{K}_ℓ ,

$$\mathbf{K}_\ell = \tan \delta_\ell^{(\text{short})}(p) = \sum_{n=0}^{\infty} K_{\ell,2n} p^{2n}. \quad (5.12)$$

The first two terms $K_{\ell,0}$ and $K_{\ell,2}$ are analogous to the inverse scattering length and effective range parameters in the usual effective range expansion. The higher-order terms can be regarded as analogs of the shape parameters. Next we expand the van der Waals wave functions in powers of p^2 ,

$$F_{\ell}(p, r) = f_{\ell,0}(r) + f_{\ell,2}(r) p^2 + O(p^4), \quad (5.13)$$

$$G_{\ell}(p, r) = g_{\ell,0}(r) + g_{\ell,2}(r) p^2 + O(p^4). \quad (5.14)$$

In the following, we define

$$\nu_0 = \frac{1}{4}(2\ell + 1),$$

which corresponds to the value of ν at threshold. Using the low-energy expansions in Appendix A.4, we find that the coefficients in Eq. (5.13) are

$$f_{\ell,0}(r) = r_s^{1/2} J_{\nu_0}(\rho_s) \quad (5.15)$$

and

$$f_{\ell,2}(r) = \frac{\Gamma(\nu_0)\Gamma(2\nu_0 - 1)}{\Gamma(\nu_0 + 1)\Gamma(2\nu_0)} \frac{\beta_6^2}{16} r_s^{1/2} [J_{\nu_0-1}(\rho_s) + N_{\nu_0}(\rho_s)] \\ - \frac{\Gamma(\nu_0)\Gamma(2\nu_0 + 1)}{\Gamma(\nu_0 + 1)\Gamma(2\nu_0 + 2)} \frac{\beta_6^2}{16} r_s^{1/2} [J_{\nu_0+1}(\rho_s) - N_{\nu_0}(\rho_s)]. \quad (5.16)$$

Similarly, the coefficients in Eq. (5.14) are

$$g_{\ell,0}(r) = r_s^{1/2} N_{\nu_0}(\rho_s) \quad (5.17)$$

and

$$g_{\ell,2}(r) = \frac{\Gamma(\nu_0)\Gamma(2\nu_0-1)}{\Gamma(\nu_0+1)\Gamma(2\nu_0)} \frac{\beta_6^2}{16} r_s^{1/2} [N_{\nu_0-1}(\rho_s) - J_{\nu_0}(\rho_s)] \\ - \frac{\Gamma(\nu_0)\Gamma(2\nu_0+1)}{\Gamma(\nu_0+1)\Gamma(2\nu_0+2)} \frac{\beta_6^2}{16} r_s^{1/2} [N_{\nu_0+1}(\rho_s) + J_{\nu_0}(\rho_s)]. \quad (5.18)$$

Using Eq. (5.8), we can now express $U_\ell^{(p)}(r)$ as an expansion in powers of p^2 . For $r > R$, we have

$$U_\ell^{(p)}(r) = f_{\ell,0}(r) - K_{\ell,0} g_{\ell,0}(r) \\ + p^2 [f_{\ell,2}(r) - K_{\ell,0} g_{\ell,2}(r) - K_{\ell,2} g_{\ell,0}(r)] + O(p^4). \quad (5.19)$$

We now consider two solutions of the Schrödinger equation $U_\ell^{(p_a)}(r)$ and $U_\ell^{(p_b)}(r)$ with momenta p_a and p_b , respectively. We have

$$\left[\frac{d^2}{dr^2} - \frac{\ell(\ell+1)}{r^2} + \frac{\beta_6^4}{r^6} \theta(r-R) + p_a^2 \right] U_\ell^{(p_a)}(r) = 2\mu \int_0^R dr' W(r,r') U_\ell^{(p_a)}(r'), \quad (5.20)$$

$$\left[\frac{d^2}{dr^2} - \frac{\ell(\ell+1)}{r^2} + \frac{\beta_6^4}{r^6} \theta(r-R) + p_b^2 \right] U_\ell^{(p_b)}(r) = 2\mu \int_0^R dr' W(r,r') U_\ell^{(p_b)}(r'). \quad (5.21)$$

Following the same steps as in Section 2.5.3, we obtain the Wronskian integral formula

$$\frac{W[U_\ell^{(p_b)}, U_\ell^{(p_a)}](r)}{p_b^2 - p_a^2} = \int_0^r U_\ell^{(p_a)}(r') U_\ell^{(p_b)}(r') dr', \quad (5.22)$$

for any $r > R$. Using Eq. (5.19) for momenta p_a and p_b we find

$$\begin{aligned} \frac{W[U_\ell^{(b)}, U_\ell^{(a)}](r)}{p_b^2 - p_a^2} &= W[f_{\ell,2}, f_{\ell,0}](r) - K_{\ell,0} \{W[g_{\ell,2}, f_{\ell,0}](r) + W[f_{\ell,2}, g_{\ell,0}](r)\} \\ &\quad + K_{\ell,0}^2 W[g_{\ell,2}, g_{\ell,0}](r) - K_{\ell,2} W[g_{\ell,0}, f_{\ell,0}](r) + O(p_a^2, p_b^2). \end{aligned} \quad (5.23)$$

In the Wronskian integral formula Eq. (5.22), we set $p_a = 0$ and take the limit $p_b \rightarrow 0$. With the wave function at zero energy written as $U_\ell^{(0)}$, the result is

$$K_{\ell,2} = b_\ell^{\text{vdW}}(r) - \frac{\pi}{4} \int_0^r [U_\ell^{(0)}(r')]^2 dr', \quad (5.24)$$

where

$$\begin{aligned} b_\ell^{\text{vdW}}(r) &= \frac{\pi}{4} W[f_{\ell,2}, f_{\ell,0}](r) + \frac{\pi}{4} K_{\ell,0}^2 W[g_{\ell,2}, g_{\ell,0}](r) \\ &\quad - \frac{\pi}{4} K_{\ell,0} \{W[g_{\ell,2}, f_{\ell,0}](r) + W[f_{\ell,2}, g_{\ell,0}](r)\}. \end{aligned} \quad (5.25)$$

The Wronskians appearing in Eq. (5.25) can be written out explicitly as

$$\begin{aligned} W[f_{\ell,2}, f_{\ell,0}](r) &= \frac{\beta_6 \rho_s}{16\nu_0(2\nu_0 - 1)} [J_{\nu_0-2}(\rho_s) J_{\nu_0}(\rho_s) - J_{\nu_0-1}^2(\rho_s)] \\ &\quad + \frac{\beta_6 \rho_s}{16\nu_0(2\nu_0 + 1)} [J_{\nu_0+2}(\rho_s) J_{\nu_0}(\rho_s) - J_{\nu_0+1}^2(\rho_s)] \\ &\quad + \frac{\beta_6 \rho_s}{4(2\nu_0 - 1)(2\nu_0 + 1)} \left[J_{\nu_0+1}(\rho_s) J_{\nu_0-1}(\rho_s) - J_{\nu_0}^2(\rho_s) + \frac{4}{\pi \rho_s} \right], \end{aligned} \quad (5.26)$$

$$\begin{aligned}
W[g_{\ell,2}, g_{\ell,0}](r) &= \frac{\beta_6 \rho_s}{16\nu_0(2\nu_0 - 1)} [N_{\nu_0-2}(\rho_s) N_{\nu_0}(\rho_s) - N_{\nu_0-1}^2(\rho_s)] \\
&+ \frac{\beta_6 \rho_s}{16\nu_0(2\nu_0 + 1)} [N_{\nu_0+2}(\rho_s) N_{\nu_0}(\rho_s) - N_{\nu_0+1}^2(\rho_s)] \\
&+ \frac{\beta_6 \rho_s}{4(2\nu_0 - 1)(2\nu_0 + 1)} \left[N_{\nu_0+1}(\rho_s) N_{\nu_0-1}(\rho_s) - N_{\nu_0}^2(\rho_s) + \frac{4}{\pi \rho_s} \right], \quad (5.27)
\end{aligned}$$

and

$$\begin{aligned}
W[g_{\ell,2}, f_{\ell,0}](r) &= W[f_{\ell,2}, g_{\ell,0}](r) \\
&= \frac{\beta_6 \rho_s}{16\nu_0(2\nu_0 - 1)} \{ J_{\nu_0-1}(\rho_s) [N_{\nu_0+1}(\rho_s) - N_{\nu_0-1}(\rho_s)] - N_{\nu_0}(\rho_s) [J_{\nu_0}(\rho_s) - J_{\nu_0-2}(\rho_s)] \} \\
&- \frac{\beta_6 \rho_s}{16\nu_0(2\nu_0 + 1)} \{ J_{\nu_0+1}(\rho_s) [N_{\nu_0+1}(\rho_s) - N_{\nu_0-1}(\rho_s)] - N_{\nu_0}(\rho_s) [J_{\nu_0+2}(\rho_s) - J_{\nu_0}(\rho_s)] \}. \quad (5.28)
\end{aligned}$$

The fact that the integral on the right-hand side of Eq. (5.24) is positive semidefinite sets an upper bound on the short-range parameter $K_{\ell,2}$. We find that

$$K_{\ell,2} \leq b_{\ell}^{\text{vdW}}(r) \quad (5.29)$$

for any $r > R$.

5.5 Impact on effective field theory

In this section we discuss the impact of our causality bounds for an effective field theory with short-range interactions and an attractive $1/r^6$ tail. In Figure 5.1 we plot the $\ell = 0$ Wronskians $W[f_{0,2}, f_{0,0}]$, $W[g_{0,2}, g_{0,0}]$, and $W[g_{0,2}, f_{0,0}]$ for $\beta_6 = 50$ (a.u.). Figure 5.2 and Figure 5.3 show the analogous plots for $\ell = 1$ and $\ell = 2$, respectively.

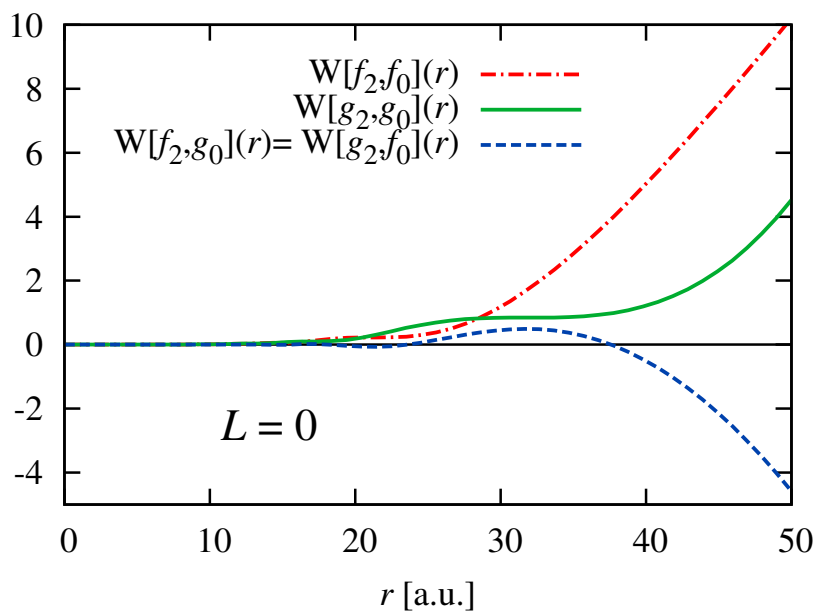


Figure 5.1 (Color online) Plot of $W[f_{0,2}, f_{0,0}](r)$, $W[g_{0,2}, g_{0,0}](r)$, and $W[g_{0,2}, f_{0,0}](r)$ as a function of r for $\ell = 0$ and $\beta_6 = 50$ (a.u.).

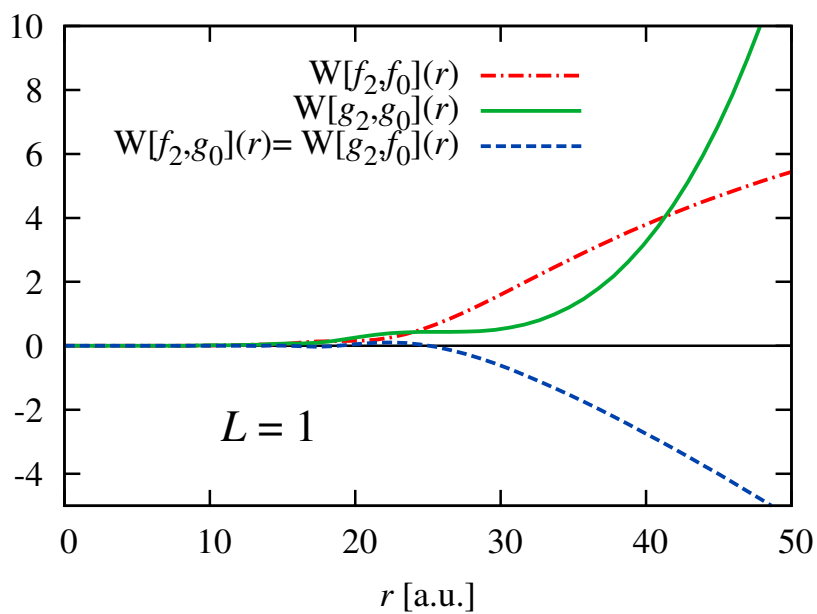


Figure 5.2 (Color online) Plot of $W[f_{1,2}, f_{1,0}](r)$, $W[g_{1,2}, g_{1,0}](r)$, and $W[g_{1,2}, f_{1,0}](r)$ as a function of r for $\ell = 1$ and $\beta_6 = 50$ (a.u.).

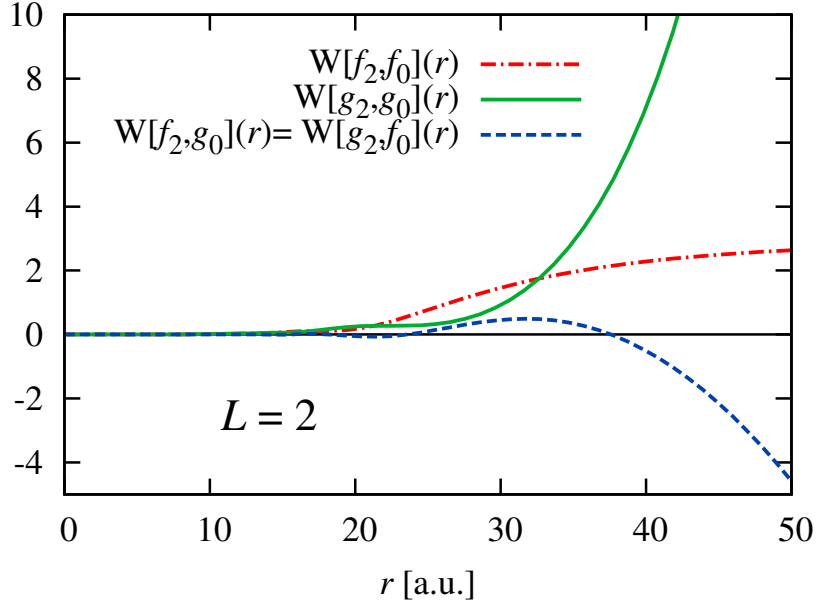


Figure 5.3 (Color online) Plot of $W[f_{2,2}, f_{2,0}](r)$, $W[g_{2,2}, g_{2,0}](r)$, and $W[g_{2,2}, f_{2,0}](r)$ as a function of r for $\ell = 2$ and $\beta_6 = 50$ (a.u.).

We note that all of the Wronskian functions in Figures 5.1–5.3 vanish in the limit $r \rightarrow 0$. This stands in clear contrast to what one finds for purely finite-range interactions [94, 95]. In that case the effective range parameter, r_ℓ , satisfies the upper bound

$$r_\ell \leq b_\ell(r), \quad (5.30)$$

where the function $b_\ell(r)$ is given in Eq. (4.9) [cf. Eq. (60) in Ref. [95]]

$$b_\ell(r) = -\frac{2\Gamma(\ell - \frac{1}{2})\Gamma(\ell + \frac{1}{2})}{\pi} \left(\frac{r}{2}\right)^{-2\ell+1} - \frac{4}{\ell + \frac{1}{2}} \frac{1}{a_\ell} \left(\frac{r}{2}\right)^2 + \frac{2\pi}{\Gamma(\ell + \frac{3}{2})\Gamma(\ell + \frac{5}{2})} \frac{1}{a_\ell^2} \left(\frac{r}{2}\right)^{2\ell+3}, \quad (5.31)$$

and a_ℓ is the scattering length. As already discussed in Section 4.5.1 near $r = 0$ the behavior of

$b_\ell(r)$ is

$$b_\ell(r) = -\frac{2\Gamma(\ell - \frac{1}{2})\Gamma(\ell + \frac{1}{2})}{\pi} \left(\frac{r}{2}\right)^{-2\ell+1} + O(r^2). \quad (5.32)$$

We see that $b_\ell(r)$ diverges to negative infinity as $r \rightarrow 0$ for $\ell \geq 1$. The causality bound on r_ℓ also drives r_ℓ to negative infinity for $\ell \geq 1$,

$$r_\ell \leq -\frac{2\Gamma(\ell - \frac{1}{2})\Gamma(\ell + \frac{1}{2})}{\pi} \left(\frac{r}{2}\right)^{-2\ell+1} + O(r^2). \quad (5.33)$$

For an effective field theory with local contact interactions, the range of the interactions are controlled by the momentum cutoff scale. No matter the values for a_ℓ and r_ℓ , it is not possible to take the momentum cutoff scale arbitrarily high without violating the causality bound for channels with angular momentum $\ell \geq 1$. For finite-range interactions with an additional attractive or repulsive Coulomb tail, one finds the same leading behavior [107]¹

$$b_\ell^{\text{Coulomb}}(r) = -\frac{2\Gamma(\ell - \frac{1}{2})\Gamma(\ell + \frac{1}{2})}{\pi} \left(\frac{r}{2}\right)^{-2\ell+1} + O(r^{-2\ell}), \quad (5.34)$$

i.e., the only difference in the causality bound relation for the Coulomb-modified effective range is the subleading $O(r^{-2\ell})$ pole term which is absent in the purely finite-range case. Hence, also for an effective field theory with contact interactions and long-range Coulomb tail, it is not possible to take the momentum cutoff scale arbitrarily high for $\ell \geq 1$ without violating the causality bound.

There is no such divergence in $b_\ell^{\text{vdW}}(r)$ at $r = 0$ for the attractive $1/r^6$ interaction. For an effective field theory with contact interactions and van der Waals tail, the causality bound does not impose convergence problems as long as $K_{\ell,2}$ is less than or equal to zero. This holds true for

¹To get this analogy, we use here the normalization of the Coulomb-modified effective range expansion found in Eq. (28) of Ref. [107] and insert it in Eqs. (64), (A.6), and (A.7) of the same paper, which give the explicit expressions for the Coulomb-modified causality bound functions for $\ell = 0, 1, 2$. The statement for arbitrary ℓ then follows by generalization.

any ℓ . There is no constraint from causality and unitarity preventing one from taking the cutoff momentum to be arbitrarily large. The key difference between the van der Waals interaction and the Coulomb interaction is that, when extended all the way to the origin, the attractive $1/r^6$ interaction is singular and the spectrum is unbounded below. An essential singularity appears at $r = 0$, and both van der Waals wave functions F_ℓ and G_ℓ vanish at the origin.

These exact same features appear in any attractive $1/r^\alpha$ interaction for $\alpha > 2$ in any number of spatial dimensions. The same can be said about an attractive $1/r^2$ interaction when the coupling constant is strong enough to form bound states. The key point is that in the zero-range limit of these attractive singular potentials, the spectrum of bound states extends to arbitrarily large negative energies. As a consequence, the scattering wave functions above threshold must vanish at the origin in order to satisfy orthogonality with respect to all such bound-state wave functions localized near the origin. In all of these cases the function $b_\ell^{\text{vdW}}(r)$ remains finite as $r \rightarrow 0$ for any ℓ . We conclude that for an effective field theory with contact interactions and attractive singular power-law interactions, we can take the cutoff momentum arbitrarily large for any ℓ without producing a divergence in the coefficient $K_{\ell,2}$ of the short-range K-matrix.

5.6 Quantum defect theory and the modified effective range expansion

Up to now we have been discussing the short-range phase shift of K-matrix for scattering relative to the van der Waals wave functions F_ℓ and G_ℓ . For power-law interactions $1/r^\alpha$ with $\alpha > 2$, we also have the option to define phase shifts relative to the Bessel functions of the free wave equation. The problem though is that the usual effective range expansion given in Eq. (2.36) is spoiled by nonanalytic terms as a function of p^2 . For the van der Waals interactions in the $\ell = 0$

channel, the leading nonanalytic term is proportional to p^3 , and so the scattering parameters a_0 and r_0 are well defined, but coefficients in higher order terms of the expansion are not. For $\ell = 1$ the leading nonanalytic term is proportional to p and so only the scattering length a_1 is well defined. For $\ell \geq 2$ none of the low-energy scattering parameters are well defined. To resolve these problems, a modified form of the effective range expansion is used which is known as quantum-defect theory [157, 91, 92].

In quantum-defect theory for attractive $1/r^6$ potentials, one defines an offset for the phase shift [79],

$$\eta_\ell = \frac{\pi}{2}(\nu - \nu_0). \quad (5.35)$$

The modified effective range expansion is then

$$p^{2\ell+1} \cot(\delta_\ell + 2\eta_\ell) = -\frac{1}{A_\ell} + \frac{1}{2}R_\ell p^2 + O(p^4 \ln p), \quad (5.36)$$

where A_ℓ and R_ℓ are the generalized scattering length and effective range parameters. These definitions coincide with the usual scattering length a_ℓ for $\ell = 0, 1$ and the usual effective range r_ℓ for $\ell = 0$. The generalized scattering length and effective range can be written in terms of the short-range K-matrix parameters as

$$A_\ell = \frac{\pi^2 \beta_6^{2\ell+1}}{2^{4\ell+1} [\Gamma(\frac{\ell}{2} + \frac{1}{4}) \Gamma(\ell + \frac{3}{2})]^2} \left[(-1)^\ell - \frac{1}{K_{\ell,0}} \right] \quad (5.37)$$

and

$$R_\ell = -\frac{2^{4\ell+2} \Gamma(\frac{\ell}{2} + \frac{1}{4})^2 \Gamma(\ell + \frac{3}{2})^2 \beta_6^{-2\ell-1}}{\pi^2 [K_{\ell,0} (-1)^\ell - 1]^2} \left[\frac{\beta_6^2 (K_{\ell,0}^2 + 1)}{4\ell^2 + 4\ell - 3} - K_{\ell,2} \right]. \quad (5.38)$$

From these results we see that the short-range parameter $K_{\ell,2}$ appears in combination with β_6^2 . But in nearly all single-channel scatterings between pairs of alkali-metal atoms, from the

following equation,

$$K_{\ell,2} = \frac{\beta_6^2}{4\ell^2 + 4\ell - 3} \left\{ 1 + \left[(-1)^\ell - A_\ell \frac{2^{4\ell+1} \Gamma\left(\frac{\ell}{2} + \frac{1}{4}\right)^2 \Gamma\left(\ell + \frac{3}{2}\right)^2}{\pi^2 \beta_6^{2\ell+1}} \right]^{-2} \right\} \\ + R_\ell A_\ell^2 \frac{2^{4\ell} \Gamma\left(\frac{\ell}{2} + \frac{1}{4}\right)^2 \Gamma\left(\ell + \frac{3}{2}\right)^2}{\pi^2 \beta_6^{2\ell+1}} \left[(-1)^\ell - A_\ell \frac{2^{4\ell+1} \Gamma\left(\frac{\ell}{2} + \frac{1}{4}\right)^2 \Gamma\left(\ell + \frac{3}{2}\right)^2}{\pi^2 \beta_6^{2\ell+1}} \right]^{-2}, \quad (5.39)$$

one quantitatively finds that $K_{\ell,2}$ is at least one order of magnitude smaller than β_6^2 . This separation of scales is the reason for the approximate universality found in Refs. [35, 151].

The dominance of β_6^{2n} over the subleading coefficients $K_{\ell,2n}$ in Eq. (5.12) for $n \geq 1$ holds for nearly all cases of single-channel scattering between alkali-metal atoms [75, 77]. This phenomenological fact explains the absence of short-distance length scales in the universality relation in Eq. (5.2). Furthermore, Gao has shown that when short-range interactions arise from a repulsive central potential, the fact that the K-matrix is nearly independent of energy means that the K-matrix is also nearly independent of angular momentum ℓ [77]. This produces a surprisingly rich class of universal physics for single-channel van der Waals interactions where $K_{\ell,2n}$ is negligible compared to β_6^{2n} for all ℓ , and $K_{\ell,0}$ is approximately the same for all ℓ . Therefore β_6 and the s -wave scattering length will determine, to a good approximation, the threshold scattering behavior for all values of ℓ .

5.7 Causal range for single-channel scattering

We have shown that for negative $K_{\ell,2} \leq 0$, the range R of the short-range interaction can be taken all the way down to zero. But when $K_{\ell,2}$ is positive, there is a constraint on R and we use

Eq. (5.29) to determine the causal range R^b ,

$$K_{\ell,2} = b_{\ell}^{\text{vdW}}(R^b). \quad (5.40)$$

As pointed out in Ref. [107], one can show *a priori* that $b_{\ell}^{\text{vdW}}(r)$ is a monotonically increasing function of r . Therefore, if a real solution to Eq. (5.40) exists, then it is unique. If, however, there is no real solution, then there is no constraint on the interaction range and we define R^b to be zero. For an effective field theory with contact interactions and van der Waals tail, the cutoff momentum can be made as large as $\sim 1/R^b$ before the causality bound is violated.

In the following analysis we extract the single-channel s -wave effective range parameters a_0 and r_0 for several different pairs of alkali-metal atoms ${}^7\text{Li}$, ${}^{23}\text{Na}$, and ${}^{133}\text{Cs}$ in singlet and triplet channels. The data is taken from Refs. [40, 41, 129, 66, 75]. The reduced masses for ${}^7\text{Li}_2$, ${}^{23}\text{Na}_2$, and ${}^{133}\text{Cs}_2$ are $\mu = 6394.7, 20954, 121100$ (a.u.), respectively. The van der Waals coupling constants for ${}^7\text{Li}_2$, ${}^{23}\text{Na}_2$, and ${}^{133}\text{Cs}_2$ are $C_6 = 1388, 1472, 7020$ (a.u.). We calculate the corresponding K-matrix parameters using Eq. (5.37) and Eq. (5.39) and then compute the resulting causal ranges. We recall that for $\ell = 0$ we simply have $A_0 = a_0$ and $R_0 = r_0$. The results for the scattering parameters and causal ranges are given in columns II, V and VI of Table 5.1. The discrepancies in R_0 are due to the fact that in the analytic studies in Refs. [66, 75] $K_{0,2}$ is neglected, while the numerical calculations of Refs. [40, 41, 129] include the short-range contribution from $K_{0,2}$.

In column V of Table 5.1, we present an approximate range for $K_{0,2}$ for each atomic pair using the values for R_0 in columns III and IV. Since $K_{0,2}$ is positive, we cannot go all the way to the zero-range limit. However, in each case $K_{0,2}$ is at least one order of magnitude smaller than β_6^2 .² Although we cannot take the zero-range limit, the causal ranges are small in comparison to

²Note that $K_{\ell,2}$ has the dimension of an area (in the appropriate atomic units).

Table 5.1 Scattering parameters and causal ranges for s -wave scattering of ${}^7\text{Li}$, ${}^{23}\text{Na}$, and ${}^{133}\text{Cs}$ pairs. The scattering data collection is taken from Ref. [66]. In columns I and IV the scattering data for ${}^7\text{Li}$ are from Ref. [41], the scattering data for ${}^{23}\text{Na}$ are from Refs. [40, 41], and data for ${}^{133}\text{Cs}$ are from Ref. [129]. In column III the effective range parameters, R_0 , are calculated analytically in Refs. [66, 75]. In column IV, the R_0 are obtained from numerical calculations. The scattering parameters in columns II and V are calculated using Eq. (5.37) and Eq. (5.39), and the causal ranges in column VI are obtained from Eq. (5.40).

		I	II	III	IV	V	VI	
Atoms	State	β_6	A_0	$K_{0,0}$	R_0	R_0	$K_{0,2}$	R^b
${}^7\text{Li}-{}^7\text{Li}$	${}^1\Sigma_g$	64.9097	36.9	-5.282	66.3	66.5	2 ~ 124	7 ~ 19
${}^7\text{Li}-{}^7\text{Li}$	${}^3\Sigma_u$	64.9097	-17.2	0.643	1006.3	1014.8	0 ~ 17	3 ~ 25
${}^{23}\text{Na}-{}^{23}\text{Na}$	${}^1\Sigma_g$	88.624	34.936	5.705	187.317	187.5	0 ~ 86	4 ~ 20
${}^{23}\text{Na}-{}^{23}\text{Na}$	${}^3\Sigma_u$	88.624	77.286	-1.213	62.3756	62.5	2 ~ 13	16 ~ 24
${}^{133}\text{Cs}-{}^{133}\text{Cs}$	${}^1\Sigma_g$	203.62	68.216	3.365	624.013	624.55	0 ~ 146	7 ~ 45

β_6 . In each case R^b is less than one-third the size of β_6 . Hence one can probe these interactions in a van der Waals effective field theory with cutoff momentum up to roughly three times $1/\beta_6$ without violating the causality bound.

5.8 Causal range near a magnetic Feshbach resonance

In Ref. [74] the multichannel problem of scattering around a magnetic Feshbach resonance is reduced to a description by an effective single-channel K-matrix that depends on the applied magnetic field B . The behavior around the resonance is described by several parameters. $B_{0,\ell}$ is the position of the resonance, while g_{res} parametrizes the width of the Feshbach resonance. K_ℓ^{bg} is a background value for the K-matrix, and the scale $d_{B,\ell}$ is introduced to define a dimensionless

magnetic field. We write the effective single-channel K-matrix as

$$\mathbf{K}_\ell^{\text{eff}}(p, B) = -\mathbf{K}_\ell^{\text{bg}} \left[1 + \frac{g_{\text{res}}}{p^2 \beta_6^2 - g_{\text{res}} (B_s + 1)} \right], \quad (5.41)$$

with

$$B_s = \frac{(B - B_{0,\ell})}{d_{B,\ell}}. \quad (5.42)$$

The parametrization given above corresponds to Eq. (18) in Ref. [74]. Note that we have changed the notation slightly and are using a different sign convention.

By expanding the right-hand side of Eq. (5.41) in p^2 , it is straightforward to determine the K-matrix expansion parameters $K_{\ell,0}$ and $K_{\ell,2}$. A short calculation yields that

$$K_{\ell,0}^{\text{eff}} = -\mathbf{K}_\ell^{\text{bg}} \left(1 + \frac{1}{B_s + 1} \right), \quad (5.43)$$

$$K_{\ell,2}^{\text{eff}} = \frac{\beta_6^2 \mathbf{K}_\ell^{\text{bg}}}{g_{\text{res}} (B_s + 1)^2}. \quad (5.44)$$

As noted in Ref. [74], the parameters $\mathbf{K}_\ell^{\text{bg}}$ and g_{res} are constrained by the condition

$$\mathbf{K}_\ell^{\text{bg}} g_{\text{res}} < 0. \quad (5.45)$$

From this we directly see that $K_{\ell,2}^{\text{eff}}$ given by Eq. (5.44) is always negative. From the causality bound in Eq. (5.29) it follows that where this effective single-channel description is applicable and correctly captures the entire energy dependence of the short-range K-matrix, the causal range will be zero when the interaction is tuned close to a Feshbach resonance.

5.9 Summary and discussion

In this chapter we have analyzed two-body scattering with arbitrary short-range interactions plus an attractive $1/r^6$ tail. We derived the constraints of causality and unitarity for the short-range K-matrix,

$$K_\ell = \tan \delta_\ell^{(\text{short})}(p) = \sum_{n=0}^{\infty} K_{\ell,2n} p^{2n}. \quad (5.46)$$

For any r larger than the range of the short-range interactions, R , we find that $K_{\ell,2}$ satisfies the upper bound

$$K_{\ell,2} \leq b_\ell^{\text{vdW}}(r), \quad (5.47)$$

where $b_\ell^{\text{vdW}}(r)$ is

$$b_\ell^{\text{vdW}}(r) = \frac{\pi}{4} W[f_{\ell,2}, f_{\ell,0}](r) + \frac{\pi}{4} K_{\ell,0}^2 W[g_{\ell,2}, g_{\ell,0}](r) - \frac{\pi}{4} K_{\ell,0} \left\{ W[g_{\ell,2}, f_{\ell,0}](r) + W[f_{\ell,2}, g_{\ell,0}](r) \right\}, \quad (5.48)$$

and the Wronskians are given in Eq. (5.26), Eq. (5.27), and Eq. (5.28).

In clear contrast with the case for only finite-range interactions which was the subject of Chapter 4 or with Coulomb tails [107], the function $b_\ell^{\text{vdW}}(r)$ does not diverge but rather vanishes as $r \rightarrow 0$ for all ℓ . When $K_{\ell,2} \leq 0$, there is no constraint derived from causality and unitarity that prevents the use of an effective field theory with zero-range contact interactions plus an attractive $1/r^6$ tail. This holds true for any angular momentum value ℓ . For the phenomenologically important case of a multichannel system near a magnetic Feshbach resonance, the effective value for $K_{\ell,2}$ is negative and so the short-range interaction can be taken to have zero range.

The van der Waals interaction is qualitatively different from the Coulomb interaction where $b_\ell^{\text{Coulomb}}(r)$ diverges for $\ell \geq 1$. The key difference is that both van der Waals wave functions

F_ℓ and G_ℓ vanish at the origin. This phenomenon also occurs for an attractive $1/r^\alpha$ interaction for $\alpha > 2$ in any number of spatial dimensions. It is also valid for an attractive $1/r^2$ interaction when the coupling constant is strong enough to form bound states. For an effective field theory with contact interactions and attractive singular power-law tail, the cutoff momentum can be made arbitrarily large for any ℓ without producing a divergence in the coefficient $K_{\ell,2}$ of the short-range K matrix.

When $K_{\ell,2}$ is positive, there is a lower bound on the range of the short-range interactions. We define the causal range R^b as this minimum value for the range, given by the condition

$$K_{\ell,2} = b_\ell^{\text{vdW}}(R^b). \quad (5.49)$$

We have analyzed several examples of s -wave scattering in alkali-metal atoms in Table 5.1. We find that the $K_{\ell,2}$ is at least one order of magnitude smaller than β_6^2 . As a result we find that the causal ranges are small in comparison with β_6 .

In summary, we find that β_6 dominates over distance scales parametrizing the short-range interactions. The origin of this van der Waals universality can be explained by two facts. The first fact is the phenomenological observation that, in single-channel scattering between alkali-metal atoms, there is a significant separation between the typical length scales of the short-distance physics and β_6 . This can be seen by the small size of the short-range parameter $K_{\ell,2}$ compared with β_6^2 . As Gao has shown, this also leads to the approximate universal relation that $K_{\ell,0}$ is the same for all ℓ [77]. Therefore, to a good approximation, β_6 and the s -wave scattering length will determine the threshold scattering behavior for all values of ℓ . For the multichannel case near a magnetic Feshbach resonance, we find that the effective $K_{\ell,2}^{\text{eff}}$ is no longer negligible. However, $K_{\ell,2}^{\text{eff}}$ is negative, and this means that there is no constraint from causality preventing the zero-range limit for the short-distance interactions.

The second fact underlying the van der Waals universality is that the zero-range limit of short-distance interactions is well behaved with regard to scattering near threshold. We note, however, that there is still no scale-invariant limit for $\ell \geq 1$ since the effective range parameter will diverge to negative infinity as β_6 goes to zero. This can be seen from the $\beta_6^{-2\ell+1}$ behavior with negative coefficient for $\ell \geq 1$ in Eq. (5.38).

The analysis in this study should be useful in developing an effective field theory with an attractive $1/r^6$ tail and contact interactions. Similarly, one can also construct effective field theories for other attractive singular potentials $1/r^\alpha$ for $\alpha \geq 2$. These effective field theories could be used to investigate the Efimov effect and other low-energy phenomena in a model-independent way.

Impurity Lattice Monte Carlo and the Adiabatic Projection Method

6.1 Introduction

The adiabatic projection method is a general framework for calculating scattering and reactions on the lattice. The method constructs a low-energy effective theory for clusters which becomes exact in the limit of large Euclidean projection time. Previous studies of this method [154, 143] have used exact sparse matrix methods. In this work we demonstrate the first application using Monte Carlo simulations. As we will show, the adiabatic projection method significantly improves the accurate calculation of finite-volume energy levels. As we also will show, the finite-volume energy levels must be calculated with considerable accuracy in order to determine the scattering phase shifts using Lüscher's method. We give a short summary of Lüscher's method later in our discussion.

The goal of this analysis is to benchmark the use of lattice Monte Carlo simulations with the adiabatic projection method. The example we consider in detail is fermion-dimer scattering

for two-component fermions and zero-range interactions. Our calculation also corresponds to neutron-deuteron scattering in the spin-quartet channel at leading order in pionless effective field theory. In our interacting system there are two components for the fermions. We call the two components up and down spins, \uparrow and \downarrow . The bound dimer state is composed of one \uparrow and one \downarrow , and our fermion-dimer system consists of two \uparrow and one \downarrow . While s -wave scattering has been considered previously [28, 26, 148, 143], we will present the first lattice calculations of p -wave and d -wave fermion-dimer scattering.

As discussed in Ref. [143], the adiabatic projection method starts with a set of initial cluster states. By clusters we mean either a single particle or a bound state of several particles. In our analysis here we consider fermion-dimer elastic scattering where there are two clusters. In Ref. [143], the initial fermion-dimer states were parameterized by the initial spatial separation between clusters, \vec{R} . The initial cluster states can be written explicitly as

$$|\vec{R}\rangle = \sum_{\vec{n}} b_{\uparrow}^{\dagger}(\vec{n}) b_{\downarrow}^{\dagger}(\vec{n}) b_{\uparrow}^{\dagger}(\vec{n} + \vec{R}) |0\rangle, \quad (6.1)$$

where the spatial volume is a periodic cubic box of length L in lattice units. The initial states are then projected using Euclidean time to form dressed cluster states,

$$|\vec{R}\rangle_t = e^{-\hat{H}t} |\vec{R}\rangle. \quad (6.2)$$

The adiabatic method uses these dressed cluster states to calculate matrix elements of the Hamiltonian and other observables. The result is a low-energy effective theory of interacting clusters which becomes systematically more accurate as the projection time t is increased. An estimate of the residual error is derived in Ref. [143].

For our calculations here we follow the same general process except that we build the initial

cluster states in a different manner. Instead of working with the relative separation between clusters, we work with the relative momentum between the clusters. We find that this change improves the efficiency of the Monte Carlo calculation by reducing the number of required initial states. The new technique involves first constructing a dimer state with momentum \vec{p} using Euclidean time projection and then multiplying by a creation operator for a second \uparrow particle with momentum $-\vec{p}$. For example, we can write the initial fermion-dimer state explicitly as

$$|\vec{p}\rangle = \tilde{b}_{\uparrow}^{\dagger}(-\vec{p})e^{-\hat{H}t'}\tilde{b}_{\uparrow}^{\dagger}(\vec{p})\tilde{b}_{\downarrow}^{\dagger}(\vec{0})|0\rangle. \quad (6.3)$$

From these states we produce dressed cluster states by Euclidean time projection,

$$|\vec{p}\rangle_t = e^{-\hat{H}t/2}|\vec{p}\rangle. \quad (6.4)$$

We then proceed in the same manner as in Ref. [143] and calculate the matrix elements of the Hamiltonian in the basis of the dressed cluster states.

For our Monte Carlo simulations we introduce a new algorithm which we call the impurity lattice Monte Carlo algorithm. Credit for developing this algorithm is to be shared with Ref. [27], where applications to impurities in many-body systems are being investigated using the same method. It can be viewed as a hybrid algorithm in between worldline and auxiliary-field Monte Carlo simulations. In worldline algorithms, the quantum amplitude is calculated by sampling particle worldlines in Euclidean spacetime. In auxiliary-field Monte Carlo simulations, the interactions are recast as single particle interactions, and the quantum amplitude is computed exactly for each auxiliary field configuration. In impurity Monte Carlo, we handle the impurities using worldline Monte Carlo simulations while all other particles are treated using the auxiliary-field formalism. Furthermore, the impurity worldlines themselves are acting as additional auxiliary fields felt by other particles in the system. We have found that for our system of two \uparrow

and one \downarrow particles, impurity lattice Monte Carlo method is computationally superior to other methods such as the auxiliary-field Monte Carlo due to its speed and efficiency as well as control over sign oscillations. We will derive the formalism of impurity Monte Carlo simulations in detail in our discussion here.

The organization of this chapter is as follows. We first start with the basic continuum and lattice formulations of our interacting system with zero-range two-component fermions. We then take a short detour to derive the connection between normal-ordered transfer matrices and lattice Grassmann actions. Using our dictionary between lattice Grassmann actions and quantum operators, we derive the transfer matrix induced by a given single impurity worldline. We then describe the implementation of the adiabatic projection method and the details of our Monte Carlo simulations for computing finite-volume energy levels.

In order to determine scattering phase shifts, we then discuss Lüscher's finite-volume method. As part of this discussion we discuss for the first time, the character of topological volume corrections for fermion-dimer scattering in the p -wave and d -wave channels. By topological volume corrections, we are specifically referring to momentum-dependent finite-volume corrections of the dimer binding energy [28, 45]. Previous studies looking at topological volume corrections had only considered s -wave scattering [28, 26, 148, 143]. The extension to higher partial waves is given in the appendix. We then conclude with a comparison of Monte Carlo results as well as exact lattice calculations and continuum calculations.

6.2 Lattice Hamiltonian

We consider a three-body system of two-component fermions with equal mass, $m_{\uparrow} = m_{\downarrow} = m$. We consider the limit of large scattering length between the two components where the interaction range of the fermions is taken to be negligible. We start with the free non-relativistic

Hamiltonian,

$$\hat{H}_0 = \frac{1}{2m} \sum_{s=\uparrow,\downarrow} \int d^3\vec{r} \vec{\nabla} b_s^\dagger(\vec{r}) \cdot \vec{\nabla} b_s(\vec{r}), \quad (6.5)$$

In the low-energy limit the interaction can be simplified as a delta-function interaction between the two spin components,

$$\hat{H} = \frac{1}{2m} \sum_{s=\uparrow,\downarrow} \int d^3\vec{r} \vec{\nabla} b_s^\dagger(\vec{r}) \cdot \vec{\nabla} b_s(\vec{r}) + C_0 \int d^3\vec{r} \hat{\rho}_\uparrow(\vec{r}) \hat{\rho}_\downarrow(\vec{r}), \quad (6.6)$$

where $\hat{\rho}_{\uparrow,\downarrow}(\vec{r})$ are density operators,

$$\hat{\rho}_\uparrow(\vec{r}) = b_\uparrow^\dagger(\vec{r}) b_\uparrow(\vec{r}), \quad (6.7)$$

$$\hat{\rho}_\downarrow(\vec{r}) = b_\downarrow^\dagger(\vec{r}) b_\downarrow(\vec{r}). \quad (6.8)$$

The ultraviolet physics of this zero-range interaction must be regulated in some manner. In our case the lattice provides the needed regularization. We denote the spatial lattice spacing as a and the temporal lattice spacing as a_t . We will write all quantities in lattice units, which are physical units multiplied by the corresponding power of a to render the combination dimensionless. We use the free non-relativistic lattice Hamiltonian defined in Eqs. (3.42) and (3.43) and the contact interaction potential is

$$\hat{V} = C_0 \sum_{\vec{n}} \hat{\rho}_\uparrow(\vec{n}) \hat{\rho}_\downarrow(\vec{n}). \quad (6.9)$$

Here \hat{l} denotes a lattice unit vector in one of the spatial directions, $\hat{l} = \hat{1}, \hat{2}, \hat{3}$. The unknown interaction coefficient C_0 is tuned to reproduce the desired binding energy of the dimer at infinite volume.

6.3 Lattice path integrals and transfer matrices

For our Monte Carlo simulations and exact lattice calculations we use the transfer matrix formalism introduced in Chapter 3. It is convenient to collect some of the important formulas given in Chapter 3. As it is already discussed, the Grassmann path integral has the form

$$\mathcal{Z} = \int \left[\prod_{n_t, \vec{n}, s=\uparrow, \downarrow} d\theta_s^*(n_t, \vec{n}) d\theta_s(n_t, \vec{n}) \right] e^{-S[\theta, \theta^*]}, \quad (6.10)$$

where $S[\theta, \theta^*]$ is the non-relativistic lattice action and defined in Section 3.4, and θ_s^* and θ_s are anti-commuting Grassmann variables. Our lattice action can be decomposed into three parts.

While the Grassmann formalism is convenient for deriving the lattice Feynman rules, the transfer matrix formalism is more convenient for numerical calculations. Therefore, we make the connection between the two formulations, and we use the following exact relation between the Grassmann path integral formula and the transfer matrix formalism [43, 44]. For any function f ,

$$\begin{aligned} & \text{Tr} \left[: f_{L_t-1}[a_{s'}^\dagger(\vec{n}'), a_s(\vec{n})] : \cdots : f_0[a_{s'}^\dagger(\vec{n}'), a_s(\vec{n})] : \right] \\ &= \int \left[\prod_{n_t, \vec{n}, s=\uparrow, \downarrow} d\theta_s^*(n_t, \vec{n}) d\theta_s(n_t, \vec{n}) \right] e^{-\sum_{n_t} S_t[\theta, \theta^*, n_t]} \prod_{n_t=0}^{L_t-1} f_{n_t}[\theta_{s'}^*(n_t, \vec{n}'), \theta_s(n_t, \vec{n})], \quad (6.11) \end{aligned}$$

where the symbol $::$ signifies normal ordering. Normal ordering rearranges all operators so that all annihilation operators are moved to the right and creation operators are moved to the left with the appropriate number of anticommutation minus signs. Then the desired transfer matrix formulation of the path integral is

$$\mathcal{Z} = \text{Tr} [\hat{M}^{L_t}], \quad (6.12)$$

where \hat{M} is the normal-ordered transfer matrix operator,

$$\hat{M} =: \exp \left[-\alpha_t \hat{H}_0 - \alpha_t C_0 \sum_{\vec{n}} \hat{\rho}_{\uparrow}(\vec{n}) \hat{\rho}_{\downarrow}(\vec{n}) \right] : . \quad (6.13)$$

Here \hat{H}_0 is the free lattice Hamiltonian given in Eq. (3.42).

6.4 Impurity Lattice Monte Carlo: Single Impurity

In this section we derive the formalism for impurity lattice Monte Carlo for a single impurity. In impurity Monte Carlo the impurities are treated differently from other particles. The assumption is that there are only a small number of impurities and these can be sampled using worldline Monte Carlo without strong fermion sign oscillation problems from antisymmetrization. In our case there is exactly one \downarrow particle, and we treat this as a single impurity for our system.

Let us consider the occupation number basis,

$$|\chi_{n_t}^{\uparrow}, \chi_{n_t}^{\downarrow}\rangle = \prod_{\vec{n}} \left\{ \left[b_{\uparrow}^{\dagger}(\vec{n}) \right]^{\chi_{n_t}^{\uparrow}(\vec{n})} \left[b_{\downarrow}^{\dagger}(\vec{n}) \right]^{\chi_{n_t}^{\downarrow}(\vec{n})} \right\} |0\rangle \quad (6.14)$$

where $\chi_{n_t}^s(\vec{n})$ counts the occupation number on each lattice site at time step n_t and has values which are either 0 or 1. Let us define the Grassmann functions,

$$X(n_t) = \prod_{\vec{n}} \left[e^{\theta_{\uparrow}^*(n_t, \vec{n}) \theta_{\uparrow}(n_t, \vec{n})} e^{\theta_{\downarrow}^*(n_t, \vec{n}) \theta_{\downarrow}(n_t, \vec{n})} \right], \quad (6.15)$$

and

$$M(n_t) = e^{-S_{H_0}[\theta, \theta^*, n_t]} e^{-S_V[\theta, \theta^*, n_t]}. \quad (6.16)$$

The transfer matrix element between time steps n_t and $n_t + 1$ can be written in terms of these

lattice Grassmann functions as

$$\begin{aligned}
& \langle \chi_{n_t+1}^\uparrow, \chi_{n_t+1}^\downarrow | \hat{M} | \chi_{n_t}^\uparrow, \chi_{n_t}^\downarrow \rangle \\
&= \prod_{\vec{n}} \left\{ \left[\frac{\vec{\partial}}{\partial \theta_{\downarrow}^*(n_t, \vec{n})} \right] \chi_{n_t+1}^\downarrow(\vec{n}) \left[\frac{\vec{\partial}}{\partial \theta_{\uparrow}^*(n_t, \vec{n})} \right] \chi_{n_t+1}^\uparrow(\vec{n}) \right\} X(n_t) M(n_t) \\
&\times \prod_{\vec{n}'} \left\{ \left[\frac{\overleftarrow{\partial}}{\partial \theta_{\uparrow}(n_t, \vec{n}')} \right] \chi_{n_t}^\uparrow(\vec{n}') \left[\frac{\overleftarrow{\partial}}{\partial \theta_{\downarrow}(n_t, \vec{n}')} \right] \chi_{n_t}^\downarrow(\vec{n}') \right\} \Big|_{\substack{\theta_{\uparrow}' = \theta_{\downarrow}' = 0 \\ \theta_{\uparrow} = \theta_{\downarrow} = 0}}. \tag{6.17}
\end{aligned}$$

This result can be verified by checking the different possible combinations for the occupation numbers. Since we have only one \downarrow particle, the right hand side is nonzero only if

$$\sum_{\vec{n}} \chi_{n_t}^\downarrow(\vec{n}) = \sum_{\vec{n}} \chi_{n_t+1}^\downarrow(\vec{n}) = 1. \tag{6.18}$$

We now derive the transfer matrix formalism for one spin- \downarrow particle worldline in a medium consisting of an arbitrary number of spin- \uparrow particles. The impurity worldline is to be considered fixed. To provide a simple visual representation of the worldline, we draw in Figure 6.1 an example of a single-particle worldline configuration on a 1+1 dimensional Euclidean lattice.

We now remove or “integrate out” the impurity particle from the lattice action. We consider first the case when the \downarrow particle hops from \vec{n}'' to some nearest neighbor site. In other words, $\chi_{n_t}^\downarrow(\vec{n}'') = 1$ and $\chi_{n_t+1}^\downarrow(\vec{n}'' \pm \hat{l}) = 1$ for some unit vector \hat{l} . In this case we have

$$\begin{aligned}
& \langle \chi_{n_t+1}^\uparrow, \chi_{n_t+1}^\downarrow | \hat{M} | \chi_{n_t}^\uparrow, \chi_{n_t}^\downarrow \rangle \\
&= \prod_{\vec{n}} \left\{ \left[\frac{\vec{\partial}}{\partial \theta_{\uparrow}^*(n_t, \vec{n})} \right] \chi_{n_t+1}^\uparrow(\vec{n}) \right\} X(n_t) M_{\vec{n}'' \pm \hat{l}, \vec{n}''}(n_t) \prod_{\vec{n}'} \left\{ \left[\frac{\overleftarrow{\partial}}{\partial \theta_{\uparrow}(n_t, \vec{n}')} \right] \chi_{n_t}^\uparrow(\vec{n}') \right\} \Big|_{\substack{\theta_{\uparrow}' = 0 \\ \theta_{\downarrow}' = 0}}, \tag{6.19}
\end{aligned}$$

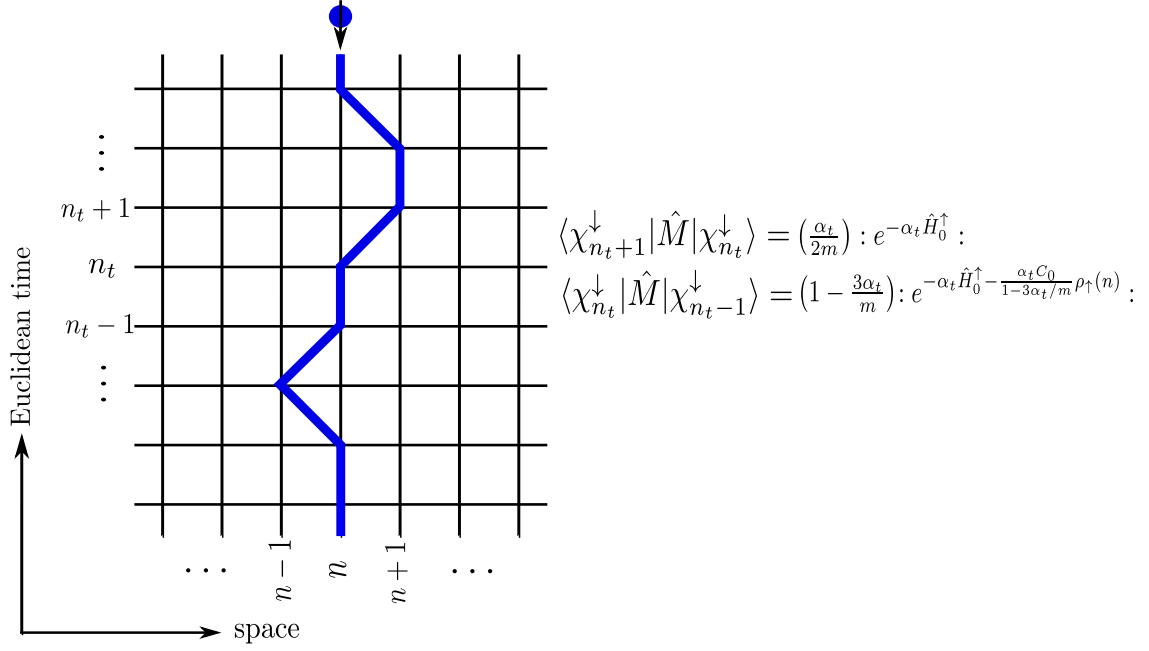


Figure 6.1 A segment of a worldline configuration on a 1+1 dimensional Euclidean lattice. See the main text for derivations of the reduced transfer-matrix operators.

where

$$\mathcal{X}(n_t) = \prod_{\vec{n}} \left[e^{\theta_\uparrow^*(n_t, \vec{n}) \theta_\uparrow(n_t, \vec{n})} \right], \quad (6.20)$$

and

$$M_{\vec{n}'' \pm \hat{l}, \vec{n}''}(n_t) = \left(\frac{\alpha_t}{2m}\right) \exp \left\{ -\alpha_t H_0^\dagger[\theta_s, \theta_s^*, n_t] \right\}. \quad (6.21)$$

Next we consider the case when $\chi_{n_t}^\downarrow(\vec{n}'') = 1$ and $\chi_{n_t+1}^\downarrow(\vec{n}'') = 1$ which corresponds to no spatial

hopping of the impurity worldline. Then we have

$$\begin{aligned} & \langle \chi_{n_t+1}^\uparrow, \chi_{n_t+1}^\downarrow | \hat{M} | \chi_{n_t}^\uparrow, \chi_{n_t}^\downarrow \rangle \\ &= \prod_{\vec{n}} \left\{ \left[\frac{\vec{\partial}}{\partial \theta_\uparrow^*(n_t, \vec{n})} \right]^{\chi_{n_t}^\uparrow(\vec{n})} \right\} \mathcal{X}(n_t) \hat{M}_{\vec{n}'', \vec{n}''}(n_t) \prod_{\vec{n}'} \left\{ \left[\frac{\overleftarrow{\partial}}{\partial \theta_\uparrow(n_t, \vec{n}') } \right]^{\chi_{n_t}^\uparrow(\vec{n}')} \right\} \Bigg|_{\substack{\theta_\uparrow' = 0 \\ \theta_\uparrow = 0}}, \end{aligned} \quad (6.22)$$

where

$$\hat{M}_{\vec{n}'', \vec{n}''}(n_t) = \left(1 - \frac{3\alpha_t}{m} \right) \exp \left\{ -\alpha_t H_0^\uparrow[\theta_s, \theta_s^*, n_t] - \frac{\alpha_t C_0}{1 - \frac{3\alpha_t}{m}} \theta_\uparrow^*(n_t, \vec{n}'') \theta_\uparrow(n_t, \vec{n}'') \right\}. \quad (6.23)$$

From these Grassmann lattice actions with the impurity integrated out, we can write down the corresponding transfer matrix operators. When the impurity makes a spatial hop, the reduced transfer-matrix operator is

$$\hat{M}_{\vec{n}'' \pm \hat{i}, \vec{n}''} = \left(\frac{\alpha_t}{2m} \right) : \exp \left[-\alpha_t \hat{H}_0^\uparrow \right] :. \quad (6.24)$$

When the impurity worldline remains stationary the reduced transfer-matrix operator is

$$\hat{M}_{\vec{n}'', \vec{n}''} = \left(1 - \frac{3\alpha_t}{m} \right) : \exp \left[-\alpha_t \hat{H}_0^\uparrow - \frac{\alpha_t C_0}{1 - \frac{3\alpha_t}{m}} \rho_\uparrow(\vec{n}'') \right] :. \quad (6.25)$$

We note that these reduced transfer matrices are just one-body operators on the linear space of \uparrow particles.

6.5 Adiabatic Projection Method

In this section we describe our application of the adiabatic projection method using a set of cluster states constructed in momentum space. As already described in Eq. (6.3) in a simplified notation, we let $|\Psi_{\vec{p}}\rangle$ be the fermion-dimer initial state with relative momentum \vec{p} ,

$$|\Psi_{\vec{p}}\rangle = \tilde{b}_{\uparrow}^{\dagger}(-\vec{p})\hat{M}^{L_t}\tilde{b}_{\uparrow}^{\dagger}(\vec{p})\tilde{b}_{\downarrow}^{\dagger}(\vec{0})|0\rangle, \quad (6.26)$$

where we use the transfer matrix operator \hat{M} given in Eq. (6.13) for some number of time steps L_t . The purpose of this time propagation is to allow the dimer to bind its constituents before injecting an additional \uparrow particle. In this part of the calculation we in fact increase the attractive interactions between the two spins to allow them to form the bound dimer faster. We find that this trick increases the computational efficiency on large lattice systems. The dressed cluster states are defined as

$$|\Psi_{\vec{p}}\rangle_{L_t/2} = \hat{M}^{L_t/2}|\Psi_{\vec{p}}\rangle, \quad (6.27)$$

for some even number L_t , and the overlap between dressed cluster states is

$$Z_{\vec{p}\vec{p}'}(L_t) = \langle\Psi_{\vec{p}}|\hat{M}^{L_t}|\Psi_{\vec{p}'}\rangle. \quad (6.28)$$

For large L_t we can obtain an accurate representation of the low-energy spectrum of \hat{M} by defining the adiabatic transfer matrix as

$$[\hat{M}^a(L_t)]_{\vec{p}\vec{p}'} = \sum_{\vec{p}''} Z_{\vec{p}\vec{p}''}^{-1}(L_t) Z_{\vec{p}''\vec{p}'}(L_t + 1). \quad (6.29)$$

Alternatively we can also construct a symmetric version of the adiabatic transfer matrix as

$$[\hat{M}^a(L_t)]_{\vec{p}\vec{p}'} = \sum_{\vec{p}'', \vec{p}'''} Z_{\vec{p}\vec{p}''}^{-1/2}(L_t) Z_{\vec{p}''\vec{p}'''}(L_t + 1) Z_{\vec{p}'''\vec{p}'}^{-1/2}(L_t). \quad (6.30)$$

Either form will produce exactly the same spectrum. As with any transfer matrix, we interpret the eigenvalues $\lambda_i(L_t)$ of the adiabatic transfer matrix as energies using the relations

$$e^{-E_i(L_t)\alpha_t} = \lambda_i(L_t), \quad E_i(L_t) = -\alpha_t^{-1} \log \lambda_i(L_t). \quad (6.31)$$

The exact low-energy eigenvalues of the full transfer matrix \hat{M} will be recovered in the limit $L_t \rightarrow \infty$.

As a special case, one can simply restrict the adiabatic projection calculation to a single initial momentum state, for example, $\vec{p} = 0$. In that case the adiabatic transfer matrix is just the scalar ratio

$$Z_{\vec{p}\vec{p}}(L_t + 1)/Z_{\vec{p}\vec{p}}(L_t). \quad (6.32)$$

However we find that the energy calculations are significantly more accurate and converge much faster with increasing L_t when using a set of several initial cluster states.

6.6 Impurity Monte Carlo Simulation

The reduced transfer matrices $\hat{M}_{\vec{n}, \vec{n}'}$ in Eq. (6.24) and (6.25) are one-body operators on the linear space of \uparrow particles. Therefore we can simply multiply the reduced transfer matrices together. It is perhaps worthwhile to note that the \vec{n}, \vec{n}' subscripts are not the matrix indices of the reduced transfer matrix, but rather the coordinates of the \downarrow particle that was integrated out. The matrix indices of $\hat{M}_{\vec{n}, \vec{n}'}$ are being left implicit.

The Euclidean time projection can be written as a sum over worldline configurations of the \downarrow particle. As a convenient shorthand we write

$$\hat{M}_{\{\vec{n}_j\}}^{[L_t]} = \hat{M}_{\vec{n}_{L_t}, \vec{n}_{L_t-1}} \cdots \hat{M}_{\vec{n}_1, \vec{n}_0}, \quad (6.33)$$

where \vec{n}_j denotes the spatial position of the spin- \downarrow particle at time step j . The projection amplitude for cluster states $|\Psi_{\vec{p}}\rangle$ and $|\Psi_{\vec{p}'}\rangle$ is then

$$Z_{\vec{p}\vec{p}'}(L_t) = \sum_{\vec{n}_0, \dots, \vec{n}_{L_t}} \langle \Psi_{\vec{p}} | \hat{M}_{\{\vec{n}_j\}}^{[L_t]} | \Psi_{\vec{p}'} \rangle. \quad (6.34)$$

The states $|\Psi_{\vec{p}}\rangle$ and $|\Psi_{\vec{p}'}\rangle$ defined in Eq. (6.26) are constructed using single particle creation operators, and so the amplitude $Z_{\vec{p}\vec{p}'}(L_t)$ is just the determinant of a 2×2 matrix of single-particle amplitudes. As seen in Eq. (6.26), there are an extra L_t' projection steps in between some of the creation operators. This gives us the following structure,

$$Z_{\vec{p}\vec{p}'}(L_t) = \sum_{\vec{n}_0, \dots, \vec{n}_{L_t}} \sum_{\vec{n}'_0, \dots, \vec{n}'_{L_t'}} \sum_{\vec{n}''_0, \dots, \vec{n}''_{L_t''}} \det M_{2 \times 2}, \quad (6.35)$$

where $\vec{n}''_0 = \vec{n}_{L_t}$, $\vec{n}'_{L_t'} = \vec{n}_0$, and

$$M_{2 \times 2} = \begin{bmatrix} \langle \vec{p} | \hat{M}_{\{\vec{n}''_j\}}^{[L_t']} \hat{M}_{\{\vec{n}_j\}}^{[L_t]} \hat{M}_{\{\vec{n}'_j\}}^{[L_t']} | \vec{p}' \rangle & \langle \vec{p} | \hat{M}_{\{\vec{n}''_j\}}^{[L_t']} \hat{M}_{\{\vec{n}_j\}}^{[L_t]} | -\vec{p}' \rangle \\ \langle -\vec{p} | \hat{M}_{\{\vec{n}_j\}}^{[L_t]} \hat{M}_{\{\vec{n}'_j\}}^{[L_t']} | \vec{p}' \rangle & \langle -\vec{p} | \hat{M}_{\{\vec{n}_j\}}^{[L_t]} | -\vec{p}' \rangle \end{bmatrix}. \quad (6.36)$$

The calculation of $Z_{\vec{p}\vec{p}'}(L_t)$ has now been recast as a problem of computing the determinant of the matrix $M_{2 \times 2}$ over all possible impurity worldlines. We use a Markov chain Monte Carlo process to select worldline configurations. The Metropolis algorithm is used to accept or reject configurations with importance sampling given by the weight function $|Z_{\vec{p}\vec{p}'}(L_t)|$, where \vec{p} is one

of the initial momenta.

We now benchmark our results for the low-energy spectrum calculated using adiabatic projection and the impurity Monte Carlo method. We compare with exact lattice results computed using the Lanczos iterative eigenvector method with a space of $\sim L^6$ basis states. Although exact lattice results provide a useful benchmark test for the three-particle system, the extension to larger systems is computationally not viable due to exponential scaling in memory and CPU time. In contrast, the impurity Monte Carlo calculation does scale well to much larger systems. In fact, many-body impurity systems are currently being studied in Ref. [27].

Table 6.1 Momentum of the dimer, \vec{p}_d , with $p = 2\pi/L$. The total momentum of the system is zero.

n	\vec{p}_d
1	$\langle p, 0, 0 \rangle$
2	$\langle 0, p, 0 \rangle$
3	$\langle 0, 0, p \rangle$
4	$\langle p, -p, 0 \rangle$
5	$\langle p, 0, -p \rangle$
6	$\langle 0, p, -p \rangle$

In our lattice calculations we take the particle mass to be the average nucleon mass, 938.92 MeV, and the interaction strength C_0 is tuned to obtain the deuteron energy, -2.2246 MeV. We use an L^3 periodic cubic volume with spatial lattice spacing $a = 1.97$ fm. The values of L used will be specified later. In the temporal direction we use L_t time steps with a temporal lattice spacing $a_t = 1.31$ fm/c.

Let N be the number of initial/final states. We choose the initial dimer momenta, \vec{p}_d , as shown in Table 6.1. In all cases the total momentum of the three-particle system is set to zero. We label and order the various possible dimer momenta with index $n = 1, \dots, N$. We then construct the corresponding $N \times N$ adiabatic matrix, $[\hat{M}^a(L_t)]_{nn'}$, and obtain the N low-lying energy states

of the finite-volume system. There is no restriction on the choice of N . Therefore, so long as the numerical stability of the matrix calculations is under control, it is advantageous to maximize the number N . While constructing a large adiabatic matrix requires more computational time, it significantly accelerates the convergence with the number of projection time steps, L_t .

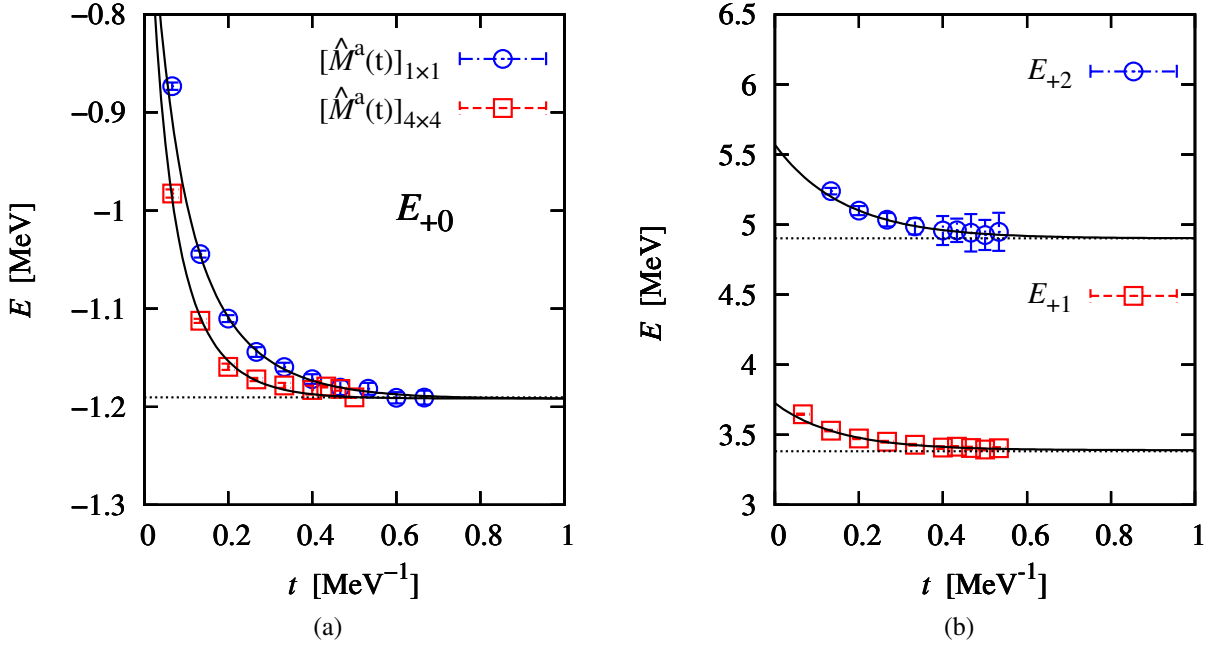


Figure 6.2 The ground state energy is shown versus projection time t using either one or four initial/final states in Panel (a) and the first two excited state energies with even parity in Panel (b). For comparison we show the exact lattice energies as dotted horizontal lines.

In Fig. 6.2(a) we compare the ground state energies using $[\hat{M}^a(t)]_{1 \times 1}$ and $[\hat{M}^a(t)]_{4 \times 4}$ adiabatic matrices. We are plotting the energies versus projection time $t = L_t a_t$. The results shown are obtained using a lattice box of length $La = 13.79$ fm, while the number of time steps is varied over a range of values to extrapolate to the limit $t \rightarrow \infty$. We use a simple exponential

ansatz to extrapolate away the residual contribution from higher-energy states,

$$E_i(t) = E_i(\infty) + c_i e^{-\Delta E_i t} + \dots \quad (6.37)$$

As can be seen clearly in the figure, the $[\hat{M}^a(t)]_{4 \times 4}$ results converge with a significantly faster exponential decay than the $[\hat{M}^a(t)]_{1 \times 1}$ results. This is consistent with the derivation in Ref. [143] that the energy gap ΔE_i in Eq. (6.37) is increased by including more initial states. The corresponding extrapolated ground state energies obtained from the $[\hat{M}^a(t)]_{1 \times 1}$ and $[\hat{M}^a(t)]_{4 \times 4}$ adiabatic matrices are $-1.1918(46)$ MeV and $-1.1916(25)$ MeV, respectively.

Table 6.2 The exact and Monte Carlo results for the ground state and lowest lying even-parity energies in a periodic box of length $La = 13.79$ fm. The Monte Carlo results are obtained from the $[\hat{M}^a(t)]_{4 \times 4}$ adiabatic matrix.

	E_{+0} [MeV]	E_{+1} [MeV]	E_{+2} [MeV]
Exact	-1.1904	3.3828	4.9024
MC	-1.1916(25)	3.3905(82)	4.9012(15)

In Figs. 6.2(a) and (b) we plot the lowest lying even-parity energies as a function of Euclidean projection time t . To be able to calculate the two excited states in Fig. 6.2(b) we use seven initial/final states and construct a 7×7 adiabatic matrix. We then use symmetry under cubic rotations to reduce the 7×7 adiabatic matrix to a 4×4 adiabatic matrix. For comparison the horizontal dotted lines in the plots represent the exact lattice energies obtained from the Lanczos iteration method. The solid lines are exponential fits to the data using the ansatz in Eq. (6.37). As seen from Fig. 6.2 and the corresponding extrapolated energies in Table 6.2, we find that the calculations using adiabatic projection with impurity Monte Carlo are in excellent agreement with the exact lattice results.

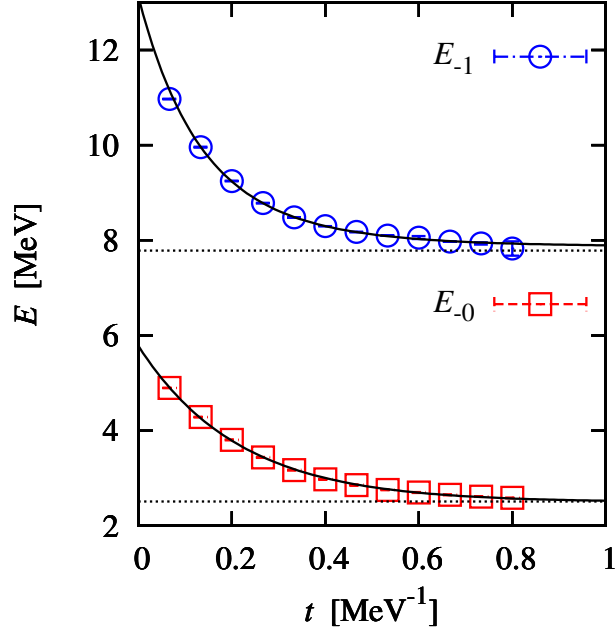


Figure 6.3 The lowest two odd parity energies as a function of Euclidean projection time t . For comparison we show the exact lattice energies as dotted horizontal lines.

In Fig. 6.3 we present the energies for the lowest two states with odd parity. In order to calculate these odd parity energies we use five initial/final states and construct a 5×5 adiabatic matrix. The horizontal dotted lines represent the exact lattice energies obtain from Lanczos iteration, and the solid lines are the exponential extrapolation fits. We see from Fig. 6.3 and Table 6.3 again that the calculations using adiabatic projection with impurity Monte Carlo are in excellent agreement with the exact lattice results. Both energy levels shown in Fig. 6.3 have three-fold degeneracy. The degeneracies of these energy levels are not shown here.

6.7 Composite particles in finite volume

In this section we present lattice results for the fermion-dimer elastic scattering phase shifts for angular momentum up to $\ell = 2$ using Lüscher's finite-volume method. As background

Table 6.3 The exact and Monte Carlo results for the energies of the lowest two odd-parity states in a periodic box of length $La = 13.79$ fm. The Monte Carlo results are obtained from the $[\hat{M}^a(t)]_{5 \times 5}$ adiabatic matrix.

	E_{-0} [MeV]	E_{-1} [MeV]
Exact	2.509	7.784
MC	2.519(25)	7.869(93)

for explaining the finite-volume calculations, we first briefly review Lüscher's method for the s -wave scattering of two particles in Section 3.5.2. In the following, we extend the previous discussion to higher partial waves $\ell \leq 2$. Since the phase shifts depend crucially on an accurate calculation and analysis of finite-volume energy levels, we also discuss in the appendix some corrections which are due to modifications of the dimer binding energy at finite volume.

6.7.1 Lüscher's finite-volume method

Lüscher [122, 124] is a well-known technique for extracting elastic phase shifts for two-body scattering from the volume dependence of two-body continuum states in a cubic periodic box. Lüscher's relation between scattering phase shifts and two-body energy levels in a cubic periodic box has the following forms [122, 124, 125]

$$p^{2\ell+1} \cot \delta_\ell(p) = \begin{cases} \frac{2}{\sqrt{\pi L}} \mathcal{Z}_{0,0}(1; \eta) & \text{for } \ell = 0, \\ \left(\frac{2\pi}{L}\right)^3 \frac{\eta}{\pi^{3/2}} \mathcal{Z}_{0,0}(1; \eta) & \text{for } \ell = 1, \\ \left(\frac{2\pi}{L}\right)^5 \frac{1}{\pi^{3/2}} \left[\eta^2 \mathcal{Z}_{0,0}(1; \eta) + \frac{6}{7} \mathcal{Z}_{4,0}(1; \eta) \right] & \text{for } \ell = 2. \end{cases} \quad (6.38)$$

where

$$\eta = \left(\frac{Lp}{2\pi} \right)^2. \quad (6.39)$$

Here $\mathcal{Z}_{\ell,m}(1; \eta)$ are the generalized zeta functions [122, 124],

$$\mathcal{Z}_{\ell,m}(1; \eta) = \sum_{\vec{n}} \frac{|\vec{n}|^\ell Y_{\ell,m}(\hat{n})}{|\vec{n}|^2 - \eta}, \quad (6.40)$$

and $Y_{\ell,m}(\hat{n})$ are the spherical harmonics. We can evaluate the zeta functions using exponentially-accelerated expressions [125]. For $\ell, m = 0$ we have

$$\begin{aligned} \mathcal{Z}_{0,0}(1; \eta) &= \pi e^\eta (2\eta - 1) + \frac{e^\eta}{2\sqrt{\pi}} \sum_{\vec{n}} \frac{e^{-|\vec{n}|^2}}{|\vec{n}|^2 - \eta} \\ &\quad - \frac{\pi}{2} \int_0^1 d\lambda \frac{e^{\lambda\eta}}{\lambda^{3/2}} \left(4\lambda^2 \eta^2 - \sum_{\vec{n}} e^{-\pi^2 |\vec{n}|^2 / \lambda} \right), \end{aligned} \quad (6.41)$$

and for arbitrary ℓ and m ,

$$\begin{aligned} \mathcal{Z}_{\ell,m}(1; \eta) &= \sum_{\vec{n}} \frac{|\vec{n}|^\ell Y_{\ell,m}(\hat{n})}{|\vec{n}|^2 - \eta} e^{-\Lambda(|\vec{n}|^2 - \eta)} \\ &\quad + \int_0^\Lambda d\lambda \left(\frac{\pi}{\lambda} \right)^{\ell+3/2} e^{\lambda\eta} \sum_{\vec{n}} \frac{|\vec{n}|^\ell Y_{\ell,m}(\hat{n})}{|\vec{n}|^2 - \eta} e^{-\pi^2 |\vec{n}|^2 / \lambda}. \end{aligned} \quad (6.42)$$

6.7.2 Results for the elastic phase shifts

We now use our lattice results for the finite-volume energies and use Eq. (6.38) to determine the elastic phase shifts. We compute phase shifts using data from the impurity Monte Carlo calculations as well as the exact lattice energies using the Lanczos method. The fermion-dimer system that we are considering corresponds exactly to neutron-deuteron scattering in the spin-

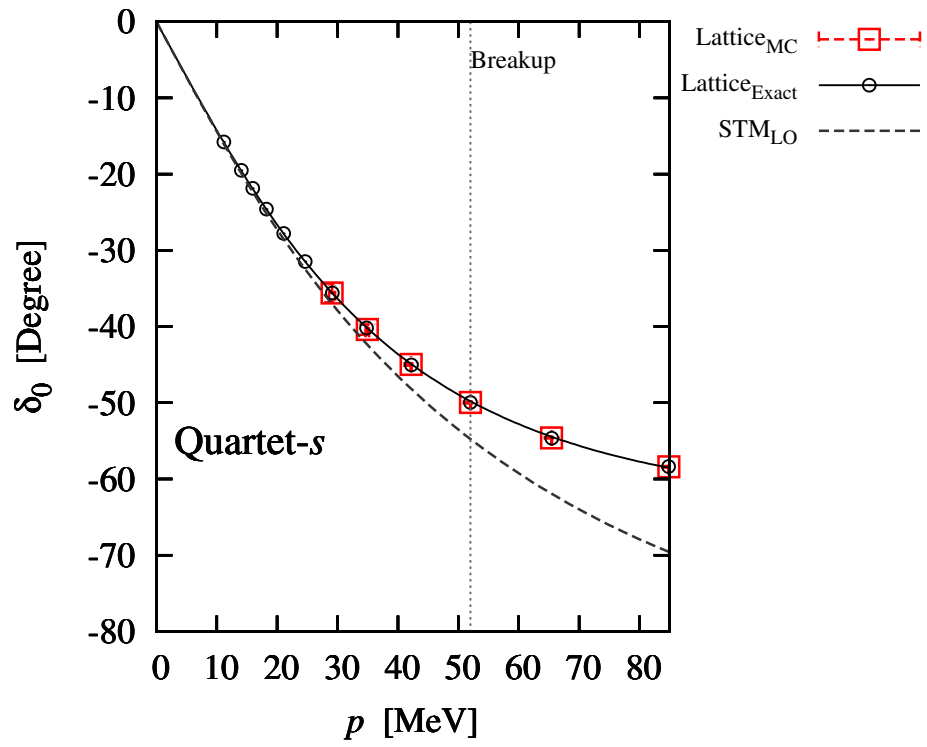


Figure 6.4 The s -wave scattering phase shift versus the relative momentum between fermion and dimer.

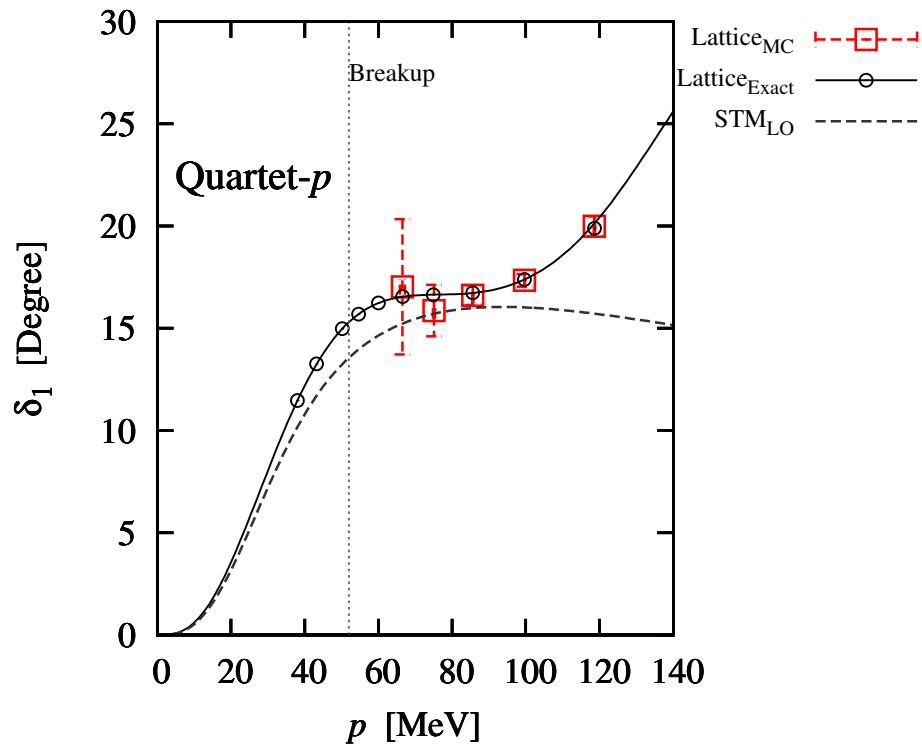


Figure 6.5 The p -wave scattering phase shift versus the relative momentum between fermion and dimer.

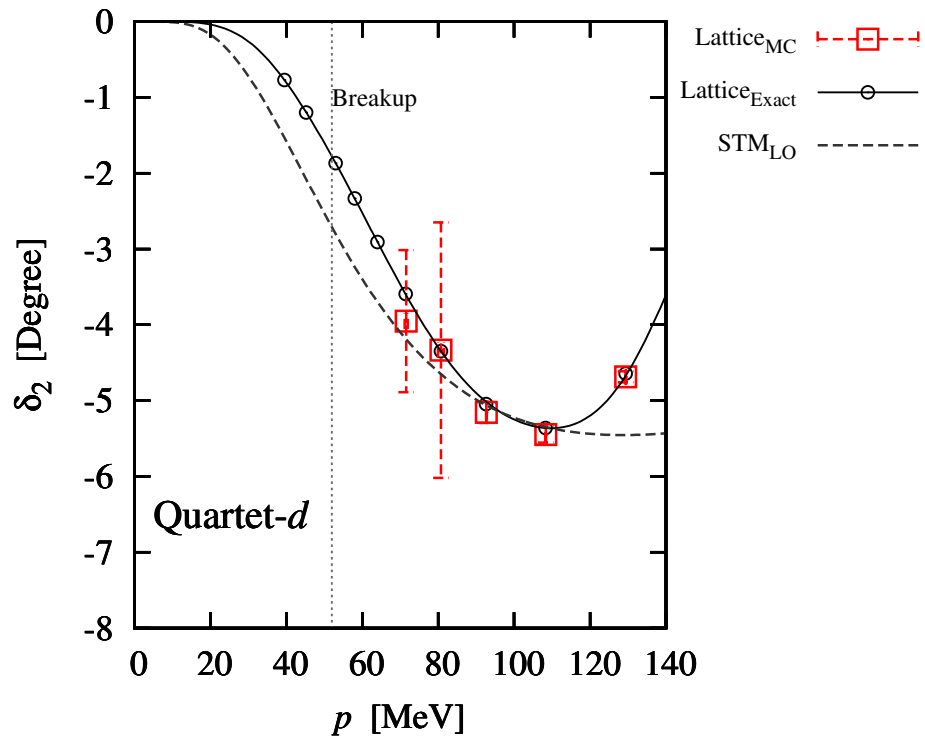


Figure 6.6 The d -wave scattering phase shift versus the relative momentum between fermion and dimer.

quartet channel at the leading order in pionless effective field theory. Therefore we choose to set the dimer energy to the physical deuteron energy of -2.2246 MeV and compare our lattice results to calculations of neutron-deuteron scattering in the continuum and infinite-volume limits at leading order in pionless effective field theory [10, 73, 153]. The Skorniakov-Ter-Martirosian (STM) integral equation for the T -matrix is

$$T_\ell(k, p) = -\frac{8\pi\gamma}{mpk} Q_\ell \left(\frac{p^2 + k^2 - mE - i0^+}{pk} \right) - \frac{2}{\pi} \int_0^\infty dq \frac{q}{p} \frac{T_\ell(k, q)}{\sqrt{3q^2/4 - mE - i0^+} - \gamma} Q_\ell \left(\frac{p^2 + q^2 - mE - i0^+}{pq} \right), \quad (6.43)$$

where γ is the dimer binding energy, $E = 3p^2/(4m) - \gamma^2/m$ is the total energy, and Q_ℓ is the Legendre function of the second kind,

$$Q_\ell(a) = \frac{1}{2} \int_{-1}^1 dx \frac{P_\ell(x)}{x+a}. \quad (6.44)$$

The scattering phase shifts can be calculated from the on-shell T -matrix formula,

$$T_\ell(p, p) = \frac{3\pi}{m} \frac{p^{2\ell}}{p^{2\ell+1} \cot \delta_\ell - ip^{2\ell+1}}. \quad (6.45)$$

We show results for the s -wave, p -wave and d -wave phase shifts in Fig. 6.4, 6.5 and 6.6 respectively. The square points indicate the data from the lattice Monte Carlo simulations, the circular points are the exact lattice calculations, and the solid lines are a fit of the exact lattice data using an effective range expansion,

$$p^{2\ell+1} \cot \delta_\ell(p) = -\frac{1}{a_\ell} + \frac{1}{2} r_\ell p^2 + \mathcal{O}(p^4). \quad (6.46)$$

The dashed lines are leading order results from the STM calculation. The dotted vertical lines

indicate the inelastic breakup threshold of the dimer. The range of lattice box sizes is $L \leq 16$ for the exact lattice and $L \leq 9$ for the Monte Carlo calculations.

Where we have overlapping data, we find excellent agreement between the Monte Carlo and exact lattice phase shifts. At very low energies we find that Monte Carlo calculations of the phase shifts become impractical due to the high sensitivity of Lüscher's method upon small deviations in the finite-volume energies. This should be regarded more as a limitation of Lüscher's formalism rather than a deficiency of the adiabatic projection method or impurity Monte Carlo.

We also find quite good agreement between the STM continuum results and the lattice results. Below the inelastic breakup threshold, the small deviation can be regarded as an estimate of lattice discretization errors. Above the breakup threshold there are also systematic errors since our analysis using Lüscher's method does not account for inelastic breakup processes. Nevertheless we see that the agreement with the STM calculation for the elastic phase shifts is still quite good, and the STM calculation does correctly account for breakup effects. To our knowledge these results are the first lattice calculations of fermion-dimer scattering in the p - and d -wave channels.

6.8 Summary and discussion

In this chapter we have presented the adiabatic projection method and its first application using Monte Carlo methods. The adiabatic method is a general framework for studying scattering and reactions on the lattice. The method constructs a low-energy effective theory for clusters, and in the limit of large Euclidean projection time the description becomes exact. In previous studies [154, 143] the initial cluster states were parameterized by the initial spatial separations between clusters. In this study we have used a new technique which parameterizes the cluster

states according to the relative momentum between clusters. This new approach is crucial for doing calculations with a small number of initial states in order to improve the efficiency of the Monte Carlo calculations. The system we have analyzed in detail here is fermion-dimer elastic scattering for two-component fermions interacting via zero-range attractive interactions.

For our calculations we have introduced a new Monte Carlo algorithm which we call impurity lattice Monte Carlo. This can be seen as a hybrid algorithm in between worldline and auxiliary-field Monte Carlo simulations. In impurity Monte Carlo we use worldline Monte Carlo for the impurities, and these impurity worldlines are acting as additional auxiliary fields in the simulation of the other particles. By using the impurity lattice Monte Carlo algorithm, we have found significant improvement over more standard auxiliary-field Monte Carlo calculations. In addition to greater speed and efficiency of the calculations, we also found a reduction of fermionic sign oscillations, and this has greatly improved the resulting accuracy.

We have found that the adiabatic projection method with impurity Monte Carlo enables highly accurate calculations of the finite-volume energy levels of the fermion-dimer system. From these energy levels we have used Lüscher's method to present the first lattice calculations of p -wave and d -wave phase shifts for fermion-dimer elastic scattering. In addition to finding excellent agreement between Monte Carlo and exact lattice phase shifts, we have also found good agreement with continuum STM calculations of neutron-deuteron elastic scattering in the spin-quartet channel at leading order in pionless effective field theory.

Our results show that the adiabatic projection method with Monte Carlo simulations is a viable approach to calculating elastic phase shifts. The method can be applied in a straightforward manner to other two-cluster scattering systems. One area where more work is needed is that our application of Lüscher's method does not account for inelastic breakup processes. Another area that needs improvement is that Lüscher's method has too much sensitivity to small changes in the finite-volume energy levels. For these reasons we are now working to develop new methods

which incorporates more information from the adiabatic projection wavefunction in order to extract scattering information in a more robust manner.

BIBLIOGRAPHY

- [1] S. Aoki, M. Fukugita, S. Hashimoto, K-I. Ishikawa, N. Ishizuka, Y. Iwasaki, K. Kanaya, T. Kaneko, Y. Kuramashi, V. Lesk, M. Okawa, Y. Taniguchi, A. Ukawa, and T. Yoshié. $i = 2$ pion scattering phase shift with wilson fermions. *Phys. Rev. D*, 67:014502, Jan 2003.
- [2] M. Bartenstein, A. Altmeyer, S. Riedl, S. Jochim, C. Chin, J. Hecker Denschlag, and R. Grimm. Crossover from a molecular bose-einstein condensate to degenerate fermi gas. *Phys. Rev. Lett.*, 92:120401, 2004.
- [3] S. R. Beane, P. F. Bedaque, K. Orginos, and M. J. Savage. Nucleon-nucleon scattering from fully dynamical lattice qcd. *Phys. Rev. Lett.*, 97:012001, Jul 2006.
- [4] Silas R. Beane, Paulo F. Bedaque, Thomas C. Luu, Kostas Orginos, Elisabetta Pallante, Assumpta Parreño, and Martin J. Savage. πK scattering in full qcd with domain-wall valence quarks. *Phys. Rev. D*, 74:114503, Dec 2006.
- [5] Silas R. Beane, Paulo F. Bedaque, Thomas C. Luu, Kostas Orginos, Elisabetta Pallante, Assumpta Parreño, and Martin J. Savage. Hyperon–nucleon scattering from fully-dynamical lattice qcd. *Nuclear Physics A*, 794(1-2):62 – 72, 2007.
- [6] Silas R. Beane, Paulo F. Bedaque, Kostas Orginos, and Martin J. Savage. $I = 2 \pi-\pi$ scattering from fully-dynamical mixed-action lattice qcd. *Phys. Rev. D*, 73:054503, Mar 2006.
- [7] Silas R. Beane, Thomas C. Luu, Kostas Orginos, Assumpta Parreño, Martin J. Savage, Aaron Torok, and André Walker-Loud. $K+K+$ scattering length from lattice qcd. *Phys. Rev. D*, 77:094507, May 2008.
- [8] Silas R. Beane, Kostas Orginos, and Martin J. Savage. Hadronic interactions from lattice qcd. *International Journal of Modern Physics E*, 17(07):1157–1218, 2008.
- [9] S.R. Beane, P.F. Bedaque, A. Parreño, and M.J. Savage. Two nucleons on a lattice. *Physics Letters B*, 585(1-2):106 – 114, 2004.
- [10] Paulo F. Bedaque and Harald W. Griebhammer. Quartet s-wave neutron deuteron scattering in effective field theory. *Nuclear Physics A*, 671(1-4):357 – 379, 2000.
- [11] Paulo F. Bedaque, H.-W. Hammer, and U. van Kolck. Renormalization of the three-body system with short-range interactions. *Phys. Rev. Lett.*, 82:463–467, 1999.
- [12] Paulo F. Bedaque, H.-W. Hammer, and U. van Kolck. The three-boson system with short-range interactions. *Nucl. Phys.*, A646:444–466, 1999.

- [13] Paulo F. Bedaque, H.-W. Hammer, and U. van Kolck. Effective theory of the triton. *Nucl. Phys.*, A676:357–370, 2000.
- [14] Paulo F. Bedaque and Ubirajara van Kolck. Effective field theory for few-nucleon systems. *Ann. Rev. Nucl. Part. Sci.*, 52:339–396, 2002.
- [15] V. Bernard, M. Lage, U.-G. Meißner, and A. Rusetsky. Resonance properties from the finite-volume energy spectrum. *Journal of High Energy Physics*, 2008(08):024, 2008.
- [16] V. Bernard, M. Lage, U.-G. Meißner, and A. Rusetsky. Scalar mesons in a finite volume. *Journal of High Energy Physics*, 2011(1), 2011.
- [17] M. Berninger, A. Zenesini, B. Huang, W. Harm, H.-C. Nägerl, F. Ferlaino, R. Grimm, P. S. Julienne, and J. M. Hutson. Universality of the Three-Body Parameter for Efimov States in Ultracold Cesium. *Phys. Rev. Lett.*, 107(12):120401, September 2011.
- [18] H. A. Bethe. Theory of the effective range in nuclear scattering. *Phys. Rev.*, 76:38–50, Jul 1949.
- [19] L. C. Biedenharn and J. M. Blatt. Neutron-proton scattering with spin-orbit coupling. ii. variational formulation and effective range theory. *Phys. Rev.*, 93:1387–1394, 1954.
- [20] John M. Blatt and L. C. Biedenharn. Neutron-proton scattering with spin-orbit coupling. i. general expressions. *Phys. Rev.*, 86:399–404, 1952.
- [21] D. Bollé and F. Gesztesy. Scattering observables in arbitrary dimension $n \geq 2$. *Phys. Rev. A*, 30:1279–1293, Sep 1984.
- [22] B. Borasoy, E. Epelbaum, H. Krebs, D. Lee, and U.-G. Meißner. Lattice simulations for light nuclei: Chiral effective field theory at leading order. *The European Physical Journal A*, 31(1):105–123, 2007.
- [23] B. Borasoy, E. Epelbaum, H. Krebs, D. Lee, and U.-G. Meißner. Two-particle scattering on the lattice: Phase shifts, spin-orbit coupling, and mixing angles. *The European Physical Journal A*, 34(2):185–196, 2007.
- [24] B. Borasoy, E. Epelbaum, H. Krebs, D. Lee, and U.-G. Meißner. Chiral effective field theory on the lattice at next-to-leading order. *The European Physical Journal A*, 35(3):343–355, 2008.
- [25] Bugra Borasoy, Evgeny Epelbaum, Hermann Krebs, Dean Lee, and Ulf-G. Meißner. Dilute neutron matter on the lattice at next-to-leading order in chiral effective field theory. *Eur. Phys. J.*, A35:357–367, 2008.

- [26] Shahin Bour, H.-W. Hammer, Dean Lee, and Ulf-G. Meißner. Benchmark calculations for elastic fermion-dimer scattering. *Phys. Rev. C*, 86:034003, Sep 2012.
- [27] Shahin Bour, Hans-Werner Hammer, Dean Lee, and Ulf-G. Meißner. Work in progress.
- [28] Shahin Bour, Sebastian König, Dean Lee, H.-W. Hammer, and Ulf-G. Meißner. Topological phases for bound states moving in a finite volume. *Phys. Rev. D*, 84:091503, Nov 2011.
- [29] Eric Braaten and H.-W. Hammer. Universality in few-body systems with large scattering length. *Phys. Rept.*, 428:259–390, 2006.
- [30] Raúl Briceño, Zohreh Davoudi, and Thomas Luu. Two-nucleon systems in a finite volume: Quantization conditions. *Phys. Rev. D*, 88:034502, Aug 2013.
- [31] Raúl A. Briceño. Two-particle multichannel systems in a finite volume with arbitrary spin. *Phys. Rev. D*, 89:074507, Apr 2014.
- [32] Raúl A. Briceño and Zohreh Davoudi. Moving multichannel systems in a finite volume with application to proton-proton fusion. *Phys. Rev. D*, 88:094507, Nov 2013.
- [33] Raúl A. Briceño, Zohreh Davoudi, Thomas C. Luu, and Martin J. Savage. Two-nucleon systems in a finite volume. ii. s13-d13 coupled channels and the deuteron. *Phys. Rev. D*, 88:114507, Dec 2013.
- [34] Ronald A. Bryan and Bruce L. Scott. Nucleon-nucleon scattering from one-boson-exchange potentials. *Phys. Rev.*, 135:B434–B450, Jul 1964.
- [35] A. Calle Cordón and E. Ruiz Arriola. Low-energy universality and scaling of van der waals forces. *Phys. Rev. A*, 81:044701, 2010.
- [36] A. Calle Cordon and E. Ruiz Arriola. Renormalization vs Strong Form Factors for One Boson Exchange Potentials. *Phys. Rev.*, C81:044002, 2010.
- [37] M. J. Cavagnero. Secular perturbation theory of long-range interactions. *Phys. Rev. A*, 50:2841–2846, Oct 1994.
- [38] Jiunn-Wei Chen, Gautam Rupak, and Martin J. Savage. Nucleon nucleon effective field theory without pions. *Nucl. Phys.*, A653:386–412, 1999.
- [39] Geoffrey F. Chew and Marvin L. Goldberger. On the analysis of nucleon-nucleon scattering experiments. *Phys. Rev.*, 75:1637–1644, Jun 1949.
- [40] R. Côté and A. Dalgarno. Elastic scattering of two na atoms. *Phys. Rev. A*, 50:4827–4835, Dec 1994.

- [41] R. Côté, E. J. Heller, and A. Dalgarno. Quantum suppression of cold atom collisions. *Phys. Rev. A*, 53:234–241, Jan 1996.
- [42] Michael Creutz. Gauge fixing, the transfer matrix, and confinement on a lattice. *Phys. Rev. D*, 15:1128–1136, Feb 1977.
- [43] Michael Creutz. Global monte carlo algorithms for many-fermion systems. *Phys. Rev. D*, 38:1228–1238, Aug 1988.
- [44] Michael Creutz. Transfer matrices and lattice fermions at finite density. *Foundations of Physics*, 30(3):487–492, 2000.
- [45] Zohreh Davoudi and Martin J. Savage. Improving the Volume Dependence of Two-Body Binding Energies Calculated with Lattice QCD. *Phys.Rev.*, D84:114502, 2011.
- [46] J.J de Swart and C Dullemond. Effective range theory and the low energy hyperon-nucleon interactions. *Annals of Physics*, 19(3):458 – 495, 1962.
- [47] A. Deltuva. Efimov physics in bosonic atom-trimer scattering. *Phys. Rev. A*, 82:040701, Oct 2010.
- [48] P.A.M. Dirac. The lagrangian in quantum mechanics. *Phys. Zeits. Sowjetunion*, 3:67–74, 1933.
- [49] John D. Dollard. Asymptotic convergence and the coulomb interaction. *Journal of Mathematical Physics*, 5(6), 1964.
- [50] M. Döring and U.-G. Meißner. Finite volume effects in pion-kaon scattering and reconstruction of the $\kappa(800)$ resonance. *Journal of High Energy Physics*, 2012(1), 2012.
- [51] M. Döring, U.-G. Meißner, E. Oset, and A. Rusetsky. Scalar mesons moving in a finite volume and the role of partial wave mixing. *The European Physical Journal A*, 48(8), 2012.
- [52] Michael Döring, Maxim Mai, and Ulf-G. Meißner. Finite volume effects and quark mass dependence of the $\Lambda(1520)$. *Physics Letters B*, 722(1–3):185 – 192, 2013.
- [53] V. N. Efimov. *Phys. Lett.*, 33:563, 1970.
- [54] V. N. Efimov. *Nucl. Phys. A*, 210:157, 1973.
- [55] Michael G. Endres, David B. Kaplan, Jong-Wan Lee, and Amy N. Nicholson. Lattice Monte Carlo calculations for unitary fermions in a harmonic trap. *Phys.Rev.*, A84:043644, 2011.

- [56] E. Epelbaum, H.-W. Hammer, and Ulf-G. Meißner. Modern theory of nuclear forces. *Rev. Mod. Phys.*, 81:1773–1825, Dec 2009.
- [57] E. Epelbaum, H. Krebs, D. Lee, and U.-G. Meißner. Lattice calculations for $a = 3, 4, 6, 12$ nuclei using chiral effective field theory. *The European Physical Journal A*, 45(3):335–352, 2010.
- [58] Evgeny Epelbaum. Few-nucleon forces and systems in chiral effective field theory. *Prog. Part. Nucl. Phys.*, 57:654–741, 2006.
- [59] Evgeny Epelbaum, Hans-Werner Hammer, and Ulf-G. Meißner. Modern Theory of Nuclear Forces. *Rev. Mod. Phys.*, 81:1773, 2009.
- [60] Evgeny Epelbaum, Hermann Krebs, Timo A. Lähde, Dean Lee, Ulf-G. Meißner, and Gautam Rupak. *Ab Initio* calculation of the spectrum and structure of ^{16}O . *Phys. Rev. Lett.*, 112:102501, Mar 2014.
- [61] Evgeny Epelbaum, Hermann Krebs, Dean Lee, and Ulf-G. Meißner. Ground state energy of dilute neutron matter at next-to-leading order in lattice chiral effective field theory. *Eur. Phys. J.*, A40:199–213, 2009.
- [62] Evgeny Epelbaum, Hermann Krebs, Dean Lee, and Ulf-G. Meißner. Lattice effective field theory calculations for $a = 3, 4, 6, 12$ nuclei. *Phys. Rev. Lett.*, 104:142501, Apr 2010.
- [63] Evgeny Epelbaum, Hermann Krebs, Dean Lee, and Ulf-G. Meißner. *Ab Initio* calculation of the hoyle state. *Phys. Rev. Lett.*, 106:192501, May 2011.
- [64] K. Erkelenz. Current status of the relativistic two-nucleon one boson exchange potential. *Physics Reports*, 13(5):191 – 258, 1974.
- [65] R. P. Feynman. Space-time approach to non-relativistic quantum mechanics. *Rev. Mod. Phys.*, 20:367–387, Apr 1948.
- [66] V. V. Flambaum, G. F. Gribakin, and C. Harabati. Analytical calculation of cold-atom scattering. *Phys. Rev. A*, 59:1998–2005, Mar 1999.
- [67] Zoltan Fodor and Christian Hoelbling. Light hadron masses from lattice qcd. *Rev. Mod. Phys.*, 84:449–495, Apr 2012.
- [68] W. M. Frank, D. J. Land, and R. M. Spector. Singular potentials. *Rev. Mod. Phys.*, 43:36–98, 1971.
- [69] H. Fritzsch and M. Gell-Mann. In *Proc. XVI Int. Conf. on High Energy Physics*, Chicago-Batavia, 1972.

- [70] H. Fritzsche, M. Gell-Mann, and H. Leutwyler. Advantages of the color octet gluon picture. *Physics Letters B*, 47(4):365 – 368, 1973.
- [71] Ziwen Fu. Rummukainen-gottlieb formula on a two-particle system with different masses. *Phys. Rev. D*, 85:014506, Jan 2012.
- [72] M. Fukugita, Y. Kuramashi, M. Okawa, H. Mino, and A. Ukawa. Hadron scattering lengths in lattice qcd. *Phys. Rev. D*, 52:3003–3023, Sep 1995.
- [73] Fabrizio Gabbiani, Paulo F. Bedaque, and Harald W. Griesshammer. Higher partial waves in an effective field theory approach to nd scattering. *Nuclear Physics A*, 675(3–4):601 – 620, 2000.
- [74] B. Gao. Analytic description of atomic interaction at ultracold temperatures. II. Scattering around a magnetic Feshbach resonance. *Phys. Rev. A*, 84(2):022706, August 2011.
- [75] Bo Gao. Quantum-defect theory of atomic collisions and molecular vibration spectra. *Phys. Rev. A*, 58:4222–4225, Nov 1998.
- [76] Bo Gao. Solutions of the schrödinger equation for an attractive $1/r^6$ potential. *Phys. Rev. A*, 58:1728–1734, Sep 1998.
- [77] Bo Gao. Angular-momentum-insensitive quantum-defect theory for diatomic systems. *Phys. Rev. A*, 64:010701, Jun 2001.
- [78] Bo Gao. General form of the quantum-defect theory for $1/r^\alpha$ type of potentials with $\alpha > 2$. *Phys. Rev. A*, 78:012702, Jul 2008.
- [79] Bo Gao. Analytic description of atomic interaction at ultracold temperatures: The case of a single channel. *Phys. Rev. A*, 80:012702, Jul 2009.
- [80] Bo Gao, Eite Tiesinga, Carl J. Williams, and Paul S. Julienne. Multichannel quantum-defect theory for slow atomic collisions. *Phys. Rev. A*, 72:042719, Oct 2005.
- [81] J Gasser and H Leutwyler. Chiral perturbation theory to one loop. *Annals of Physics*, 158(1):142 – 210, 1984.
- [82] J. Gasser, M.E. Sainio, and A. Šarc. Nucleons with chiral loops. *Nuclear Physics B*, 307(4):779 – 853, 1988.
- [83] M. Gattobigio, A. Kievsky, and M. Viviani. Spectra of helium clusters with up to six atoms using soft-core potentials. *Phys. Rev. A*, 84:052503, Nov 2011.
- [84] M. Gell-Mann. A schematic model of baryons and mesons. *Physics Letters*, 8(3):214 – 215, 1964.

- [85] H. Georgi. Thoughts on effective field theory. *Nucl. Phys. Proc. Suppl.*, 29BC:1–10, 1992.
- [86] Alexandros Gezerlis and J. Carlson. Strongly paired fermions: Cold atoms and neutron matter. *Phys. Rev.*, C77:032801, 2008.
- [87] Alexandros Gezerlis and J. Carlson. Low-density neutron matter. *Phys. Rev.*, C81:025803, 2010.
- [88] Stefano Giorgini, Lev P. Pitaevskii, and Sandro Stringari. Theory of ultracold fermi gases. *Rev. Mod. Phys.*, 80:1215, 2008.
- [89] M. Göckeler, R. Horsley, M. Lage, U.-G. Meißner, P. E. L. Rakow, A. Rusetsky, G. Schierholz, and J. M. Zanotti. Scattering phases for meson and baryon resonances on general moving-frame lattices. *Phys. Rev. D*, 86:094513, Nov 2012.
- [90] M.L. Goldberger and K.M. Watson. *Collision Theory*. Dover Publications, 2004.
- [91] C. Greene, U. Fano, and G. Strinati. General form of the quantum-defect theory. *Phys. Rev. A*, 19:1485–1509, Apr 1979.
- [92] Chris H. Greene, A. R. P. Rau, and U. Fano. General form of the quantum-defect theory. ii. *Phys. Rev. A*, 26:2441–2459, Nov 1982.
- [93] M. R. Hadizadeh, M. T. Yamashita, Lauro Tomio, A. Delfino, and T. Frederico. Scaling properties of universal tetramers. *Phys. Rev. Lett.*, 107:135304, Sep 2011.
- [94] H. W. Hammer and Dean Lee. Causality and universality in low-energy quantum scattering. *Phys. Lett.*, B681:500–503, 2009.
- [95] H. W. Hammer and Dean Lee. Causality and the effective range expansion. *Annals Phys.*, 325:2212–2233, 2010.
- [96] H. W. Hammer and L. Platter. Universal Properties of the Four-Body System with Large Scattering Length. *Eur. Phys. J.*, A32:113–120, 2007.
- [97] N. Ishii, S. Aoki, and T. Hatsuda. Nuclear force from lattice qcd. *Phys. Rev. Lett.*, 99:022001, Jul 2007.
- [98] A.D. Jackson, D.O. Riska, and B. Verwest. Meson exchange model for the nucleon-nucleon interaction. *Nuclear Physics A*, 249(3):397 – 444, 1975.
- [99] J. David Jackson and John M. Blatt. The interpretation of low energy proton-proton scattering. *Rev. Mod. Phys.*, 22:77–118, Jan 1950.

- [100] J.M. Jauch. Theory of the scattering operator.ii, multichannel scattering. *Helvetica Physica Acta*, 31:661, 1958.
- [101] R.C. Johnson. Angular momentum on a lattice. *Physics Letters B*, 114(2-3):147 – 151, 1982.
- [102] M.W. Kermode. Effective range theory for multi-channel scattering. *Nuclear Physics A*, 99(4):605 – 624, 1967.
- [103] J. Kinast, S. L. Hemmer, M. E. Gehm, A. Turlapov, and J. E. Thomas. Evidence for superfluidity in a resonantly interacting fermi gas. *Phys. Rev. Lett.*, 92:150402, 2004.
- [104] Thorsten Koehler, Krzysztof Goral, and Paul S. Julienne. Production of cold molecules via magnetically tunable feshbach resonances. *Rev. Mod. Phys.*, 78:1311, 2006.
- [105] Sebastian König. *Effective quantum theories with short-and long-range forces*. PhD thesis, Universitäts-und Landesbibliothek Bonn, 2013.
- [106] Sebastian König, Dean Lee, and H.-W. Hammer. Volume Dependence of Bound States with Angular Momentum. *Phys.Rev.Lett.*, 107:112001, 2011.
- [107] Sebastian König, Dean Lee, and H.-W. Hammer. Causality constraints for charged particles. 2012.
- [108] Sebastian König, Dean Lee, and H.-W. Hammer. Non-relativistic bound states in a finite volume. *Annals of Physics*, 327(6):1450 – 1471, 2012.
- [109] Sebastian König, Dean Lee, and H.-W. Hammer. Non-relativistic bound states in a finite volume. *Annals Phys.*, 327:1450–1471, 2012.
- [110] T. Kraemer, M. Mark, P. Waldburger, J. G. Danzl, C. Chin, B. Engeser, A. D. Lange, K. Pilch, A. Jaakkola, H.-C. Naegerl, and R. Grimm. Evidence for efimov quantum states in an ultracold gas of cesium atoms. *Nature*, 440:315, 2006.
- [111] Simon Kreuzer and Harald W. Griesshammer. Three particles in a finite volume: The breakdown of spherical symmetry. 2012.
- [112] Simon Kreuzer and H.-W. Hammer. The Triton in a finite volume. *Phys.Lett.*, B694:424–429, 2011.
- [113] Mark J. H. Ku, Ariel T. Sommer, Lawrence W. Cheuk, and Martin W. Zwierlein. Revealing the superfluid lambda transition in the universal thermodynamics of a unitary fermi gas. *Science*, 335(6068):563–567, 2012.
- [114] Y. Kuramashi, M. Fukugita, H. Mino, M. Okawa, and A. Ukawa. Lattice qcd calculation of full pion scattering lengths. *Phys. Rev. Lett.*, 71:2387–2390, Oct 1993.

- [115] M. Lacombe, B. Loiseau, J. M. Richard, R. Vinh Mau, J. Côté, P. Pirès, and R. de Tournreil. Parametrization of the paris $n - -n$ potential. *Phys. Rev. C*, 21:861–873, Mar 1980.
- [116] Timo A. Lähde, Evgeny Epelbaum, Hermann Krebs, Dean Lee, Ulf-G. Meißner, and Gautam Rupak. Lattice effective field theory for medium-mass nuclei. *Physics Letters B*, 732(0):110 – 115, 2014.
- [117] Dean Lee. The Ground state energy at unitarity. *Phys. Rev.*, C78:024001, 2008.
- [118] Dean Lee. Lattice simulations for few- and many-body systems. *Prog.Part.Nucl.Phys.*, 63:117–154, 2009.
- [119] Luka Leskovec and Sasa Prelovsek. Scattering phase shifts for two particles of different mass and nonzero total momentum in lattice qcd. *Phys. Rev. D*, 85:114507, Jun 2012.
- [120] Ning Li and Chuan Liu. Generalized lüscher formula in multichannel baryon-meson scattering. *Phys. Rev. D*, 87:014502, Jan 2013.
- [121] C.-J.D. Lin, G. Martinelli, E. Pallante, C.T. Sachrajda, and G. Villadoro. Finite-volume two-pion amplitudes in the $i=0$ channel. *Physics Letters B*, 553(3-4):229 – 241, 2003.
- [122] M. Lüscher. Volume dependence of the energy spectrum in massive quantum field theories. *Communications in Mathematical Physics*, 105(2):153–188, 1986.
- [123] M. Lüscher. Volume dependence of the energy spectrum in massive quantum field theories. 1. stable particle states. *Commun. Math. Phys.*, 104:177, 1986.
- [124] Martin Lüscher. Two-particle states on a torus and their relation to the scattering matrix. *Nuclear Physics B*, 354(2–3):531 – 578, 1991.
- [125] Thomas Luu and Martin J. Savage. Extracting scattering phase shifts in higher partial waves from lattice qcd calculations. *Phys. Rev. D*, 83:114508, Jun 2011.
- [126] R. Machleidt. High-precision, charge-dependent bonn nucleon-nucleon potential. *Phys. Rev. C*, 63:024001, Jan 2001.
- [127] R. Machleidt and D.R. Entem. Chiral effective field theory and nuclear forces. *Physics Reports*, 503(1):1 – 75, 2011.
- [128] R. Machleidt and I. Slaus. The nucleon-nucleon interaction: Topical review. *J. Phys. G: Nucl. Part. Phys.*, 27:R69, 2001.
- [129] M. Marinescu. Computation of the scattering length and effective range in molecular physics. *Phys. Rev. A*, 50:3177–3180, Oct 1994.

- [130] A. Martínez Torres, L. R. Dai, C. Koren, D. Jido, and E. Oset. Kd. *Phys. Rev. D*, 85:014027, Jan 2012.
- [131] M. McNeil Forbes, S. Gandolfi, and A. Gezerlis. Effective-Range Dependence of Resonantly Interacting Fermions. May 2012.
- [132] Nicholas Metropolis, Arianna W. Rosenbluth, Marshall N. Rosenbluth, Augusta H. Teller, and Edward Teller. Equation of state calculations by fast computing machines. *The Journal of Chemical Physics*, 21(6), 1953.
- [133] Tim-Oliver Müller, Alexander Kaiser, and Harald Friedrich. s -wave scattering for deep potentials with attractive tails falling off faster than $-1/r^2$. *Phys. Rev. A*, 84:032701, Sep 2011.
- [134] M. M. Nagels, T. A. Rijken, and J. J. de Swart. Low-energy nucleon-nucleon potential from regge-pole theory. *Phys. Rev. D*, 17:768–776, Feb 1978.
- [135] E.J. Newman and G.T. Barkema. *Monte Carlo Methods in Statistical Physics*. Clarendon Press, 1999.
- [136] Roger G. Newton. *Scattering theory of waves and particles*. 1982.
- [137] Y. Nishida and D. Thanh Son. Unitary Fermi gas, epsilon expansion, and nonrelativistic conformal field theories. *ArXiv e-prints*, April 2010.
- [138] K. M. O’Hara, S. L. Hemmer, M. E. Gehm, S. R. Granade, and J. E. Thomas. Observation of a strongly interacting degenerate fermi gas of atoms. *Science*, 298:2179–2182, 2002.
- [139] Thomas F. O’Malley, Larry Spruch, and Leonard Rosenberg. Modification of effective-range theory in the presence of a long-range ($1/r^4$) potential. *Journal of Mathematical Physics*, 2(4), 1961.
- [140] M. Pavon Valderrama and E. Ruiz Arriola. Renormalization of NN Interaction with Chiral Two Pion Exchange Potential. Central Phases and the Deuteron. *Phys. Rev.*, C74:054001, 2006.
- [141] M. E. Peskin and D. V. Schroeder. *Introduction to Quantum Field Theory*. Addison-Wesley, 1995.
- [142] Daniel R. Phillips and Thomas D. Cohen. How short is too short? constraining zero-range interactions in nucleon nucleon scattering. *Phys. Lett.*, B390:7–12, 1997.
- [143] Michelle Pine, Dean Lee, and Gautam Rupak. Adiabatic projection method for scattering and reactions on the lattice. *Eur.Phys.J.*, A49:151, 2013.

- [144] L. Platter, H.-W. Hammer, and Ulf-G. Meißner. The four-boson system with short-range interactions. *Phys. Rev.*, A70:052101, 2004.
- [145] L. Platter, H.-W. Hammer, and Ulf-G. Meißner. On the correlation between the binding energies of the triton and the alpha-particle. *Phys. Lett.*, B607:254–258, 2005.
- [146] M. Raoult and F. H. Mies. Feshbach resonance in atomic binary collisions in the wigner threshold law regime. *Phys. Rev. A*, 70:012710, Jul 2004.
- [147] C. Regal and D. S. Jin. Experimental realization of bcs-bec crossover physics with a fermi gas of atoms. 2006.
- [148] A Rokash, E Epelbaum, H Krebs, D Lee, and U-G Meißner. Finite volume effects in low-energy neutron–deuteron scattering. *Journal of Physics G: Nuclear and Particle Physics*, 41(1):015105, 2014.
- [149] Marc H Ross and Gordon L Shaw. Multichannel effective range theory. *Annals of Physics*, 13(2):147 – 186, 1961.
- [150] Sanjukta Roy, Manuele Landini, Andreas Trenkwalder, Giulia Semeghini, Giacomo Spagnolli, Andrea Simoni, Marco Fattori, Massimo Inguscio, and Giovanni Modugno. Test of the universality of the three-body efimov parameter at narrow feshbach resonances. *Phys. Rev. Lett.*, 111:053202, Aug 2013.
- [151] E. Ruiz Arriola. Van der Waals Forces and Photon-Less Effective Field Theory. *Few-Body Systems*, 50:399–402, May 2011.
- [152] K. Rummukainen and Steven Gottlieb. Resonance scattering phase shifts on a non-rest-frame lattice. *Nuclear Physics B*, 450(1–2):397 – 436, 1995.
- [153] Gautam Rupak and Xin-Wei Kong. Quartet s-wave p–d scattering in {EFT}. *Nuclear Physics A*, 717(1–2):73 – 90, 2003.
- [154] Gautam Rupak and Dean Lee. Radiative capture reactions in lattice effective field theory. *Phys.Rev.Lett.*, 111(3):032502, 2013.
- [155] Brandon P. Ruzic, Chris H. Greene, and John L. Bohn. Quantum defect theory for high-partial-wave cold collisions. *Phys. Rev. A*, 87:032706, Mar 2013.
- [156] Frauke Schwarz, Tim-Oliver Müller, and Harald Friedrich. Near-threshold feshbach resonances in interatomic collisions and spectra. *Phys. Rev. A*, 85:052703, May 2012.
- [157] M. J. Seaton. 1. *Rep. Prog. Phys.*, 46:167, 1983.
- [158] M.J. Seaton. Coulomb functions for attractive and repulsive potentials and for positive and negative energies. *Computer Physics Communications*, 146(2):225 – 249, 2002.

- [159] Jean-Marc Sparenberg, Pierre Capel, and Daniel Baye. Influence of low-energy scattering on loosely bound states. *Phys. Rev. C*, 81:011601, Jan 2010.
- [160] H. P. Stapp, T. J. Ypsilantis, and N. Metropolis. Phase-shift analysis of 310-mev proton-proton scattering experiments. *Phys. Rev.*, 105:302–310, 1957.
- [161] V. G. J. Stoks, R. A. M. Klomp, M. C. M. Rentmeester, and J. J. de Swart. Partial-wave analysis of all nucleon-nucleon scattering data below 350 mev. *Phys. Rev. C*, 48:792–815, 1993.
- [162] V. G. J. Stoks, R. A. M. Klomp, C. P. F. Terheggen, and J. J. de Swart. Construction of high-quality *NN* potential models. *Phys. Rev. C*, 49:2950–2962, 1994.
- [163] M. S. Swanson. *Path Integrals and Quantum Processes*. Elsevier Science, 1992.
- [164] J.R. Taylor. *Scattering Theory: The Quantum Theory of Nonrelativistic Collisions*. Dover Publications, 2006.
- [165] M. Pavón Valderrama and E. Ruiz Arriola. Low-energy *NN* scattering at next-to-next-to-next-to-next-to-leading order for partial waves with $j \leq 5$. *Phys. Rev. C*, 72:044007, 2005.
- [166] U. van Kolck. Effective field theory of nuclear forces. *Prog. Part. Nucl. Phys.*, 43:337–418, 1999.
- [167] U. van Kolck. Effective field theory of short range forces. *Nucl. Phys.*, A645:273–302, 1999.
- [168] J. von Stecher, J. P. D’Incao, and C. H. Greene. Four-body legacy of the Efimov effect. *ArXiv e-prints*, October 2008.
- [169] J. Wang, J. P. D’Incao, B. D. Esry, and C. H. Greene. Origin of the Three-Body Parameter Universality in Efimov Physics. *Physical Review Letters*, 108(26):263001, June 2012.
- [170] Y. Wang, J. Wang, J. P. D’Incao, and C. H. Greene. Universal Three-Body Parameter in Heteronuclear Atomic Systems. *Physical Review Letters*, 109(24):243201, December 2012.
- [171] Steven Weinberg. Phenomenological Lagrangians. *Physica*, A96:327, 1979.
- [172] Steven Weinberg. Nuclear forces from chiral lagrangians. *Physics Letters B*, 251(2):288 – 292, 1990.
- [173] Steven Weinberg. Effective chiral lagrangians for nucleon-pion interactions and nuclear forces. *Nuclear Physics B*, 363(1):3 – 18, 1991.

- [174] Eugene P. Wigner. Lower limit for the energy derivative of the scattering phase shift. *Phys. Rev.*, 98(1):145–147, 1955.
- [175] Kenneth G. Wilson. Confinement of quarks. *Phys. Rev. D*, 10:2445–2459, Oct 1974.
- [176] R. B. Wiringa, V. G. J. Stoks, and R. Schiavilla. Accurate nucleon-nucleon potential with charge-independence breaking. *Phys. Rev. C*, 51:38–51, Jan 1995.
- [177] Gabriel Wlazlowski and Piotr Magierski. Quantum Monte Carlo study of dilute neutron matter at finite temperatures. *Phys. Rev.*, C83:012801, 2011.
- [178] H. Yukawa. on the interaction of elementary particles. i. *Proc. Phys. Math. Soc. Japan*, 17:48, 1935.
- [179] A. Zee. *Quantum Field Theory in a Nutshell*. Princeton Univ. Press, Princeton, NJ, 2010.
- [180] M. W. Zwierlein, C. A. Stan, C. H. Schunck, S. M. F. Raupach, A. J. Kerman, and W. Ketterle. Condensation of pairs of fermionic atoms near a feshbach resonance. *Phys. Rev. Lett.*, 92:120403, 2004.

APPENDICES

Appendix A

A.1 Bessel and related Functions

$S_\ell(r)$ and $C_\ell(r)$ are Riccati-Bessel and Riccati-Neumann functions, which are defined in terms of the Bessel and Neumann functions as

$$S_\ell(x) = \sqrt{\frac{\pi x}{2}} J_{\ell+\frac{1}{2}}(x) = \sqrt{\pi} \left(\frac{x}{2}\right)^{\ell+1} \sum_{n=0}^{\infty} \frac{i^{2n}}{\Gamma(n+1)\Gamma(n+\ell+\frac{3}{2})} \left(\frac{x}{2}\right)^{2n}, \quad (\text{A.1})$$

$$\begin{aligned} C_\ell(x) &= -\sqrt{\frac{\pi r}{2}} N_{\ell+\frac{1}{2}}(x) \\ &= \frac{1}{\sqrt{\pi}} \left(\frac{x}{2}\right)^{-\ell} \Gamma(-\ell+\frac{1}{2})\Gamma(\ell+\frac{1}{2}) \sum_{n=0}^{\infty} \frac{i^{2n}}{\Gamma(n+1)\Gamma(n-\ell+1/2)} \left(\frac{x}{2}\right)^{2n}. \end{aligned} \quad (\text{A.2})$$

We define the following functions $s_\ell(p, r)$ and $c_\ell(p, r)$ in terms of Riccati-Bessel and Riccati-Neumann functions,

$$s_\ell(p, r) = p^{-\ell-1} S_\ell(pr) = \sum_{n=0}^{\infty} \frac{\sqrt{\pi} i^{2n} p^{2n}}{\Gamma(n+1)\Gamma(n+\ell+\frac{3}{2})} \left(\frac{r}{2}\right)^{2n+\ell+1}, \quad (\text{A.3})$$

$$c_\ell(p, r) = p^\ell C_\ell(pr) = \sum_{n=0}^{\infty} \frac{i^{2n} p^{2n}}{\sqrt{\pi}} \frac{\Gamma(-\ell + \frac{1}{2})\Gamma(\ell + \frac{1}{2})}{\Gamma(n+1)\Gamma(n-\ell+1/2)} \left(\frac{r}{2}\right)^{2n-\ell}. \quad (\text{A.4})$$

The relations in Eqs. (A.3) and (A.4) with Eqs. (A.1) and (A.2) indicate that $s_\ell(p, r)$ and $c_\ell(p, r)$ can be written in powers of p^2 ,

$$s_\ell(p, r) = \sum_{n=0}^{\infty} s_{2n, \ell}(r) p^{2n+2} \quad \text{and} \quad c_\ell(p, r) = \sum_{n=0}^{\infty} c_{2n, \ell}(r) p^{2n+2}, \quad (\text{A.5})$$

where $s_{n, \ell}(r)$ and $c_{n, \ell}(r)$ are

$$s_{n, \ell}(r) = \frac{\sqrt{\pi} i^{2n}}{\Gamma(n+1)\Gamma(n+\ell+\frac{3}{2})} \left(\frac{r}{2}\right)^{2n+\ell+1}, \quad (\text{A.6})$$

$$c_{n, \ell}(r) = \frac{i^{2n}}{\sqrt{\pi}} \frac{\Gamma(-\ell + \frac{1}{2})\Gamma(\ell + \frac{1}{2})}{\Gamma(n+1)\Gamma(n-\ell+\frac{1}{2})} \left(\frac{r}{2}\right)^{2n-\ell}. \quad (\text{A.7})$$

A.2 Coulomb wave functions

We consider radial wave function $V_\ell^{(p)}(r)$ that satisfies the radial Schrödinger equation for $r > R$,

$$\left[\frac{d^2}{dr^2} - \frac{\ell(\ell+1)}{r^2} - \frac{\gamma}{r} + p^2 \right] V_\ell^{(p)}(r) = 0, \quad (\text{A.8})$$

where μ is the reduced mass, and $\gamma = 2\mu\alpha Z_1 Z_2$. Defining $r_\gamma = -\gamma r/2$ and $\varepsilon = 4p^2/\gamma^2$ Eq. (A.8) can be written as

$$\left[\frac{d^2}{dr_\gamma^2} - \frac{\ell(\ell+1)}{r_\gamma^2} + \frac{2}{r_\gamma} + \varepsilon \right] \chi = 0, \quad (\text{A.9})$$

The solution to this differential equation has the form [158] of

$$\chi(\varepsilon, \ell; r_\gamma) = \sum_{q=0}^{\infty} \varepsilon^q \left[\sum_{p=0}^q \alpha_{q-p} \chi_q(\ell, r_\gamma) \right], \quad (\text{A.10})$$

as linearly independent functions $\chi_q(\ell, r_\gamma)$,

$$\chi_q(\ell, r_\gamma) = \begin{cases} \sum_{p=2q}^{3q} C_{q,p} \phi_p(\ell, r_\gamma) & q > 1, \\ -\frac{(\ell+1)}{4} \phi_2 + \frac{1}{12} \phi_3 & q = 1, \\ \phi_0(\ell, r_\gamma) & q = 0, \end{cases} \quad (\text{A.11})$$

where

$$\phi_p(\ell, r_\gamma) = a P_p(\ell, r_\gamma) + b Q_p(\ell, r_\gamma), \quad (\text{A.12})$$

and

$$C_{q,p} = \begin{cases} \frac{-(2\ell+p)C_{q-1,p-2} + C_{q-1,p-3}}{4p} & \text{for } 2q \leq p \leq 3q, \\ 1 & \text{for } q = p = 0, \\ 0 & \text{for } 2q > p \text{ and } p > 3q. \end{cases} \quad (\text{A.13})$$

The coefficient α_p in Eq. (A.11) and the constants a and b in Eq. (A.12) are to be determined depending on the choice of normalization of the function $\chi(\varepsilon, \ell; r_\gamma)$. The functions $P_p(\ell, r_\gamma)$ and $Q_p(\ell, r_\gamma)$ are defined in terms of Bessel and Modified Bessel functions

$$P_p(\ell, r_\gamma) = \begin{cases} (2r_\gamma)^{(p+1)/2} J_{2\ell+1+p}(2\sqrt{2r_\gamma}) & \text{for } r_\gamma > 0, \\ (-1)^{\ell+1+p} (-2r_\gamma)^{(p+1)/2} I_{2\ell+1+p}(\sqrt{-8r_\gamma}) & \text{for } r_\gamma < 0, \end{cases} \quad (\text{A.14})$$

and

$$Q_p(\ell, r_\gamma) = \begin{cases} (2r_\gamma)^{(p+1)/2} Y_{2\ell+1+p}(2\sqrt{2r_\gamma}) & \text{for } r_\gamma > 0, \\ \frac{2}{\pi} (-1)^{\ell+1+p} (-2r_\gamma)^{(p+1)/2} K_{2\ell+1+p}(\sqrt{-8r_\gamma}) & \text{for } r_\gamma < 0. \end{cases} \quad (\text{A.15})$$

A.2.1 Regular solution $f(\varepsilon, \ell; r_\gamma)$

Here the normalization of the Coulomb wave functions is chosen as the same as that of Ref. [21]. From the functions introduced in the previous section, the regular Coulomb wave function is written as a convergent expansion in ε ,

$$f(\varepsilon, \ell; r_\gamma) = \sum_{q=0}^{\infty} \varepsilon^q \left[\sum_{p=0}^q \alpha_{q-p} \chi_p^{(f)}(\ell, r_\gamma) \right], \quad (\text{A.16})$$

and this function is equivalent to $f_\ell(p, r)$ in Eq. (2.56). Comparing to the regular function of Bollé and Gesztesy [21], we find $a = 1$, $b = 0$ and α_q as

$$\alpha_q = \begin{cases} \frac{(2\ell+1)!}{(-\gamma)^{\ell+1}} & \text{for } q = 0 \text{ and } r_\gamma > 0, \\ (-1)^{-\ell} \frac{(2\ell+1)!}{(-\gamma)^{\ell+1}} & \text{for } q = 0 \text{ and } r_\gamma < 0, \\ 0 & \text{for } q \geq 1. \end{cases} \quad (\text{A.17})$$

We find the first few functions of the expansion of $f_\ell(p, r)$ in power of p^2 that we use in Eq. (2.59)–(2.62) are

$$f_{0,\ell}^\pm(r) = \frac{(2\ell+1)!}{(\pm\gamma)^{\ell+1/2}} \sqrt{r} \mathcal{J}_{2\ell+1}^{(\pm)}(2\sqrt{\pm\gamma r}), \quad (\text{A.18})$$

$$f_{2,\ell}^{\pm}(r) = -\frac{(2\ell+1)!}{3} \frac{\sqrt{r^3}}{(\pm\gamma)^{\ell+3/2}} \left[3(\ell+1) \mathcal{J}_{2\ell+3}^{(\pm)}(2\sqrt{\pm\gamma r}) \pm \sqrt{\pm\gamma r} \mathcal{J}_{2\ell+4}^{(\pm)}(2\sqrt{\pm\gamma r}) \right], \quad (\text{A.19})$$

$$f_{4,\ell}^{\pm}(r) = \frac{(2\ell+1)!}{90} \frac{\sqrt{r^5}}{(\pm\gamma)^{\ell+5/2}} \left[5(r\gamma + 9\ell^2 + 27\ell + 18) \mathcal{J}_{2\ell+5}^{(\pm)}(2\sqrt{\pm\gamma r}) \right. \\ \left. \pm (20\ell + 18) \sqrt{\pm\gamma r} \mathcal{J}_{2\ell+6}^{(\pm)}(2\sqrt{\pm\gamma r}) \right], \quad (\text{A.20})$$

$$f_{6,\ell}^{\pm}(r) = -\frac{(2\ell+1)!}{5670} \frac{\sqrt{r^7}}{(\pm\gamma)^{\ell+7/2}} \\ \left\{ 7[135\ell^3 + 810\ell^2 + 5\ell(7r\gamma + 297) + 54(r\gamma + 15)] \mathcal{J}_{2\ell+7}^{(\pm)}(2\sqrt{\pm\gamma r}) \right. \\ \left. \pm \sqrt{\pm\gamma r} (455\ell^2 + 1253\ell + 35r\gamma + 810) \mathcal{J}_{2\ell+8}^{(\pm)}(2\sqrt{\pm\gamma r}) \right\}, \quad (\text{A.21})$$

where $\mathcal{J}_n^{(-)}(x)$ is the Bessel function of the first kind $J_n(x)$ and $\mathcal{J}_n^{(+)}(x)$ is the modified Bessel function of the first kind $I_n(x)$.

A.2.2 Irregular solution.I $h(\varepsilon, \ell; r_\gamma)$

The first irregular Coulomb wave function is obtained setting $a = 0$ and $b = 1$ in Eq. (A.12),

$$h(\varepsilon, \ell; r_\gamma) = A(\varepsilon, \ell) \left[\sum_{q=0}^M \varepsilon^q \chi_q^{(h)}(\ell, r_\gamma) + \mathcal{O}(\varepsilon^{M+1}) \right], \quad (\text{A.22})$$

where

$$\chi_q^{(h)}(\ell, r_\gamma) = \begin{cases} \sum_{p=2q}^{3q} C_{q,p} Q_p(\ell, r_\gamma) & q > 1, \\ -\frac{(\ell+1)}{4} Q_2 + \frac{1}{12} Q_3 & q = 1, \\ Q_0(\ell, r_\gamma) & q = 0, \end{cases} \quad (\text{A.23})$$

and

$$A(\varepsilon, \ell) = \prod_{p=0}^{\ell} (1 + p^2 \varepsilon) = \sum_{n=0}^{\ell} \varepsilon^n \sigma_{n,\ell}. \quad (\text{A.24})$$

However, this irregular solution $h(\varepsilon, \ell; r_\gamma)$ is not a desired function since it is not analytic in ε .

A.2.3 Irregular solution.II $g(\varepsilon, \ell; r_\gamma)$

The second irregular Coulomb wave function which is analytic in ε is defined as a linear combination of $h(\varepsilon, \ell; r_\gamma)$ and $f(\varepsilon, \ell; r_\gamma)$,

$$g(\varepsilon, \ell; r_\gamma) = -h(\varepsilon, \ell; r_\gamma) - A(\varepsilon, \ell) B(\varepsilon, 0) f(\varepsilon, \ell; r_\gamma), \quad (\text{A.25})$$

where

$$B(\varepsilon, \ell) = \frac{1}{2\pi} \psi\left(\frac{i}{\sqrt{\varepsilon}} + \ell + 1\right) + \frac{1}{2\pi} \psi\left(\frac{i}{\sqrt{\varepsilon}} - \ell\right) - \frac{1}{\pi} \log\left(\frac{i}{\sqrt{\varepsilon}}\right) - \frac{i}{\exp\left(\frac{2\pi}{\sqrt{\varepsilon}}\right) - 1} \quad (\text{A.26})$$

$$= \frac{\varepsilon}{\pi} \left\{ \sum_{p=0}^{\ell} \frac{p}{1 + p^2 \varepsilon} + \frac{1}{12} \left(1 + \frac{\varepsilon}{10} + \frac{\varepsilon^2}{21} + \frac{\varepsilon^3}{20} + \mathcal{O}(\varepsilon^4) \right) \right\}. \quad (\text{A.27})$$

In Eq. (A.25) $B(\varepsilon, \ell = 0)$ is set according to the normalization which gives $\tilde{g}_\ell(p, r) = g(\varepsilon, \ell; r_\gamma)$.

Let us define

$$A(\varepsilon, \ell)B(\varepsilon, 0) = \sum_{n=1}^N \varepsilon^n \omega_{n,\ell} + \mathcal{O}(\varepsilon^{N+1}), \quad (\text{A.28})$$

then the convergent expression is written as

$$g(\varepsilon, \ell; r_\gamma) = \sum_{q=0}^{\infty} \varepsilon^q \left[\sum_{p=0}^q \beta_{q-p} \chi_p^{(g)}(\ell, r_\gamma) \right], \quad (\text{A.29})$$

where

$$\chi_p^{(g)}(\ell, r_\gamma) = \begin{cases} \sigma_{0,\ell} \chi_q^{(h)}(\ell, r_\gamma) & \text{for } q = 0, \\ \sum_{m=0}^{\min(q,\ell)} \sigma_{m,\ell} \chi_{q-m}^{(h)}(\ell, r_\gamma) - \sum_{m=1}^q \omega_{m,\ell} \chi_{q-m}^{(f)}(\ell, r_\gamma) & \text{for } q > 0, \end{cases} \quad (\text{A.30})$$

and

$$\beta_i = \begin{cases} -\pi \frac{(-\gamma)^\ell}{(2\ell+1)!} & \text{for } i = 0 \text{ and } r_\gamma > 0, \\ -\pi \frac{(-\gamma)^\ell}{(2\ell+1)!} & \text{for } i = 0 \text{ and } r_\gamma < 0, R = -r_\gamma, \\ 0 & \text{for } i \geq 1. \end{cases} \quad (\text{A.31})$$

In the following we give the first few functions of the expansion of $\tilde{g}_\ell(p, r)$ in power of p^2 that we use in Eq. (2.59)–(2.62),

$$g_{0,\ell}^{(\pm)}(r) = \pm \frac{2(\pm\gamma)^{\ell+1/2}}{(2\ell+1)!} \sqrt{r} \mathcal{N}_{2\ell+1}^{(\pm)}(2\sqrt{\pm r\gamma}), \quad (\text{A.32})$$

$$g_{2,0}^{(\pm)}(r) = \frac{2r^2}{3} \mathcal{N}_2^{(\pm)}(2\sqrt{\pm r\gamma}) \mp \frac{\sqrt{r}}{3(\pm\gamma)^{3/2}} \mathcal{J}_1^{(\pm)}(2\sqrt{\pm r\gamma}), \quad (\text{A.33})$$

$$g_{2,1}^{(\pm)}(r) = \frac{r}{18} \left[\pm 2(r\gamma - 4) \mathcal{N}_4^{(\pm)}(2\sqrt{\pm r\gamma}) \mp \frac{2(r\gamma - 12) \mathcal{N}_3^{(\pm)}(2\sqrt{\pm r\gamma})}{\sqrt{\pm r\gamma}} \mp \frac{\mathcal{J}_3^{(\pm)}(2\sqrt{\pm r\gamma})}{\sqrt{\pm r\gamma}} \right], \quad (\text{A.34})$$

$$g_{2,2}^{(\pm)}(r\gamma) = \frac{\sqrt{\pm r\gamma}}{360} \left[\pm 2\sqrt{\pm r\gamma}(\gamma r - 12) \mathcal{N}_6^{(\pm)}(2\sqrt{\pm r\gamma}) \mp 4(\gamma r - 30) \mathcal{N}_5^{(\pm)}(2\sqrt{\pm r\gamma}) \mp \mathcal{J}_5^{(\pm)}(2\sqrt{\pm r\gamma}) \right], \quad (\text{A.35})$$

$$g_{4,0}^{(\pm)}(r) = \frac{1}{45\gamma^4} \left\{ \mp 18(-\gamma r)^3 \mathcal{N}_6^{(\pm)}(2\sqrt{\pm r\gamma}) \pm 5(\gamma r + 18)(\pm\gamma r)^{5/2} \mathcal{N}_5^{(\pm)}(2\sqrt{\pm r\gamma}) \pm 5\gamma^2 r^2 \mathcal{J}_2^{(\pm)}(2\sqrt{\pm r\gamma}) \mp 6\sqrt{\pm\gamma r} \mathcal{J}_1^{(\pm)}(2\sqrt{\pm r\gamma}) \right\}, \quad (\text{A.36})$$

$$g_{4,1}^{(\pm)}(r) = \frac{r^{3/2}}{270(\pm\gamma)^{3/2}} \left\{ \frac{(5\gamma^2 r^2 - 264) \mathcal{J}_6^{(\pm)}(2\sqrt{\pm r\gamma})}{(\pm\gamma r)^{3/2}} \pm \frac{6(\gamma r(5\gamma r - 11) - 220) \mathcal{J}_5^{(\pm)}(2\sqrt{\pm r\gamma})}{(\gamma r)^2} \pm [\gamma r(5\gamma r + 4) - 720] \mathcal{N}_5^{(\pm)}(2\sqrt{\pm r\gamma}) \mp 8\sqrt{\pm\gamma r}(\gamma r - 18) \mathcal{N}_6^{(\pm)}(2\sqrt{\pm r\gamma}) \right\}, \quad (\text{A.37})$$

$$\begin{aligned}
g_{4,2}^{(\pm)}(r) = \frac{r^2}{5400(\pm\gamma r)^{3/2}} \left\{ \pm 2(5\gamma r - 153) \mathcal{J}_5^{(\pm)}(2\sqrt{\pm r\gamma}) \right. \\
\pm \sqrt{\pm\gamma r} 12(\gamma r(\gamma r + 8) - 96) \mathbf{K}_6(2\sqrt{r\gamma}) \\
+ \sqrt{\pm\gamma r} 5(\gamma r - 12) \mathcal{J}_6^{(\pm)}(2\sqrt{\pm r\gamma}) \\
\left. \pm (5\gamma^3 r^3 - 108\gamma^2 r^2 - 192\gamma r + 5760) \mathcal{N}_5^{(\pm)}(2\sqrt{\pm r\gamma}) \right\}, \quad (\text{A.38})
\end{aligned}$$

$$\begin{aligned}
g_{6,0}^{(\pm)}(r_\gamma) = \frac{r}{5670\gamma^5} \left\{ 10(\pm\gamma r)^3(7\gamma r + 162) \mathcal{N}_8^{(\pm)}(2\sqrt{r\gamma}) \right. \\
- 756(\gamma r + 15)(\pm\gamma r)^{5/2} \mathcal{N}_7^{(\pm)}(2\sqrt{\pm r\gamma}) \\
- \left(105\gamma^6 r^6 + 8946\gamma^5 r^5 + 75600\gamma^4 r^4 - 119520\gamma^3 r^3 \right. \\
\left. - 462240\gamma^2 r^2 + 2592000\gamma r + 7257600 \right) \frac{\mathcal{J}_7^{(\pm)}(2\sqrt{r\gamma})}{(\pm\gamma r)^{7/2}} \\
- \left(1008\gamma^5 r^5 + 11088\gamma^4 r^4 - 15120\gamma^3 r^3 \right. \\
\left. - 73440\gamma^2 r^2 + 345600\gamma r + 1036800 \right) \frac{\mathcal{J}_8^{(\pm)}(2\sqrt{\pm r\gamma})}{\gamma^3 r^3} \left. \right\}, \quad (\text{A.39})
\end{aligned}$$

$$\begin{aligned}
g_{6,1}^{(\pm)}(r\gamma) = \frac{r^2}{34020\gamma^3} & \left\{ -\frac{3749760}{(\pm\gamma r)^{7/2}} \mathcal{J}_7^{(\pm)}(2\sqrt{\pm r\gamma}) \right. \\
& + 4\sqrt{\pm\gamma r}[\gamma r(621 - 154\gamma r) + 34020] \mathcal{N}_7^{(\pm)}(2\sqrt{r\gamma}) \\
& \pm 2\gamma r[\gamma r(35\gamma r + 54) - 9720] \mathcal{N}_8^{(\pm)}(2\sqrt{\pm r\gamma}) \\
& - \left(798\gamma^5 r^5 - 2772\gamma^4 r^4 - 99792\gamma^3 r^3 \right. \\
& \quad \left. + 44640\gamma^2 r^2 + 535680\gamma r \right) \frac{\mathcal{J}_8^{(\pm)}(2\sqrt{\pm r\gamma})}{(\gamma r)^4} \\
& - (105\gamma^4 r^4 + 5670\gamma^3 r^3 - 36036\gamma^2 r^2 \\
& \quad \left. - 694080\gamma r + 401760) \frac{\mathcal{J}_7^{(\pm)}(2\sqrt{\pm r\gamma})}{(\pm\gamma r)^{5/2}} \right\}, \tag{A.40}
\end{aligned}$$

$$\begin{aligned}
g_{6,2}^{(\pm)}(r\gamma) = \frac{r}{680400\gamma^3} & \left\{ -54(7\gamma^3 r^3 - 294\gamma^2 r^2 + 15280) \frac{\mathcal{J}_8^{(\pm)}(2\sqrt{\pm r\gamma})}{\gamma r} \right. \\
& - 3 \left(35\gamma^4 r^4 + 126\gamma^3 r^3 - 38556\gamma^2 r^2 \right. \\
& \quad \left. + 45840\gamma r + 1925280 \right) \frac{\mathcal{J}_7^{(\pm)}(2\sqrt{\pm r\gamma})}{(\pm\gamma r)^{3/2}} \\
& + 12\sqrt{\pm\gamma r} \left(-28\gamma^3 r^3 + 1475\gamma^2 r^2 \right. \\
& \quad \left. + 720\gamma r - 181440 \right) \mathcal{N}_7^{(\pm)}(2\sqrt{\pm r\gamma}) \\
& \pm \gamma r \left(70\gamma^3 r^3 - 2076\gamma^2 r^2 - 8640\gamma r \right. \\
& \quad \left. + 311040 \right) \mathcal{N}_8^{(\pm)}(2\sqrt{\pm r\gamma}) \Big\}, \tag{A.41}
\end{aligned}$$

where $\mathcal{N}_n^{(-)}(x)$ stands for $\pi/2$ times the Bessel function of the second kind $N_n(x)$ and $\mathcal{N}_n^{(+)}(x)$ is the modified Bessel function of the second kind $K_n(x)$.

A.3 van der Waals wave functions

In this section we derive the van der Waals wave functions F_ℓ and G_ℓ , following the steps in Ref. [76]. We first redefine the radial function as $U_\ell(r) = \sqrt{r_s}Z(\rho_s)$. This rearrangement puts Eq. (5.5) into the form of an inhomogeneous Bessel equation,

$$\mathcal{L}_{v_0}Z(\rho_s) = \left[\rho_s^2 \frac{d^2}{d\rho_s^2} + \rho_s \frac{d}{d\rho_s} - v_0^2 + \rho_s^2 \right] Z(\rho_s) = -\frac{p_s^2}{8} \frac{Z(\rho_s)}{\rho_s}, \quad (\text{A.42})$$

with

$$v_0 = \frac{1}{4}(2\ell + 1).$$

The idea, introduced in Ref. [37], is now to consider $Z_v(\rho_s)$ as a series expansion of solutions,

$$Z(\rho_s) = \sum_{n=0}^{\infty} p_s^{2n} \varphi^{(n)}(\rho_s), \quad (\text{A.43})$$

and to use perturbation theory to obtain a solution for $Z_v(\rho_s)$. Substituting Eq. (A.43) into Eq. (A.42) leads to an infinite number of differential equations,

$$\begin{aligned} \mathcal{L}_{v_0} \varphi^{(0)}(\rho_s) + p_s^2 \left[\mathcal{L}_{v_0} \varphi^{(1)}(\rho_s) + \frac{1}{8\rho_s} \varphi^{(0)}(\rho_s) \right] \\ + p_s^4 \left[\mathcal{L}_{v_0} \varphi^{(2)}(\rho_s) + \frac{1}{8\rho_s} \varphi^{(1)}(\rho_s) \right] + \dots = 0. \end{aligned} \quad (\text{A.44})$$

The zeroth-order differential equation is homogenous, while all other orders are inhomogeneous. This procedure generates a secular perturbation in all inhomogeneous differential equations as well as driving terms. The secular terms here refer to the solutions of the zeroth-order differential equation, which are Bessel functions.

Following Ref. [76], we introduce a function $Z_v(\rho_s)$ which has an expansion in terms of

Bessel functions with momentum-dependent coefficients,

$$Z_{\mathbf{v}}(\rho_s) = \sum_{m=-\infty}^{\infty} b_m(p_s) \mathcal{J}_{\mathbf{v}+m}(\rho_s). \quad (\text{A.45})$$

We insert this as an ansatz into Eq. (A.42) with \mathbf{v} yet to be determined. Here \mathcal{J}_n denotes collectively the Bessel and Neumann functions, J_n and N_n . Substitution of Eq. (A.45) into Eq. (A.42) yields a three-term recurrence relation for the b_m functions with $-\infty < m < \infty$,

$$[(\mathbf{v} + m)^2 - \mathbf{v}_0^2]b_m(p_s) + \frac{p_s^2}{16(m + \mathbf{v} - 1)}b_{m-1}(p_s) + \frac{p_s^2}{16(m + \mathbf{v} + 1)}b_{m+1}(p_s) = 0. \quad (\text{A.46})$$

Solving these equations for $b_m(p_s)$ yields

$$b_m(p_s) = (-1)^m \left(\frac{p_s}{4}\right)^{2m} \frac{\Gamma(\mathbf{v})\Gamma(\mathbf{v} - \mathbf{v}_0 + 1)\Gamma(\mathbf{v} + \mathbf{v}_0 + 1)}{\Gamma(\mathbf{v} + m)\Gamma(\mathbf{v} - \mathbf{v}_0 + m + 1)\Gamma(\mathbf{v} + \mathbf{v}_0 + m + 1)} c_m(\mathbf{v}) \quad (\text{A.47})$$

and

$$b_{-m}(p_s) = (-1)^m \left(\frac{p_s}{4}\right)^{2m} \frac{\Gamma(\mathbf{v} - m + 1)\Gamma(\mathbf{v} - \mathbf{v}_0 - m)\Gamma(\mathbf{v} + \mathbf{v}_0 - m)}{\Gamma(\mathbf{v} + 1)\Gamma(\mathbf{v} - \mathbf{v}_0)\Gamma(\mathbf{v} + \mathbf{v}_0)} c_m(-\mathbf{v}) \quad (\text{A.48})$$

for $m \geq 0$. The functions $c_m(\pm\mathbf{v})$ are defined as

$$c_m(\pm\mathbf{v}) = \prod_{s=0}^{m-1} Q(\pm\mathbf{v} + s) b_0(p_s), \quad (\text{A.49})$$

where $Q(\mathbf{v})$ is given by

$$Q(\mathbf{v}) = \frac{1}{1 - \frac{p_s^2}{16(\mathbf{v} + 1)[(\mathbf{v} + 1)^2 - \mathbf{v}_0^2](\mathbf{v} + 2)[(\mathbf{v} + 2)^2 - \mathbf{v}_0^2]} Q(\mathbf{v} + 1)}. \quad (\text{A.50})$$

The coefficient $b_0(p_s)$ only determines the overall normalization and is simply set to one in the following. Eq. (A.46) for $m = 0$ determines the shift ν in the order of the Bessel functions. We determine ν using the constraint

$$(\nu^2 - \nu_0^2) - \frac{Q(-\nu)}{16^2 \nu (\nu - 1) [(\nu - 1)^2 - \nu_0^2]} p_s^4 - \frac{Q(\nu)}{16^2 \nu (\nu + 1) [(\nu + 1)^2 - \nu_0^2]} p_s^4 = 0. \quad (\text{A.51})$$

In general there are several roots which become complex beyond a critical scaled momentum p_s , and one must be careful to choose the physical solution. For a detailed discussion of this point, see Refs. [76, 79].

Choosing either $\mathcal{I}_n = J_n$ or $\mathcal{I}_n = N_n$ already yields a pair of linearly independent solutions. However, in order to get a pair with energy-independent normalization as $r_s \rightarrow 0$ (which ensures analyticity in the energy), we furthermore define

$$x_\ell(p_s) = \cos \eta_\ell \sum_{m=-\infty}^{\infty} (-1)^m b_{2m}(p_s) - \sin \eta_\ell \sum_{m=-\infty}^{\infty} (-1)^m b_{2m+1}(p_s) \quad (\text{A.52})$$

and

$$y_\ell(p_s) = \sin \eta_\ell \sum_{m=-\infty}^{\infty} (-1)^m b_{2m}(p_s) + \cos \eta_\ell \sum_{m=-\infty}^{\infty} (-1)^m b_{2m+1}(p_s), \quad (\text{A.53})$$

with

$$\eta_\ell = \frac{\pi}{2}(\nu - \nu_0).$$

Combining everything, we arrive at the van der Waals wave functions,

$$F_\ell(p, r) = \frac{r_s^{1/2}}{x_\ell^2(p_s) + y_\ell^2(p_s)} \left[x_\ell(p_s) \sum_{m=-\infty}^{\infty} b_m(p_s) J_{\nu+m}(\rho_s) - y_\ell(p_s) \sum_{m=-\infty}^{\infty} b_m(p_s) N_{\nu+m}(\rho_s) \right], \quad (\text{A.54})$$

$$G_\ell(p, r) = \frac{r_s^{1/2}}{x_\ell^2(p_s) + y_\ell^2(p_s)} \left[x_\ell(p_s) \sum_{m=-\infty}^{\infty} b_m(p_s) N_{\nu+m}(\rho_s) + y_\ell(p) \sum_{m=-\infty}^{\infty} b_m(p_s) J_{\nu+m}(\rho_s) \right]. \quad (\text{A.55})$$

A.4 Low-energy expansions of the function terms in van der Waals wave functions

In this appendix we expand all functions relating to the van der Waals wave functions in powers of momentum. We first consider ν , the shift in the order of the Bessel functions in Eq. (5.6) and Eq. (5.7). Using Eq. (A.51) in Appendix A.3, we find

$$\nu = \nu_0 - \frac{3}{2^8 \nu_0 (4\nu_0^2 - 1)(\nu_0^2 - 1)} p_s^4 + O(p_s^8), \quad (\text{A.56})$$

where $\nu_0 = (2\ell + 1)/4$. Using the expansion in Eq. (A.47), Eq. (A.48), and Eq. (A.50), we get

$$b_m(p_s) = (-1)^m \frac{\Gamma(\nu_0)\Gamma(2\nu_0 + 1)}{m!\Gamma(\nu_0 + m)\Gamma(2\nu_0 + m + 1)} \left(\frac{p_s}{4}\right)^{2m} + O(p_s^{2m+2}) \quad (\text{A.57})$$

and

$$b_{-m}(p_s) = \frac{\Gamma(\nu_0 - m + 1)\Gamma(2\nu_0 - m)}{m!\Gamma(\nu_0 + 1)\Gamma(2\nu_0)} \left(\frac{p_s}{4}\right)^{2m} + O(p_s^{2m+2}) \quad (\text{A.58})$$

for $m \geq 0$. Substituting these expressions into Eq. (A.52) and Eq. (A.53) we obtain

$$x_\ell(p_s) = 1 + O(p_s^4), \quad (\text{A.59})$$

$$y_\ell(p_s) = - \left[\frac{\Gamma(\nu_0)\Gamma(2\nu_0 - 1)}{\Gamma(\nu_0 + 1)\Gamma(2\nu_0)} + \frac{\Gamma(\nu_0)\Gamma(2\nu_0 + 1)}{\Gamma(\nu_0 + 1)\Gamma(2\nu_0 + 2)} \right] \left(\frac{p_s}{4}\right)^2 + O(p_s^4). \quad (\text{A.60})$$

B.1 Wronskians of the wave functions

B.1.1 Single channel

Here we calculate Wronskians of the wave function, $U_\ell^{(p)}(r)$, and Wronskians of combinations of the $s_{n,\ell}(r)$ and $c_{n,\ell}(r)$ functions. The Wronskian of $U_\ell^{(p)}(r)$ for the non-interacting region $r > R$ is

$$\begin{aligned}
 W[U_\ell^{(p_a)}(r), U_\ell^{(p_b)}(r)] &= (p_a^2 - p_b^2)W[u_{2,\ell}, u_{0,\ell}](r) \\
 &\quad + (p_a^4 - p_b^4)W[u_{4,\ell}, u_{0,\ell}](r) \\
 &\quad + (p_a^4 p_b^2 - p_b^4 p_a^2)W[u_{4,\ell}, u_{2,\ell}](r) \\
 &\quad + (p_a^6 - p_b^6)W[u_{6,\ell}, u_{0,\ell}](r) + \mathcal{O}(p_a^8 + p_b^8), \tag{B.1}
 \end{aligned}$$

where

$$W[u_{2,\ell}, u_{0,\ell}](r) = \frac{1}{2}r\ell W[s_{0,\ell}, c_{0,\ell}](r) + \frac{1}{2}b_{1,\ell}(r), \tag{B.2}$$

$$W[u_{4,\ell}, u_{0,\ell}](r) = P_\ell W[s_{0,\ell}, c_{0,\ell}](r) + b_{2,\ell}(r), \quad (\text{B.3})$$

$$W[u_{6,\ell}, u_{0,\ell}](r) = Q_\ell W[s_{0,\ell}, c_{0,\ell}](r) + b_{3,\ell}(r), \quad (\text{B.4})$$

$$W[u_{4,\ell}, u_{2,\ell}](r) = b_{4,\ell}(r). \quad (\text{B.5})$$

It should be noted that $W[f, g] = -W[g, f]$. The functions $b_{n,\ell}(r)$ are defined in terms of Wronskians of combinations of the $s_{n,\ell}(r)$ and $c_{n,\ell}(r)$ functions by

$$\begin{aligned} b_{1,\ell}(r) = & \frac{2}{a_\ell^2} W[s_{2,\ell}, s_{0,\ell}](r) - \frac{2}{a_\ell} W[s_{2,\ell}, c_{0,\ell}](r) \\ & - \frac{2}{a_\ell} W[c_{2,\ell}, s_{0,\ell}](r) + 2W[c_{2,\ell}, c_{0,\ell}](r), \end{aligned} \quad (\text{B.6})$$

$$\begin{aligned} b_{2,\ell}(r) = & -\frac{r_\ell}{2a_\ell} W[s_{2,\ell}, s_{0,\ell}](r) + \frac{1}{2} r_\ell W[s_{2,\ell}, c_{0,\ell}](r) \\ & + \frac{1}{a_\ell^2} W[s_{4,\ell}, s_{0,\ell}](r) - \frac{1}{a_\ell} W[s_{4,\ell}, c_{0,\ell}](r) \\ & - \frac{1}{a_\ell} W[c_{4,\ell}, s_{0,\ell}](r) + W[c_{4,\ell}, c_{0,\ell}](r), \end{aligned} \quad (\text{B.7})$$

$$\begin{aligned} b_{3,\ell}(r) = & W[c_{6,\ell}, c_{0,\ell}](r) + P_\ell W[s_{2,\ell}, c_{0,\ell}](r) + \frac{1}{a_\ell^2} W[s_{6,\ell}, s_{0,\ell}](r) \\ & - \frac{1}{a_\ell} W[c_{6,\ell}, s_{0,\ell}](r) - \frac{1}{a_\ell} W[s_{6,\ell}, c_{0,\ell}](r) + \frac{r_\ell}{2} W[s_{4,\ell}, c_{0,\ell}](r) \\ & - \frac{P_\ell}{a_\ell} W[s_{2,\ell}, s_{0,\ell}](r) - \frac{r_\ell}{2a_\ell} W[s_{4,\ell}, s_{0,\ell}](r), \end{aligned} \quad (\text{B.8})$$

$$\begin{aligned}
b_{4,\ell}(r) = & W[c_{4,\ell}, c_{2,\ell}](r) + \left(\frac{r_\ell^2}{4} + \frac{P_\ell}{a_\ell} \right) W[s_{2,\ell}, s_{0,\ell}](r) - \frac{r_\ell}{2a_\ell} W[s_{4,\ell}, s_{0,\ell}](r) \\
& + \frac{r_\ell}{2} W[c_{4,\ell}, s_{0,\ell}](r) + \frac{r_\ell}{2} W[s_{2,\ell}, c_{2,\ell}](r) + \frac{1}{a_\ell^2} W[s_{4,\ell}, s_{2,\ell}](r) \\
& + P_\ell W[s_{0,\ell}, c_{2,\ell}](r) - \frac{1}{a_\ell} W[c_{4,\ell}, s_{2,\ell}](r) - \frac{1}{a_\ell} W[s_{4,\ell}, c_{2,\ell}](r). \tag{B.9}
\end{aligned}$$

We now calculate Wronskians of all possible combinations of $s_0(r)$, $s_2(r)$, $c_0(r)$ and $c_2(r)$ functions. We find

$$W[s_{0,\ell}, c_{0,\ell}] = -1, \tag{B.10}$$

$$W[s_{0,\ell}, c_{2,\ell}](r) = -\frac{r^2}{2+4\ell}, \tag{B.11}$$

$$W[s_{2,\ell}, c_{0,\ell}](r) = \frac{r^2}{2+4\ell}, \tag{B.12}$$

$$W[s_{2,\ell}, c_{2,\ell}](r) = \frac{r^4}{16\ell(\ell+1)-12}, \tag{B.13}$$

$$W[s_{0,\ell}, s_{2,\ell}](r) = \frac{\pi}{\Gamma(\frac{3}{2}+\ell)\Gamma(\frac{5}{2}+\ell)} \left(\frac{r}{2}\right)^{3+2\ell}, \tag{B.14}$$

$$W[c_{0,\ell}, c_{2,\ell}](r) = -\frac{\Gamma(-\frac{1}{2}+\ell)\Gamma(\frac{1}{2}+\ell)}{\pi} \left(\frac{r}{2}\right)^{1-2\ell}. \tag{B.15}$$

B.1.2 Coupled channels

Here we calculate Wronskians of the $U(r)$ and $V(r)$ wave functions. Wronskians of $U_\alpha(r)$ and $V_\alpha(r)$ for the non-interacting region $r \geq R$ are

$$\begin{aligned}
W[U_{a\alpha}(r), U_{b\alpha}(r)] &= (p_a^2 - p_b^2) \left\{ \frac{1}{2} r_{j-1} W[s_0(r), c_0(r)]_{j-1} \right. \\
&\quad + \frac{1}{a_{j-1}^2} W[s_2(r), s_0(r)]_{j-1} + \frac{1}{a_{j-1}} W[c_0(r), s_2(r)]_{j-1} \\
&\quad + \frac{1}{a_{j-1}} W[s_0(r), c_2(r)]_{j-1} + W[c_2(r), c_0(r)]_{j-1} \left. \right\} \\
&\quad + \mathcal{O}(p_a^4) + \mathcal{O}(p_b^4), \tag{B.16}
\end{aligned}$$

$$W[V_{a\alpha}(r), V_{b\alpha}(r)] = (p_a^2 - p_b^2) q_0^2 W[c_2(r), c_0(r)]_{j+1} + \mathcal{O}(p_a^4) + \mathcal{O}(p_b^4). \tag{B.17}$$

Wronskians of the β -state wave functions are

$$W[U_{a\beta}(r), U_{b\beta}(r)] = (p_a^2 - p_b^2) q_0^2 \frac{1}{a_{j+1}^2} W[s_2(r), s_0(r)]_{j-1} + \mathcal{O}(p_a^4) + \mathcal{O}(p_b^4), \tag{B.18}$$

$$\begin{aligned}
W[V_{a\beta}(r), V_{b\beta}(r)] &= (p_a^2 - p_b^2) \left\{ \frac{1}{2} r_{j+1} W[s_0(r), c_0(r)]_{j+1} \right. \\
&\quad + \frac{1}{a_{j+1}^2} W[s_2(r), s_0(r)]_{j+1} + \frac{1}{a_{j+1}} W[c_0(r), s_2(r)]_{j+1} \\
&\quad + \frac{1}{a_{j+1}} W[s_0(r), c_2(r)]_{j+1} + W[c_2(r), c_0(r)]_{j+1} \left. \right\} \\
&\quad + \mathcal{O}(p_a^4) + \mathcal{O}(p_b^4). \tag{B.19}
\end{aligned}$$

Wronskian of the combinations of the α and β -states are

$$\begin{aligned}
W[U_{a\alpha}(r), U_{b\beta}(r)] &= q_0 \frac{1}{a_{j+1}} W[c_0(r), s_0(r)]_{j-1} - p_a^2 \left\{ q_0 \frac{1}{a_{j-1}a_{j+1}} W[s_2(r), s_0(r)]_{j-1} \right. \\
&\quad \left. - q_0 \frac{1}{a_{j+1}} W[c_2(r), s_0(r)]_{j-1} \right\} + p_b^2 \left\{ q_0 \frac{1}{a_{j-1}a_{j+1}} W[s_2(r), s_0(r)]_{j-1} \right. \\
&\quad \left. - q_0 \frac{1}{a_{j+1}} W[s_2(r), c_0(r)]_{j-1} + q_0 \frac{r_{j+1}}{2} W[s_0(r), c_0(r)]_{j-1} \right. \\
&\quad \left. - q_1 \frac{1}{a_{j+1}} W[s_0(r), c_0(r)]_{j-1} \right\} + \mathcal{O}(p^4), \tag{B.20}
\end{aligned}$$

$$\begin{aligned}
W[U_{a\beta}(r), U_{b\alpha}(r)] &= -q_0 \frac{1}{a_{j+1}} W[c_0(r), s_0(r)]_{j-1} + p_b^2 \left\{ q_0 \frac{1}{a_{j-1}a_{j+1}} W[s_2(r), s_0(r)]_{j-1} \right. \\
&\quad \left. - q_0 \frac{1}{a_{j+1}} W[c_2(r), s_0(r)]_{j-1} \right\} - p_a^2 \left\{ q_0 \frac{1}{a_{j-1}a_{j+1}} W[s_2(r), s_0(r)]_{j-1} \right. \\
&\quad \left. - q_0 \frac{1}{a_{j+1}} W[s_2(r), c_0(r)]_{j-1} + q_0 \frac{r_{j+1}}{2} W[s_0(r), c_0(r)]_{j-1} \right. \\
&\quad \left. - q_1 \frac{1}{a_{j+1}} W[s_0(r), c_0(r)]_{j-1} \right\} + \mathcal{O}(p^4), \tag{B.21}
\end{aligned}$$

$$\begin{aligned}
W[V_{a\alpha}(r), V_{b\beta}(r)] &= -q_0 \frac{1}{a_{j+1}} W[c_0(r), s_0(r)]_{j+1} - p_a^2 \left\{ q_1 \frac{1}{a_{j+1}} W[c_0(r), s_0(r)]_{j+1} \right. \\
&\quad \left. + q_0 \frac{1}{a_{j+1}} W[c_2(r), s_0(r)]_{j+1} - q_0 W[c_2(r), c_0(r)]_{j+1} \right\} \\
&\quad + p_b^2 \left\{ q_0 \frac{r_{j+1}}{2} W[c_0(r), s_0(r)]_{j+1} - q_0 \frac{1}{a_{j+1}} W[c_0(r), s_2(r)]_{j+1} \right. \\
&\quad \left. + q_0 W[c_0(r), c_2(r)]_{j+1} \right\} + \mathcal{O}(p^4), \tag{B.22}
\end{aligned}$$

$$\begin{aligned}
W[V_{a\beta}(r), V_{b\alpha}(r)] &= q_0 \frac{1}{a_{j+1}} W[c_0(r), s_0(r)]_{j+1} + p_b^2 \left\{ q_1 \frac{1}{a_{j+1}} W[c_0(r), s_0(r)]_{j+1} \right. \\
&\quad \left. + q_0 \frac{1}{a_{j+1}} W[c_2(r), s_0(r)]_{j+1} - q_0 W[c_2(r), c_0(r)]_{j+1} \right\} \\
&\quad - p_a^2 \left\{ q_0 \frac{r_{j+1}}{2} W[c_0(r), s_0(r)]_{j+1} - q_0 \frac{1}{a_{j+1}} W[c_0(r), s_2(r)]_{j+1} \right. \\
&\quad \left. + q_0 W[c_0(r), c_2(r)]_{j+1} \right\} + \mathcal{O}(p^4). \tag{B.23}
\end{aligned}$$

C.1 Coupled-channel Parameterizations

The scattering matrix in terms of the eigenphase parameters was given in Eq. (4.21). The scattering matrix in terms of the nuclear bar parameters is

$$S = \begin{pmatrix} e^{2i\bar{\delta}_\alpha} \cos 2\bar{\epsilon} & ie^{i(\bar{\delta}_\alpha + \bar{\delta}_\beta)} \sin 2\bar{\epsilon} \\ ie^{i(\bar{\delta}_\alpha + \bar{\delta}_\beta)} \sin 2\bar{\epsilon} & e^{2i\bar{\delta}_\beta} \cos 2\bar{\epsilon} \end{pmatrix}. \quad (\text{C.1})$$

Here $\bar{\delta}_\alpha$, $\bar{\delta}_\beta$ and $\bar{\epsilon}$ are the nuclear bar phase shifts and mixing angle [160]. The relations between the eigenphase and the nuclear bar parameters are

$$\sin(\delta_\alpha - \delta_\beta) = \frac{\sin 2\bar{\epsilon}}{\sin 2\epsilon}, \quad (\text{C.2})$$

$$\delta_\alpha + \delta_\beta = \bar{\delta}_\alpha + \bar{\delta}_\beta, \quad (\text{C.3})$$

$$\tan 2\epsilon = \frac{\tan 2\bar{\epsilon}}{\sin(\bar{\delta}_\alpha - \bar{\delta}_\beta)}. \quad (\text{C.4})$$

The two-channel effective range expansion is defined slightly differently in the eigenphase

and the nuclear bar parameterizations. In the eigenphase parameterization,

$$\sum_{m'm''n'n'} \mathbf{p}_{mm'} U_{m'm''} [\mathbf{K}^{-1}]_{m''n''} [U^{-1}]_{n''n'} \mathbf{p}_{n'n} = -\frac{1}{a_{mn}} + \frac{1}{2} r_{mn} p^2 + \mathcal{O}(p^4), \quad (\text{C.5})$$

and in the nuclear bar parameterization,

$$\sum_{m'n'} \mathbf{p}_{mm'} [\mathbf{K}^{-1}]_{m''n''} \mathbf{p}_{n'n} = -\frac{1}{\bar{a}_{mn}} + \frac{1}{2} \bar{r}_{mn} p^2 + \mathcal{O}(p^4), \quad (\text{C.6})$$

where \mathbf{p}_{mn} is the diagonal momentum matrix $\text{diag}(p^{j-1/2}, p^{j+3/2})$. Therefore, by straightforward calculations we find the following relations among the threshold scattering parameters,

$$a_\alpha = \bar{a}_\alpha, \quad (\text{C.7})$$

$$r_\alpha = \bar{r}_\alpha + \frac{2\bar{q}_0\bar{q}_1}{\bar{a}_\alpha} + \frac{\bar{q}^2\bar{r}_\beta}{\bar{a}_\alpha^2}, \quad (\text{C.8})$$

$$a_\beta = \bar{a}_\beta - \frac{\bar{q}_0^2}{\bar{a}_\alpha}, \quad (\text{C.9})$$

$$r_\beta = \bar{r}_\beta, \quad (\text{C.10})$$

$$q_0 = \frac{\bar{q}_0}{\bar{a}_\alpha}, \quad (\text{C.11})$$

$$q_1 = \frac{(\bar{a}_\beta\bar{a}_\alpha - \bar{q}_0^2)(\bar{a}_\alpha\bar{q}_1 + \bar{r}_\beta\bar{q}_0)}{2\bar{a}_\alpha^2}. \quad (\text{C.12})$$

For the uncoupled channels q_0 and q_1 are zero, and these relations become $a_\alpha = \bar{a}_\alpha$, $r_\alpha = \bar{r}_\alpha$, $a_\beta = \bar{a}_\beta$, and $r_\beta = \bar{r}_\beta$.

C.2 Numerical Test using Delta-Function Shell Potentials in a coupled-channel system

As an example to test the equalities in Eq. (4.50), Eq. (4.51) and Eq. (4.54), we consider the scattering of two spin- $\frac{1}{2}$ particles with a delta-function shell potential and partial-wave mixing,

$$W(r, R) = \begin{pmatrix} C_{11} & C_{12} \\ C_{12} & C_{22} \end{pmatrix} \delta(r - R). \quad (\text{C.13})$$

The coupled radial Schrödinger equations become

$$-\frac{d^2 U(r)}{dr^2} - k^2 U(r) + 2\mu C_{11} \delta(r - R) U(r) + 2\mu C_{12} \delta(r - R) V(r) = 0, \quad (\text{C.14})$$

$$-\frac{d^2 V(r)}{dr^2} - k^2 V(r) + \frac{6}{r^2} V(r) + 2\mu C_{21} \delta(r - R) U(r) + 2\mu C_{22} \delta(r - R) V(r) = 0. \quad (\text{C.15})$$

The interaction potentials are non-vanishing only at $r = R$, and everywhere else the wave functions of particles are free wave solutions. We split the space in two regions, $r > R$ and $r < R$. Solutions for the region $r > R$ are the same as functions in Eq. (4.29)-(4.32). For $r < R$ these functions must satisfy the boundary conditions at the origin. After normalization, the solutions for the region $r > R$ are

$$U_{\alpha}^{II}(r) = \cos \varepsilon(k) k^{J-1} \left[\cot \delta_{J-1}(k) S_{J-1}(kr) + C_{J-1}(kr) \right], \quad (\text{C.16})$$

$$V_{\alpha}^{II}(r) = \sin \varepsilon(k) k^{J-1} \left[\cot \delta_{J-1}(k) S_{J+1}(kr) + C_{J+1}(kr) \right], \quad (\text{C.17})$$

$$U_{\beta}^{II}(r) = -\sin \varepsilon(k) k^{J+1} \left[\cot \delta_{J+1}(k) S_{J-1}(kr) + C_{J-1}(kr) \right], \quad (\text{C.18})$$

$$V_{\beta}^{II}(r) = \cos \varepsilon(k) k^{J+1} \left[\cot \delta_{J+1}(k) S_{J+1}(kr) + C_{J+1}(kr) \right], \quad (\text{C.19})$$

and for the region $r < R$,

$$U_{\alpha}^I(r) = A(k) \cos \varepsilon(k) k^{J-1} S_{J-1}(kr), \quad (\text{C.20})$$

$$V_{\alpha}^I(r) = B(k) \sin \varepsilon(k) k^{J-1} S_{J+1}(kr), \quad (\text{C.21})$$

$$U_{\beta}^I(r) = -D(k) \sin \varepsilon(k) k^{J+1} S_{J-1}(kr), \quad (\text{C.22})$$

$$V_{\beta}^I(r) = E(k) \cos \varepsilon(k) k^{J+1} S_{J+1}(kr). \quad (\text{C.23})$$

Here $A(k)$, $B(k)$, $D(k)$ and $E(k)$ are amplitudes to be determined by boundary conditions.

At the boundary between two regions we have

$$U^H(R) = U^I(R), \quad (\text{C.24})$$

$$V^H(R) = V^I(R). \quad (\text{C.25})$$

In addition, by integrating Eq. (C.14) and Eq. (C.15) around $r = R$, we have

$$-\left(\frac{dU(r)}{dr}\right)_{R-\eta}^{R+\eta} + 2\mu C_{11}U(R) + 2\mu C_{12}V(R) = 0, \quad (\text{C.26})$$

$$-\left(\frac{dV(r)}{dr}\right)_{R-\eta}^{R+\eta} + 2\mu C_{22}V(R) + 2\mu C_{21}U(R) = 0. \quad (\text{C.27})$$

Taking $\eta \rightarrow 0$, we obtain two more boundary conditions,

$$\lim_{\eta \rightarrow 0} \left(\left. \frac{dU^H(r)}{dr} \right|_{(R+\eta)} - \left. \frac{dU^I(r)}{dr} \right|_{(R-\eta)} \right) = 2\mu C_{11}U(R) + 2\mu C_{12}V(R), \quad (\text{C.28})$$

$$\lim_{\eta \rightarrow 0} \left(\left. \frac{dV^H(r)}{dr} \right|_{(R+\eta)} - \left. \frac{dV^I(r)}{dr} \right|_{(R-\eta)} \right) = 2\mu C_{22}V(R) + 2\mu C_{21}U(R). \quad (\text{C.29})$$

Next we use these four boundary conditions to find phase shifts and mixing parameters as well as all unknown amplitudes. After substituting wave functions in Eq. (C.16)-(C.23) into these

boundary conditions, we get the following equations for the $J - 1$ channel,

$$A(k) = \cot \delta_{J-1}(k) + \frac{C_{J-1}(kR)}{S_{J-1}(kR)}, \quad (\text{C.30})$$

$$B(k) = \cot \delta_{J-1}(k) + \frac{C_{J+1}(kR)}{S_{J+1}(kR)}, \quad (\text{C.31})$$

$$\begin{aligned} & \cot \delta_{J-1}(k) S'_{J-1}(kR) + C'_{J-1}(kR) - A(k) S'_{J-1}(kR) \\ &= 2\mu C_{11} A(k) S_{J-1}(kR) + 2\mu C_{12} \tan \varepsilon(k) B(k) S_{J+1}(kR), \end{aligned} \quad (\text{C.32})$$

$$\begin{aligned} & \tan \varepsilon(k) \left[\cot \delta_{J-1}(k) S'_{J+1}(kR) + C'_{J+1}(kR) - B(k) S'_{J+1}(kR) \right] \\ &= 2\mu C_{22} \tan \varepsilon(k) B(k) S_{J+1}(kR) + 2\mu C_{21} A(k) S_{J-1}(kR), \end{aligned} \quad (\text{C.33})$$

and following equations for the $J + 1$ channel,

$$D(k) = \cot \delta_{J+1}(k) + \frac{C_{J-1}(kR)}{S_{J-1}(kR)}, \quad (\text{C.34})$$

$$E(k) = \cot \delta_{J+1}(k) + \frac{C_{J+1}(kR)}{S_{J+1}(kR)}, \quad (\text{C.35})$$

$$\begin{aligned} & \tan \varepsilon(k) \left[\cot \delta_{J+1}(k) S'_{J-1}(kR) + C'_{J-1}(kR) + D(k) S'_{J-1}(kR) \right] \\ &= 2\mu C_{11} \tan \varepsilon(k) D(k) S_{J-1}(kR) - 2\mu C_{12} E(k) S_{J+1}(kR), \end{aligned} \quad (\text{C.36})$$

$$\begin{aligned} & \cot \delta_{J+1}(k) S'_{J+1}(kR) + C'_{J+1}(kR) - E(k) S'_{J+1}(kR) \\ &= 2\mu C_{22} E(k) S_{J+1}(kR) - 2\mu C_{21} \tan \varepsilon(k) D(k) S_{J-1}(kR). \end{aligned} \quad (\text{C.37})$$

In the following, we present the results from numerical calculations for $j \leq 3$. For numerical solutions we use free parameters μ , C_{11} , C_{12} , C_{22} , R and r to calculate some numerical data for the scattering phase shifts and mixing angle. Then we use some fitting procedure to determine the scattering lengths, effective ranges and mixing parameters. We simply fit the data to Eq. (4.40) and (4.41). It is clear that there is an abundance of free parameters which we can use to determine the scattering parameters. However, we set these free parameters such values that we can obtain very nice fits to the data.

C.2.0.1 Example 1. 3S_1 - 3D_1 Coupling.

Our first example is the 3S_1 - 3D_1 coupled channel corresponding with $j = 1$. We perform numerical calculations using $2\mu C_{11} = -6.4$ MeV, $2\mu C_{12} = -0.28$ MeV, $2\mu C_{22} = -1.4$ MeV and $R = 2.6$ fm. Results are shown in Table C.1 and Table C.2.

Table C.1 Numerical results for scattering length and effective range in two-body interaction by the delta function potentials.

Channel	a_L [fm $^{2L+1}$]	r_L [fm $^{-2L+1}$]
3S_1	2.766	1.804
3D_1	-0.326	-36.876
3P_2	16.108	-1.110
3F_2	-0.039	-287.01
3D_3	8.832	-0.665
3G_3	0.008	-1550.6

For $r = 6.5$ fm and $k = 0.335$ MeV, we obtain

$$b_0(r) - q_0^2 \frac{6}{r^3} - r_0 = 4.577 \text{ fm}, \quad (\text{C.38})$$

Table C.2 Numerical results for the mixing parameters in two-body interaction by the delta function potentials.

Mixing angle	q_0 [fm ²]	q_1 [fm ⁴]
ε_1	0.075	0.068
ε_2	0.060	0.034
ε_3	0.232	0.057

and this agrees with the predicted equivalent expression within numerical precision,

$$2 \int_0^R \left([U_\alpha^I(r')]^2 + [V_\alpha^I(r')]^2 \right) dr' + 2 \int_R^r \left([U_\alpha^{II}(r')]^2 + [V_\alpha^{II}(r')]^2 \right) dr' = 4.575 \text{ fm}. \quad (\text{C.39})$$

We also find

$$b_2(r) + q_0^2 \frac{2r^3}{3a_2^2} - r_2 = 5978.51 \text{ fm}^{-3}, \quad (\text{C.40})$$

agrees with

$$2 \int_0^R \left([U_\beta^I(r')]^2 + [V_\beta^I(r')]^2 \right) dr' + 2 \int_R^r \left([U_\beta^{II}(r')]^2 + [V_\beta^{II}(r')]^2 \right) dr' = 5934.13 \text{ fm}^{-3}. \quad (\text{C.41})$$

C.2.0.2 Example 2. 3P_2 - 3F_2 Coupling.

The second example is the coupled channel 3P_2 - 3F_2 with $J = 2$. We use $2\mu C_{11} = -1.759$ MeV, $2\mu C_{12} = -0.28$ MeV, $2\mu C_{22} = -1.36$ MeV and $R = 2.6$ fm, and the results for a_1 , a_3 , r_3 , q_0 and q_1 shown in Table C.1 and Table C.2. For $r = 8.42$ fm and $k = 0.33$ MeV we get

$$b_1(r) - q_0^2 \frac{90}{r^5} - r_1 = 5.188 \text{ fm}^{-1}, \quad (\text{C.42})$$

which agrees within numerical precision with

$$2 \int_0^R \left([U_\alpha^I(r')]^2 + [V_\alpha^I(r')]^2 \right) dr' + 2 \int_R^r \left([U_\alpha^{II}(r')]^2 + [V_\alpha^{II}(r')]^2 \right) dr' = 5.187 \text{ fm}^{-1}. \quad (\text{C.43})$$

We also find

$$b_3(r) + q_0^2 \frac{2r^5}{45a_3^2} - r_3 = 2.8052 \times 10^6 \text{ fm}^{-5}, \quad (\text{C.44})$$

which agrees with

$$2 \int_0^R \left([U_\beta^I(r')]^2 + [V_\beta^I(r')]^2 \right) dr' + 2 \int_R^r \left([U_\beta^{II}(r')]^2 + [V_\beta^{II}(r')]^2 \right) dr' = 2.8035 \times 10^6 \text{ fm}^{-5}. \quad (\text{C.45})$$

C.2.0.3 Example 3. 3D_3 - 3G_3 Coupling.

The last example is the 3D_3 - 3G_3 coupled channel with $J = 3$. We use $2\mu C_{11} = -2.255$ MeV, $2\mu C_{12} = -0.28$ MeV, $2\mu C_{22} = -3.27$ MeV and $R = 2.6$ fm, and the parameters a_2, a_4, r_2, a_4, q_0 and q_1 are calculated numerically and indicated in Table C.1 and Table C.2. For $r = 9.7$ fm and $k = 0.33$ MeV the results for the 3D_3 channel are

$$b_2(r) - q_0^2 \frac{3150}{r^7} - r_2 = 120.256 \text{ fm}^{-3}, \quad (\text{C.46})$$

which agrees within numerical precision with

$$2 \int_0^R \left([U_\alpha^I(r')]^2 + [V_\alpha^I(r')]^2 \right) dr' + 2 \int_R^r \left([U_\alpha^{II}(r')]^2 + [V_\alpha^{II}(r')]^2 \right) dr' = 120.88 \text{ fm}^{-3}. \quad (\text{C.47})$$

For $r = 2.93$ fm and $k = 1.0$ MeV, the results of the 3G_3 channel are

$$b_4(r) + \frac{q_0^2}{a_4^2} \frac{2r^7}{1575} - r_4 = 2.218 \times 10^8 \text{ fm}^{-7}, \quad (\text{C.48})$$

which agrees with

$$2 \int_0^R \left([U_\beta^I(r')]^2 + [V_\beta^I(r')]^2 \right) dr' + 2 \int_R^r \left([U_\beta^{II}(r')]^2 + [V_\beta^{II}(r')]^2 \right) dr' = 2.214 \times 10^8 \text{ fm}^{-7}. \quad (\text{C.49})$$

D.1 Finite-volume binding energy corrections and topological volume corrections for scattering with arbitrary ℓ

In order to apply Lüscher's finite-volume method with maximal accuracy, we consider also finite-volume corrections to the binding energy of the dimer. The finite-volume correction to two-body s -wave binding energies was derived in Ref. [123] and extended to arbitrary angular momentum in Ref. [106, 109]. There has also been significant work towards understanding three-body binding energy corrections at finite volume [112, 111].

It was noticed in Ref. [28] that the finite-volume corrections to the dimer binding energy is dependent on the motion of the dimer. This fact has been used to cancel out finite-volume corrections to the binding energy [45]. The dimer motion induces phase-twisted boundary conditions on the dimer's relative-coordinate wavefunction. These effects are called topological volume corrections and were found to have an effect on the finite-volume analysis for scattering of the dimer. The study of topological volume corrections were carried out for s -wave scattering in Ref. [28, 26] and further applied in Ref. [148, 143]. In the following we show the extension to general partial wave ℓ .

The general solution of the Helmholtz equation has the form of

$$\Psi_p(\vec{r}) = \sum_{\ell,m} c_{\ell,m}(p) G_{\ell,m}(\vec{r}, p^2). \quad (\text{D.1})$$

The functions $G_{\ell,m}(\vec{r}, p^2)$ form a linearly independent complete basis set and are defined as

$$G_{\ell,m}(\vec{r}, p^2) = \mathcal{Y}_{\ell,m}(\nabla) G(\vec{r}, p^2). \quad (\text{D.2})$$

Here $\mathcal{Y}_{\ell,m}$ are the solid spherical harmonic polynomials and defined in terms of the spherical harmonics as

$$\mathcal{Y}_{\ell}^m(\vec{r}) = r^{\ell} Y_{\ell}^m(\theta, \phi), \quad (\text{D.3})$$

and $G(\vec{r}, p^2)$ is the periodic Green's function solution to the Helmholtz equation for $\ell, m = 0$,

$$G_{0,0}(\vec{r}, p^2) = G(\vec{r}, p^2) = \frac{1}{L^3} \sum_{\vec{k}} \frac{e^{\frac{2i\pi}{L}\vec{k}\cdot\vec{r}}}{\left(\frac{2\pi}{L}\vec{k}\right)^2 - p^2}. \quad (\text{D.4})$$

Using Eq. (B1) of Ref. [124], we have

$$G_{\ell,m}(\vec{r}, p^2) = r^{\ell} Y_{\ell}^m(\theta, \phi) \left(\frac{1}{r} \frac{\partial}{\partial r}\right)^{\ell} G(\vec{r}, p^2). \quad (\text{D.5})$$

Inserting Eq. (D.4) into Eq. (D.5), we write the asymptotic form of the scattering wave function as

$$u_{\ell}(r) = C \sum_{\vec{k}} |\vec{k}|^{\ell} \frac{e^{\frac{2i\pi}{L}\vec{k}\cdot\vec{r}}}{\left(\frac{2\pi}{L}\vec{k}\right)^2 - p^2}, \quad (\text{D.6})$$

where C is the normalization coefficient. The derivation of the topological volume corrections for the s -wave scattering of two composite particles A and B is given in Ref. [28, 26, 148]. Here we focus on the fermion-dimer scattering and derive the topological volume corrections for higher partial waves.

In this analysis we take the continuum limit. We let the total momentum of the fermion plus dimer system to be zero and let p be the magnitude of the relative momentum between the fermion and dimer. Let $E_{d,\vec{0}}(\infty)$ be the dimer energy at infinite volume and m_d be the dimer mass. Then the fermion-dimer energy at infinite volume, $E_{df}(p, \infty)$, is

$$E_{df}(p, \infty) = \frac{p^2}{2m_d} + \frac{p^2}{2m} + E_{d,\vec{0}}(\infty). \quad (\text{D.7})$$

As in previous studies of fermion-dimer scattering on the lattice [28, 26, 148, 143], we calculate the effective dimer mass of the dimer on the lattice by computing the dimer dispersion relation. Now we let $E_{df}(p, L)$ be the finite-volume energy of the fermion-dimer system. Following Ref. [28, 26, 148], we can compute the expectation value

$$E_{df}(p, L) = \frac{\int d^3r u_\ell^*(r) \hat{H} u_\ell(r)}{\int d^3r |u_\ell(r)|^2} = \frac{1}{\mathcal{N}_\ell} \sum_{\vec{k}}^{k_{max}} |\vec{k}|^{2\ell} \frac{\frac{p^2}{2m_d} + E_{d,\vec{k}}(L)}{(\vec{k}^2 - \eta)^2}, \quad (\text{D.8})$$

where $E_{d,\vec{k}}(L)$ is the finite-volume energy of the dimer with momentum \vec{k} , \mathcal{N}_ℓ is defined as

$$\mathcal{N}_\ell = \sum_{\vec{k}}^{k_{max}} |\vec{k}|^{2\ell} (\vec{k}^2 - \eta)^{-2}, \quad (\text{D.9})$$

and $\eta = \left(\frac{Lp}{2\pi}\right)^2$. For $\ell > 0$ the summations are divergent and we must cutoff the short distance behavior at some momentum scale Λ characterizing the range of the fermion-dimer interactions.

The corresponding maximum index value k_{max} scales as $\Lambda L/(2\pi)$.

Let $\Delta E_{d,\vec{0}}(L) = E_{d,\vec{0}}(L) - E_{d,\vec{0}}(\infty)$ be the finite-volume energy shift of the dimer energy in its rest frame, and $\Delta E_{d,\vec{k}}(L) = E_{d,\vec{k}}(\infty) - E_{d,\vec{k}}(L)$ be the finite-volume energy shift of the dimer energy with momentum \vec{k} . One can show that [28],

$$\frac{\Delta E_{d,\vec{k}}(L)}{\Delta E_{d,\vec{0}}(L)} = \frac{1}{3} \sum_{i=1}^3 \cos(2\pi k_i \alpha). \quad (\text{D.10})$$

Using Eq. (D.7), (D.8), and (D.10), we can now write the fermion-dimer energy correction at finite volume as

$$E_{df}(p, L) - E_{df}(p, \infty) = \tau_\ell(\eta) \Delta E_{d,\vec{0}}(L), \quad (\text{D.11})$$

where $\tau_\ell(\eta)$ is the topological factor,

$$\tau_\ell(\eta) = \frac{1}{\mathcal{N}_\ell} \sum_{\vec{k}}^{k_{max}} \frac{|\vec{k}|^{2\ell} \sum_{i=1}^3 \cos(2\pi k_i \alpha)}{3(\vec{k}^2 - \eta)^2}, \quad (\text{D.12})$$

with $\alpha = m/(m + m_d) = 1/3$. Due to the short distance behavior of the momentum mode summations for $\ell > 0$, we find that the topological phase factor $\tau_\ell(\eta)$ is suppressed by the lattice length L ,

$$\tau_{\ell>0}(\eta) = \mathcal{O}(L^{-1}). \quad (\text{D.13})$$

In other words, the topological volume correction for $\ell > 0$ is smaller by a factor of L relative to the $\ell = 0$ correction. In our analysis of fermion-dimer scattering we have therefore included topological volume corrections as written in Eq. (D.12) for $\ell = 0$, but neglected the corrections for $\ell > 0$. We find that this prescription gives good agreement with the continuum infinite-volume

STM results for partial waves $\ell = 0, 1, 2$.